Contrast Enhanced Ultrasound Molecular Imaging of the Inflammatory Response in Myocarditis

Inauguraldissertation

zur

Erlangung der Würde eines Doktors der Philosophie

vorgelegt der

Philosophisch-Naturwissenschaftlichen Fakultät

der Universität Basel

von

David Steinl

aus Deutschland

Basel, 2019

Genehmigt von der Philosophisch-Naturwissenschaftlichen Fakultät

auf Antrag von

Prof. Dr. Jörg. Huwyler

Prof. Dr. Beat A. Kaufmann

Prof. Dr. Christoph. Handschin

Basel, den 19. September 2017

Dekan Prof. Dr. Martin Spiess

Contents

1 Contrast Enhanced Ultrasound

1.1 Introduction to ultrasound

Observation on bats led the Italian priest Spallanzani to the idea of animal echolocation based on inaudible sound. In the late 19th century, experiments with Galton's whistle on animals led to refinements of the understanding of sound waves that are just beyond the human perception but are audible for smaller mammals. Audible mechanical waves, or "acoustic" waves that humans can sense, have a frequency between 20 Hz - 20 kHz. Sound waves with a lower frequency than 20 Hz are termed infra sound while waves with higher frequency than 20 kHz are termed ultrasound. Regardless of their frequency, they propagate by longitudinal motion via compression and rarefaction of matter.

Today, ultrasound is routinely applied worldwide in various imaging protocols, material assessment and other industrial applications or even in the consumer sector as home therapy devices or for cleaning purposes.
Anecdotal, the development of ultrasound for various applications is based on two events unfolding around the turn of the 19th century.

The first was the experimental demonstration of the piezoelectric effect in 1880 by the two Curie brothers Jacques and Pierre, which constitutes the core principle of the generation and detection of ultrasound.

The second was the tragic disaster of the RMS Titanic in 1912, which fueled public - and most importantly military - interests to detect non-visible and submerged obstacles, ranging from icebergs and riffs to hostile submarines. Great efforts and the incorporation of various technological advances led to the development of sound-based echolocation and echography.

Piezoelectricity describes a process where applied mechanical force on a crystal lattice causes change in the local polarization density which subsequently results in the generation of a differential electric charge (see figure 1.1). This effect is called the direct piezoelectric effect and the generated electric charge is proportional to the degree of deformation exercised on the material, which can be for example quartz, barium titanate or lead zirconate. The crystals' thickness determines the resonance frequency, where output would be maximal.

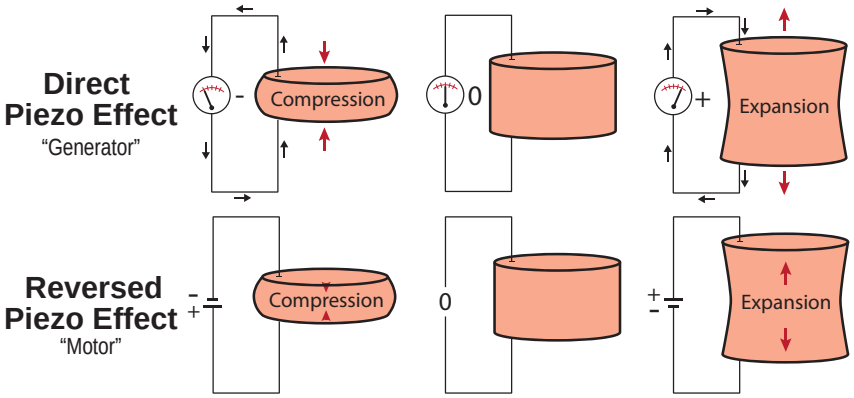

Figure 1.1: Schematics of the direct and reversed piezo-effect. A current forces the crystal material to change shape and thus converts electric into mechanical energy. Applied stress on the resting crystal transforms mechanical into electric energy that can be used to detect the returning ultrasound waves.

But most importantly, this effect can be reversed. In the reversed piezoelectric effect, an applied voltage forces the crystal to expand or shrink and acts as a "motor". This principle is exploited for the formation of ultrasound waves by applying an alternating current.

The single-phase current is inverted at a distinct frequency to force the crystal material into a stable oscillatory deformation that results in the generation of a pressure wave, which propagates through the tissue via compression and rarefaction as a longitudinal wave. The piezoelectric crystals in the transducer are only briefly forced to actively generate ultrasound waves and will return to a passive state to detect back scattered waves ("echoes") and the established voltages caused by the direct piezo effect are measured and analyzed.

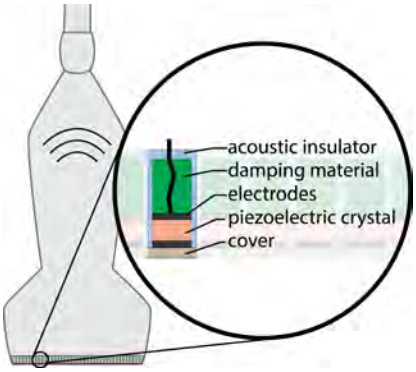

Figure 1.2: Schematic of an ultrasound imaging transducer.

The composition of an ultrasound transducer is complex, but the underlying principle is a piezoelectric crystal between opposing electrodes and an individual enclosure with an acoustic insulator (see figure 1.2). A dampening material ensures a steeper up- and down-ramping of the crystal oscillations and ensures a unidirectional emission of sound waves. Multiple piezoelectric elements are combined into an array and by selective and time-phased activation, complex waves can be generated.

1.2 Properties of ultrasound waves

Ultrasound pulses produced by the oscillatory crystal deformation will travel through the tissue as a pressure wave (see figure 1.3) The tissue undergoes cyclic pressure variations (compression and rarefaction) parallel to the longitudinal wave's propagation path. Local differences in acoustic impedance caused by solid objects or tissue interfaces (e.g. lumen vs. vessel wall, muscle vs. bone) will reflect the incident sound waves back to the transmitter (t_3 in figure 1.3), where it will be registered. The temporal difference between the emission and reception of a sound wave is due to the traveled path, which has to be twice the distance between transducer and object.

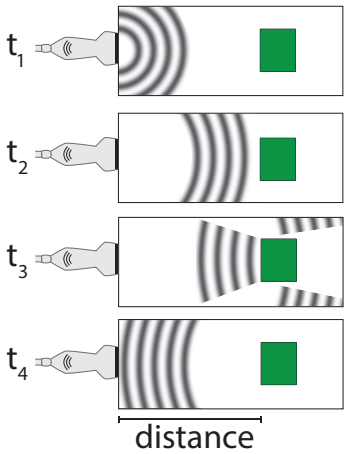

Figure 1.3: Propagation of a pulsed sound wave.

With knowledge of the propagation velocity, the depth of a signal reflection can be reconstructed. Because an emitted ultrasound pulse will travel through tissue with varying density, it will on its path produce a multitude of returning echoes. The detected voltages at the transducer will be amplified, filtered and processed (including demodulation, envelop detection, log compression etc.) and powerful computational capacity is needed to construct a real-time image.

An ultrasound wave is characterized by its sinusoidal frequency that falls between 2 MHz - 10 MHz for clinical ultrasound, but can even be used above 40 MHz for high-resolution imaging.

Pressure waves can be thought of as continuous sinus waves characterized by wave length λ and amplitude.

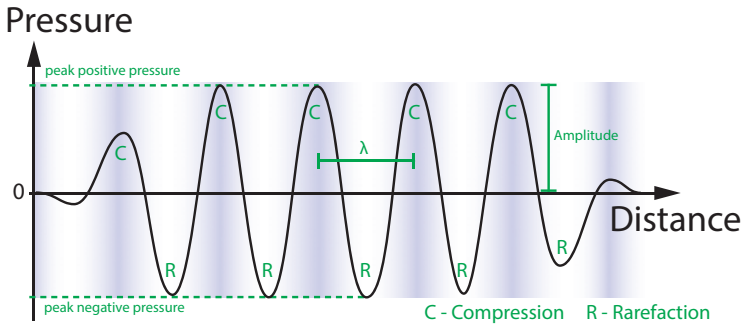

Figure 1.4: Pressure waves are characterized by amplitude and wave length λ. The pressure wave induces local compressions (C) and rarefactions (R) and propagates through matter with a certain velocity (air: 330 m/s, soft body tissue 1500 m/s and more than 4000 m/s for solids like bone).

The wavelength λ is the spatial dimension between two points with the same phase (from peak pressure nadir to peak pressure nadir) and depends on the propagation speed (c) and inversely on the frequency of compressions/rarefactions per second (f)

$$\text{Wavelength } \lambda = \frac{c}{f}. \tag{1.1}$$

Medical ultrasound with fundamental frequencies between 2 - 15 MHz typically has a wave length of 0.8 - 0.1 mm in tissue. The propagation speed is dependent on the matter that it travels through and averages 1'540 m/s for soft tissue. More exactly, the propagation speed c of a pressure wave depends on the tissue density ρ and compressibility κ and follows the equation

$$\text{Propagation speed } c = \sqrt{\frac{1}{\kappa\rho}}. \tag{1.2}$$

In soft tissue, ultrasound waves travel with 1'450 m/s (fat) - 1'580 m/s (muscle), while in hard tissue like bone the velocity exceeds 4'000 m/s.

The second parameter of a wave is it's amplitude. For ultrasound waves, amplitude is equal with the degree of tissue displacement transmitted as pressure. The maximal allowed value in diagnostic ultrasound is 4 MPa for peak negative acoustic pressure. The intensity I of an ultrasound wave is dependent on pressure P squared,

the tissue density ρ and the specific propagation speed c.

$$\text{Intensity } I = \frac{P^2}{\rho \times c} \tag{1.3}$$

When tissue density and propagation speed are assumed to be constant, the intensity of a soundwave is proportional to pressure squared.

$$\text{Intensity } I \propto P^2 \tag{1.4}$$

Manufacturers of ultrasound equipment are obliged to display real-time mechanical and thermal indices on the user interfaces as a metrical indicator to rate possible effects on the examined tissue. The mechanical index (MI) is an estimate of tissue damage by cavitation effects that happens at high pressure differentials. For diagnostic ultrasound, a value below 0.3 is accepted to not have any effect and the maximal allowed value for MI is 1.9. The mechanical index is a measure of peak negative pressure (P_neg) during a rarefaction divided by the square root of the center frequency f_c. It is determined for a ultrasound system in water where an attenuation-corrected peak negative pressure αP_r depending on penetration depth z_{MI} is measured with a hydrophone in respect to attenuation-corrected center frequency ($\sqrt{f_c}(c_{\text{MI}})$) at one focus point.

$$\text{Mechanical index (MI)} = \frac{\alpha P_{neg}(z_{\text{MI}})}{\sqrt{f_c}(c_{\text{MI}})}. \tag{1.5}$$

In diagnostic ultrasound exams with a 2.5 MHz transducer and a MI=1.3, these settings would result in peak negative pressures of 2 MPa and thus a total pressure differential of 4 MPa in a timespan of 0.2 µs. This is equivalent to a pressure change from 400 m below sea level to the surface in $^1/_{5'000'000}$th of a second.

1.3 Attenuation of ultrasound waves

However complex, the average intensity of an ultrasound beam that passes through an area of tissue can be expressed as

$$\text{average Intensity } I = \frac{\text{power [mW]}}{\text{area [cm}^2\text{]}}. \tag{1.6}$$

The cross section of an ultrasound beam will diverge with increasing penetration depth and the intensity is proportional to distance r squared. It should be noted that the maximal intensity is highest at the center of the beam and falls off towards the periphery.

$$\text{Intensity } I \propto \frac{1}{r^2}. \tag{1.7}$$

The loss in intensity (thus amplitude) of a wave over distance is called attenuation. It relies on interaction of pressure waves with the penetrated tissue that include reflection, scattering and absorption.

When a pressure wave arrives at a tissue interface of different acoustic impedance, it will be reflected as a specular or mirrored wave at a complementary angle $\theta_{\text{reflected}}$ to the incident angle θ_{incident}. Most of the signal detected in ultrasound imaging are specular reflections that have an incident angle θ_{incident} close to 90° at smooth boundaries.

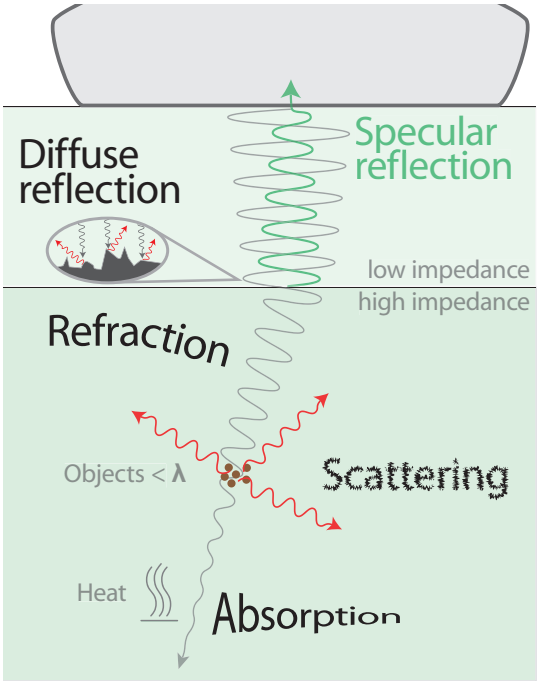

Figure 1.5: Representation of a continuous incident sound-wave that hits a tissue interface at 90° and is subsequently reflected back to the transducer where it can be detected. In case of irregularities at the interface, the wave can be reflected diffusely at various angles. Part of the wave's energy will pass through the interface where it gets refracted during the transition. If the wave hits objects smaller than its λ, it will be scattered. The mechanical energy of the wave is also transformed into heat and thus intensity absorbed in the tissue.

However, due to the non-homogeneous character of biological interfaces that contain irregularities in various sizes, part of the incident waves will be reflected diffusely, especially when the irregular structures have similar dimensions as the incident wave length. Diffuse reflections contribute to the decrease of a ultrasound waves' intensity over a traveled distance, but a large part of the reflected energy travels back to the transducer where it is detected. Structures much smaller than the wavelength, e.g. red blood cells that have a diameter of 7 μm vs. a typical ultrasound wavelength of λ= 500 μm will scatter the incoming sound wave in every direction (Reyleigh scattering) and only a small amount of the scattered sound waves will be detected at the transducer. The stochastic backscatter of diffuse reflections and most importantly the Reyleigh scattering at small structures are low in energy, but will give the tissue a characteristic texture or signature in 2-dimensional ultrasound images and allows computational intense tracking of these patterns.
In contrast to scattering and reflections, absorption is a gradual process that is mostly dependent on distance traveled, and the energy of a sound wave is converted from vibration into heat. The attenuation is expressed in decibels depending on the ratio between propagated and received intensity:

$$\text{Attenuation (dB)} = 10 \times \log_{10}\left(\frac{\text{received intensity}}{\text{propagated intensity}}\right) \tag{1.8}$$

In soft tissue, the attenuation coefficient α is around 1 dB cm^{-1} MHz^{-1}, which would translate into a decrease in signal intensity of 21% per cm and MHz. At an exemplary imaging depth of 1.5 cm, the received intensity of a 1 MHz wave would theoretically be only half of the propagated intensity (see table 1.1). The signals thus need to be amplified in accordance to their travel time in a step called time-gain compensation. For skeletal muscle, the average attenuation is greater than 1.5 dB cm^{-1} MHz^{-1} and differs profoundly when imaging is performed either longitudinal or orthogonal in respect to its muscle fibers. Lung tissue attenuates ultrasound waves even at a higher magnitude than air or bone (see figure 1.14) due to the small air-filled pockets formed by alveoli, which help re-

Table 1.1: Attenuation in dB to the ratio of $\frac{\text{received signal}}{\text{propagated signal}}$

dB	ratio
0	1:1
-3	1:2
-7	1:5
-10	1:10
-20	1:100
-30	1:1'000
...	...

fracting the incident wave effectively. Ultrasound waves with higher frequencies will be attenuated over a shorter distance and thus will penetrate tissue to a lesser depth than lower frequency waves as it is shown for e.g. 3.5 MHz, 7 MHz and 15 MHz in muscle in figure 1.14.

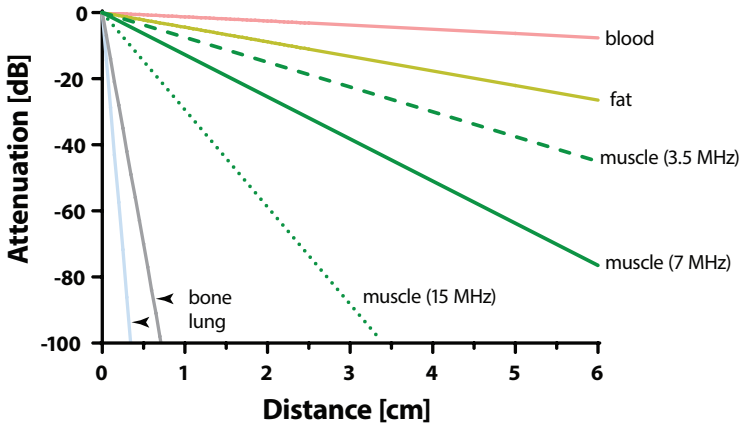

Figure 1.6: Theoretical attenuation for imaging with 7 MHz in respect to traveled distance for selected tissues. Blood does show the smallest attenuation in contrast to bone and lung. For muscle, three different frequencies are shown. Waves with a higher frequency show a faster attenuation over travel distance than waves with lower frequencies.

1.4 Ultrasound beamforming

Ultrasound imaging is performed with short pulses of sound waves, instead of a continuous transmission. In fact, transducers for diagnostic ultrasound are only very briefly active, transmitting sound waves only during 0.1 - 2 % of the pulse repetition period and register reflected signals during a much longer listening period. The pulse duration, pulse cycle and number of pulses per time are important parameters for the imaging process that influence imaging depth, resolution and frame rate of real-time images.

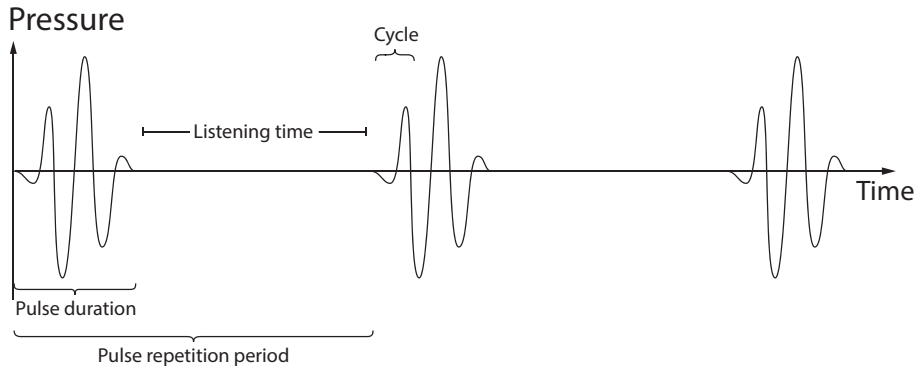

Figure 1.7: Simplified example of pulsed ultrasound imaging. Here, 3 short pulses with 3 cycles are shown. During the pulse repetition period, a short pulse is transmitted and the transducer returns to quiescent stage and detects returning echos. A typical pulse repetition period in diagnostic ultrasound lasts between 0.1 and 1 ms.

Modern transducers possess between 32-256 crystals depending on probe type and imaging applications. These crystals are usually not excited as singular sequential chain to generate waves with a single-point source. Instead, they are organized in arrays, small groups of crystals, that can fire simultaneously and would results in a straight ultrasound beam with straight propagation. Crystals of a single array can be excited differentially as well, offering the possibility to focus and/or steer the resulting wave front (see figure 1.8).

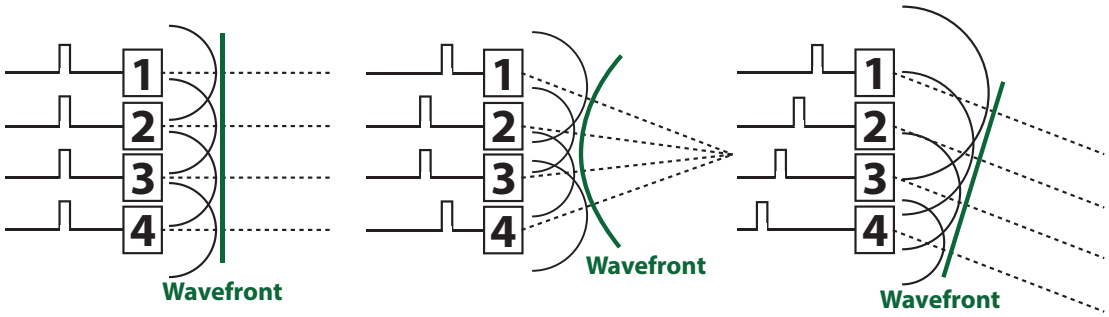

(a) Un-focused **(b)** Focusing **(c)** Steering

Figure 1.8: The crystals in ultrasound transducers can be bundled into arrays and activated simultaneously, as it is shown here for a theoretical 4 crystal array.. **(a)** A Linear pattern is achieved when the crystals are all excited simultaneously. The wavefront will progress straight into the tissue. **(b)** Focusing of an ultrasound beam is achieved by differential phasing of an array, which produces a focused wavefront with a focal point. **(c)** Phasing of an array can also be used to steer the wave front.

1.5 Ultrasound resolution

However, the existence of multiple sound waves at the same time will result in constructive and destructive interference that result in local amplification and extinction of sound pressure levels. The beamforming, that is the control of interference patterns in ultrasound imaging is complex but designed to generate optimal acoustic pressure at the desired imaging point.
The resolution in ultrasound imaging rests on three pillars: spatial resolution, temporal resolution and contrast resolution.

Spatial resolution is the ability of the ultrasound system to distinguish 2 different structures at a certain depth. For ultrasound, the spatial resolution has 2 dimensions: lateral (perpendicular to the imaging axis) and axial.
Unfocused transducers will transmit wavefronts that lead to huge amplitude change close to the source, which is called near-field or Fresnel's Zone (see figure 1.9). Further away in what is termed far-field, the intensity will change less dramatically and the ultrasound beam spreads. For medical ultrasound, transducers with a long near-field are preferred, because the intensity as well as lateral resolution is higher, which allows to distinguish two structures at a certain depth perpendicular to the sound waves.

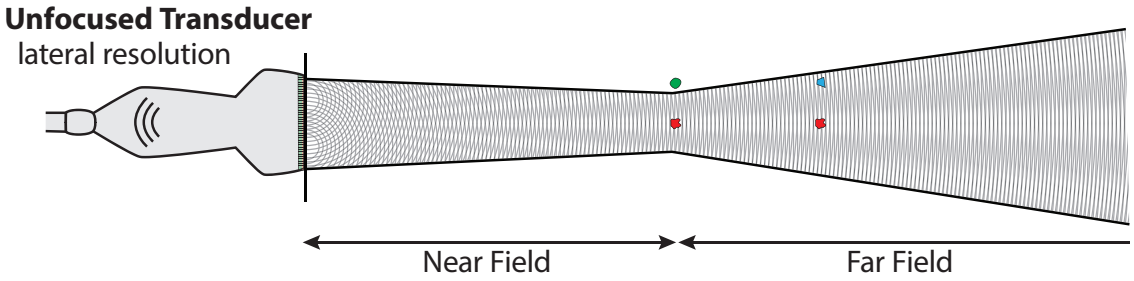

Figure 1.9: Here, two theoretical waves are drawn to show the interference patterns. Unfocused transducer have a "natural" focus point between a near-field (Fresnel's zone) and a far-field. The unfocused transducer can resolve laterally the green and red structures at the near-field but fails to resolve blue and red in the far-field.

Focused transducers with their phased arrays will generate an ultrasound beam with a focal zone (see figure 1.10). In this focal zone, the beam width is minimal and the amplitude can be more than 100-fold higher compared to areas outside the zone.

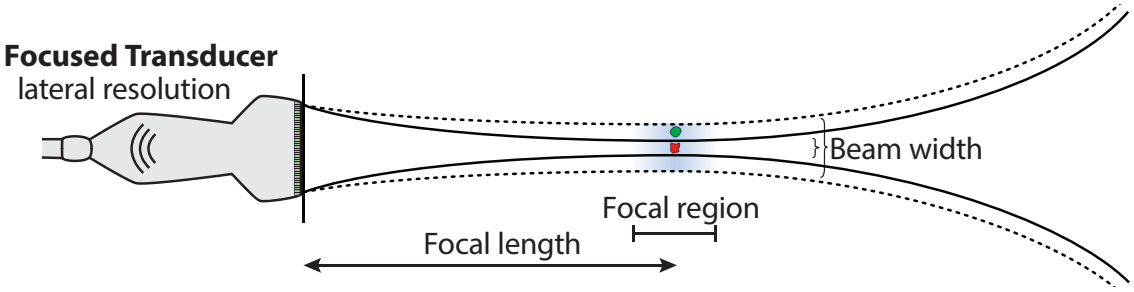

Figure 1.10: Focused transducers show a very narrow beam width at the focal region. Smaller beam-widths increase the lateral resolution. The larger beam shown here in dashed lines cannot resolve the two structures.

Axial resolution (or longitudinal) is the minimal spatial dimension between two structures parallel on the imaging path that the ultrasound system can yet distinguish (see figure 1.11). It is determined by the frequency and the spatial pulse length. Higher frequencies and shorter pulses yield a better resolution. The spatial pulse length itself is defined by the number of cycles and the wavelength. Therefore, axial resolution is best when high frequency transducers with a strong crystal dampers are used. Unfortunately, these conditions favor strong attenuation as well and thus limit the signal-to-noise ratio due to the dampening and ultimately the penetration depth. However, the axial resolution does not vary with imaging depth as the lateral resolution does.

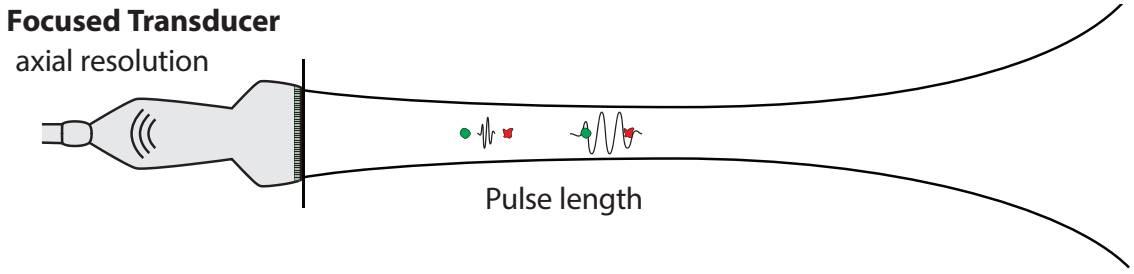

Figure 1.11: Focused transducers show a very narrow beam width at the focal region. Smaller beam widths increase the lateral resolution. The axial resolution is determined by the spatial pulse length (number of cycles, wavelength)

Temporal resolution of an ultrasound system depends on 3 factors: the number of scan-lines, the depth of imaging and the number of focus points.
The wider the acquired frame is, the more scan-lines have to be used. By reducing the image width, a frame can be acquired quicker and a next frame started earlier, thus increasing the frame rate.

The reduction of the imaging depth increases the possible frame rate as well, because for each scan-line, the waiting period can be reduced to detect only signal to a certain depth.
Multiple focus points have the side effect, that for each focus point, all scan lines have to be duplicated which impacts the frame rate significantly.

Contrast resolution is determined by the acoustic differences of adjacent structures and the processing (digital sampling, compression) that results in a discernible difference in intensity in an ultrasound image. The acoustic differences between tissues can be very small so that there is no clear delineation in the anatomical ultrasound images. Application of ultrasound contrast agent will increase the echogenicity of blood, which increases the contrast of the blood circulating in organs and tissue.
The returning echoes that the ultrasound image is reconstructed from, can vary in their amplitude over several magnitudes ($> 10^{12}$). During the signal processing, this acquired raw data is compressed to be stored and displayed. The ratio of the lowest powered to the highest powered echoes is expressed as dynamic range

$$\text{Dynamic range (dB)} = 10 \times \log_{10}\left(\frac{\text{highest power}}{\text{lowest power}}\right). \tag{1.9}$$

Usually, the compression is selected between 30 dB to 60 dB which would translate to a signal ratio of 1:100 to 1:1'000'000 respectively. The reconstructed images then are stored as gray scale image sequences with a bit-depth of typically 8 bit, allowing 256 different values per pixel.

1.6 Ultrasound imaging modes

The most prominent mode of operation in medical imaging is the 2-dimensional B-mode (or brightness-mode). B-mode offers a real-time image of brightness-modulated echoes that originate from structures in the imaging plane.
In M-mode (or motion-mode) imaging, a single scan line is used to reconstruct a 1-dimensional B-mode image to assess motion of the tissue boundaries.

In Doppler Mode, moving particles or structures can be characterized by their movements. Measurements of frequency shifts in reflected echoes of moving particles (predominantly erythrocytes) can be used to determine their velocities. The velocity information can then be presented as a color-coded overlay on B-mode images. Red colors indicate particles moving towards the transducer and blue colors indicating particles moving away (see Figure 1.12).

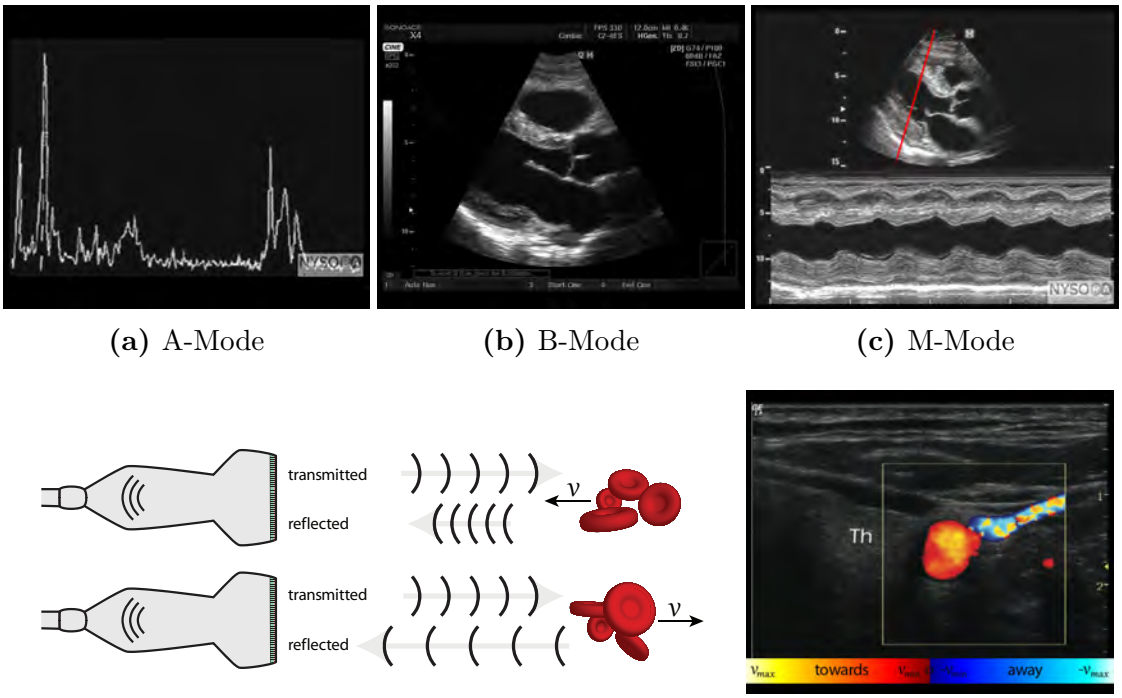

(a) A-Mode **(b)** B-Mode **(c)** M-Mode

(d) Pulsed-Wave Doppler Principle **(e)** Color Doppler Mode

Figure 1.12: Example of the display modes in ultrasound imaging. **(a)** A-Mode (Amplitude): For a single scan-line the echoes are plotted as a function of depth. **(b)** B-Mode (brightness): 2-Dimensional representation of all acquired scan-lines formed into a brightness-modulated image. **(c)** M-Mode (motion): B-Mode representation of a single scan line (marked red) to monitor the tissue motion. **(d)** Pulsed-wave Doppler principle. Ultrasound pulses will be reflected with a frequency shift depending on the movement of the reflective particles. **(e)** Color Doppler Mode. Velocity information is presented as a color-coded overlay on top of a B-mode image with red colors indicating moving particles towards the transducers and blue colors indicating particles moving away.
Ultrasound Images from http://www.nysora.com

1.7 Contrast enhanced ultrasound

Depending on the imaging conditions, some tissue-interfaces will have a similar acoustic impedance. A liver for instance can present with a non-suspicious appearance on anatomical B-mode images. However, when contrast agent is applied that increases the echogenicity of blood and thus blood vessels, an extensively vascularized liver tumor can become clearly visible as shown in figure 1.13

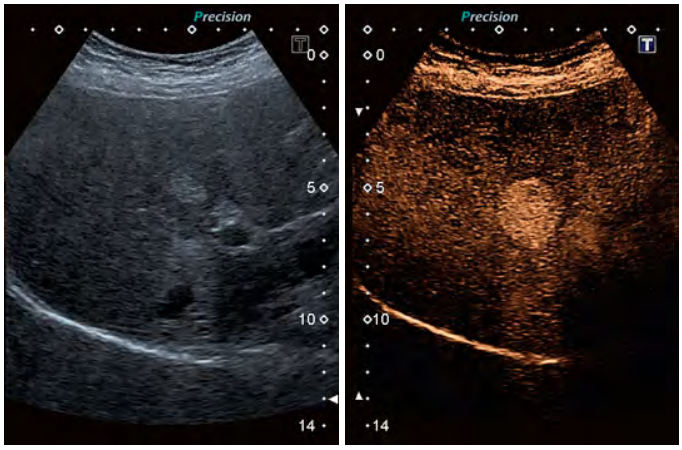

(a) Anatomical B-Mode **(b)** Contrast B-Mode

Figure 1.13: Ultrasound imaging of a liver tumor **(a)** without contrast agent or **(b)** with a contrast agent. Images from Toshiba Medical Systems Europe.

The contrast agents used in ultrasound imaging are acoustically reflective particles like liposomes and nano-particles that possess small gas-pockets which increase the particle's echogenicity. The most common and effective contrast agent for ultrasound are microbubbles between 1-6 μm in diameter that possess a gas-filled core.

1.7.1 Structure of Microbubbles

Microbubbles as a contrast agent have been accidentally discovered by intra-cardiac injections in the 1960s, when ultrasound images of the aorta showed a brief increase in contrast. The effect was due to fine air-bubbles that have been formed at the catheter tip while injecting. However, they were frail and disintegrated quickly by coalescence, fragmentation and shrinking through diffusion.
By encapsulation with either proteins (e.g. albumins), polymers (cyanoacrylate) or

by a phospholipid monolayer, the half life of the microbubbles increases dramatically and can modulate specific properties regarding acoustic character, biofuntionality or stability.

Shells consisting of polymers or proteins are characterized by their rigid character, and although they expand and contract in a pressure field, the generated echoes are of smaller intensity compared to microbubbles that possess a semi-fluid lipid-layered shell. In addition, the use of lipid layer allows for a stoichiometric composition and thus dynamic control over the properties of the shell even after the assembly of the microbubble.

The use of functionalized lipids bearing biotin-, maleimide- or NHS-groups allows the microbubble to have additional properties to the reflection of ultrasound waves.

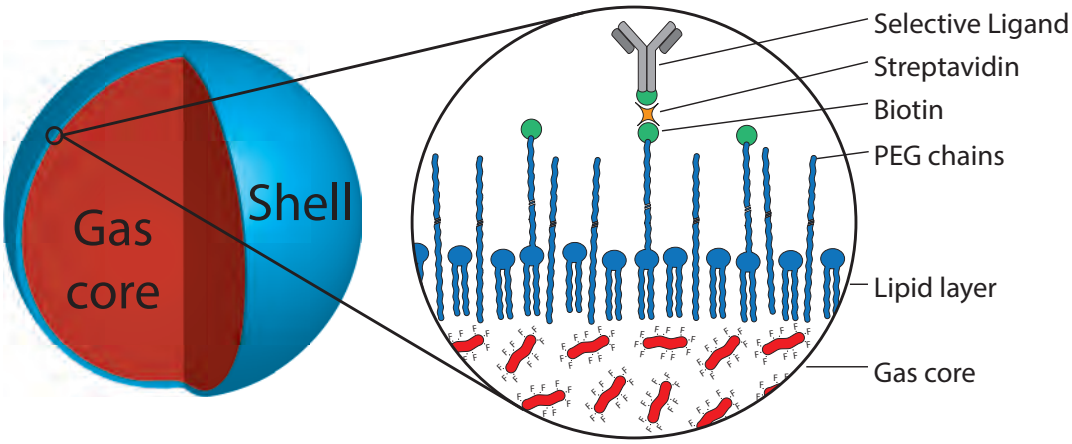

Figure 1.14: Microbubbles consists of a gaseous core surrounded by a shell made mostly from proteins, polymers or phospholipids. They are between 1-6 μm in diameter. Selective ligands can be attached to the microbubble shell via functionalized lipids as it is shown here using biotin-streptavidin chemistry. Polyethylene glycol (PEG) chains form a protective layer around the microbubble to prevent Ostwald ripening (fusion of microbubbles). The used gas usually has a high molecular weight and a low diffusivity and here, Perfluorobutane (C_4F_{10}) is shown exemplary.

The gas-core optimally consist of an inert gas with a low diffusion coefficient and low solubility in blood, for example sulphur hexafluoride or perfluorobutane.

Once microbubbles are assembled, the core-gas will diffuse slowly out of the microbubble across an osmotic gradient into the surrounding and the diameter of the microbubble will decrease. For highly soluble gases like oxygen, nitrogen or carbon-dioxide, the persistence is of several magnitudes shorter compared to large molecule gasses.

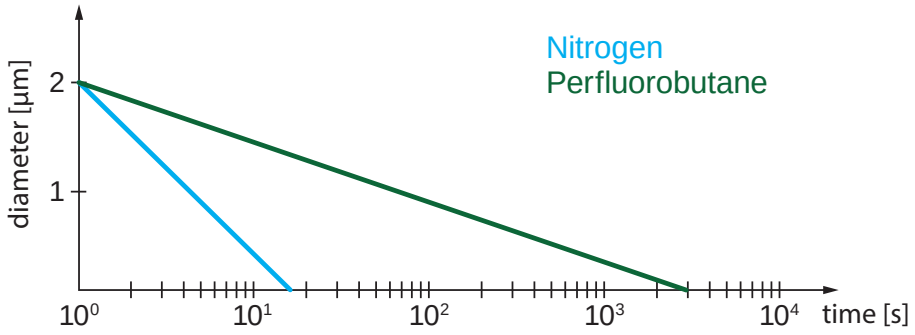

Figure 1.15: Microbubble persistence *in vivo* depending on the core gas. Gases with lower diffusion coefficient (e.g. Perflurcarbons) show a slower microbubble shrinking due to loss of internal gas pressure than gases with a higher coefficient (e.g. Nitrogen).

1.7.2 Microbubble behaviour in an ultrasound field

When microbubbles are placed in an ultrasound field with periodically changing pressure, they start to oscillate by cyclic expansion and compression. The degree of oscillation is dependent on the frequency of the incident ultrasound beam and the acoustic intensity. An individual microbubble has a specific resonant frequency at which it will oscillate most effectively.

This frequency does show an inverse hyperbolic relation to the microbubble diameter and is further determined amongst others by the microbubbles shell-elasticity and the surrounding dampening.

Linear oscillation

In pressure fields with low acoustic power insonation of a peak pressure <100 kPa, microbubbles will oscillate in a linear manner with the same frequency as the exciting soundwave (see Figure 1.16a).

The back scatter that will be detected at the transducer will be of several magnitudes higher than the back scatter from red blood cells thus opacifying the blood but the signal will not differ qualitatively, thus backscatter is only enhanced.

Non-linear oscillation

Within pressure fields of moderate intensities of peak pressures between 0.1-1 MPa, microbubbles will show non-linear behavior (see Figure 1.16b). Gas-filled microbubbles will expand in low pressure much quicker and to a greater extent than they can be compressed under high pressure and thus will stay longer in a expanded state.

Because of its non-linear behavior, a microbubble will have a different diameter each time it encounters the periodically reoccurring pressure maxima and minima. This will lead to a different backscatter and applied force on the shell that will influence the oscillatory behavior.

Another effect of this non-linear behavior is the generation of harmonic and subharmonic oscillations that microbubbles can undergo as well. This behavior will result in backscattering of sound wave at multiples (harmonics) and half (subharmonics) of the incident fundamental frequency.

Disruption

If the incident ultrasound beam exceeds a pressure >1 MPa, the microbubble will oscillate in an erratic manner and the forces lead to a shell rupture and microbubble destruction (see Figure 1.16c).

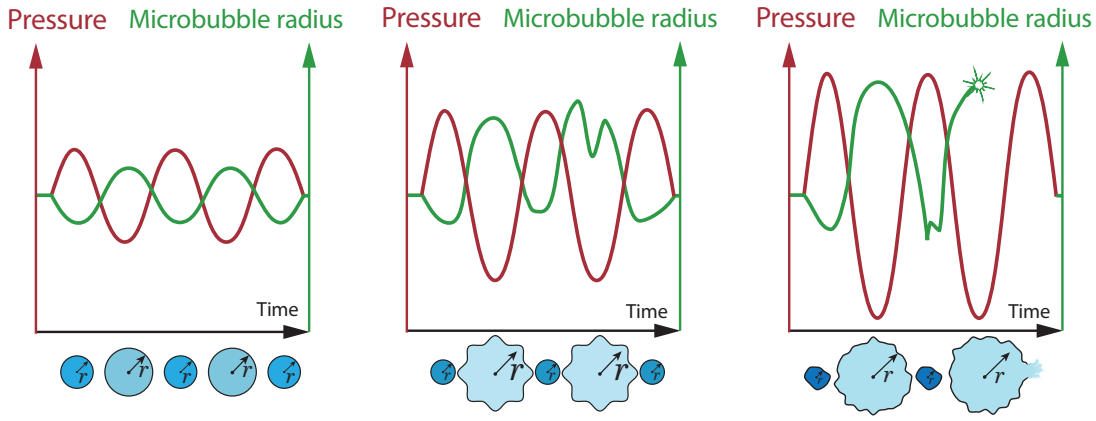

(a) Low pressure **(b)** Moderate pressure **(c)** High pressure

Figure 1.16: Microbubble behaviour in a cyclic pressure field. **(a)** Under low acoustic power insonation, a microbubble will oscillate with a linear change of its radius. **(b)** With higher pressure however, the behaviour of a microbubble becomes non-linear and it will produce a harmonic response as well. **(c)** With further pressure increase, the microbubble will start oscillate erratically and will eventually burst.

1.7.3 Contrast enhanced ultrasound imaging techniques

The resulting back-scatter from microbubbles are thus special in at least two ways: they show a complex intensity pattern that will differ from linear responses of tissue and they show harmonic and sub-harmonic components. For contrast-enhanced ultrasound imaging, various strategies are possible that utilize these differences.

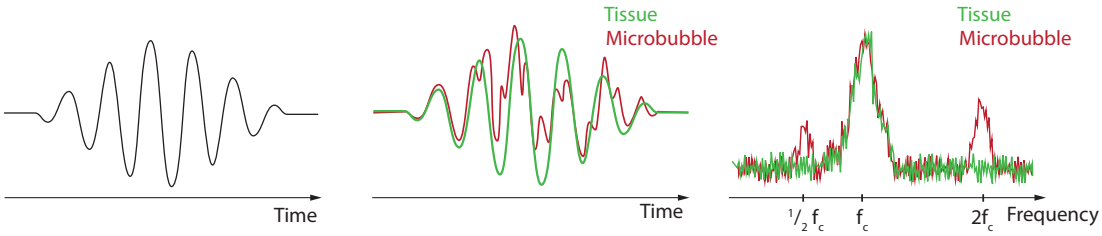

(a) Incident pulse **(b)** Returned signal **(c)** Frequency spectrum

Figure 1.17: Differences of signals from tissue and microbubbles. **(a)** Intensity of an incident sound pulse over time that will produce returns originating either from tissue or microbubbles. **(b)** The intensity of echoes from tissue resemble the linear oscillation of the incident soundwave while the signal from microbubbles show non-linear and irregular intensity changes. **(c)** The frequency spectrum for tissue will show a single peak at the fundamental frequency f_c of the incident sound wave while the spectrum for microbubbles will show sub-harmonic ($\frac{1}{n}f_c$) and harmonic (nf_c) components as well.

Cadence Contrast Pulse Sequencing (CPS) Technology

Cadence contrast pulse sequencing (CPS) is a advanced ultraound imaging protocol to distinguish acoustic signals from microbubbles and tissue. The imaging protocol is based on three principles: pulse inversion, power modulation and harmonic imaging.

In CPS, three successive ultrasound pulses are transmitted with a second pulse that is special in two ways.

Firstly, the second pulse at t_2 has a phase of 180° compared to the first and third pulse at t_1 and t_3 respectively, which is called pulse inversion.

Secondly, the second pulse at t_2 has a amplitude that is exactly twice as high compared to the first and third pulse at t_1 and t_3 respectively, which is called power modulation.

The backscatter from for these three pulses will be combined according to the travel time. For tissue, with a predominating linear response, the signals will cancel each other out, resulting in no signal after the combination. For microbubles, how-

ever, their complex backscatter that is caused by the non-linear behavior will result in a clear signal that differentiates the signals received from microbubbles.
For harmonic imaging, the same principle will result in an eliminated signal after combination for tissue, but in a clear signal for microbubbles.

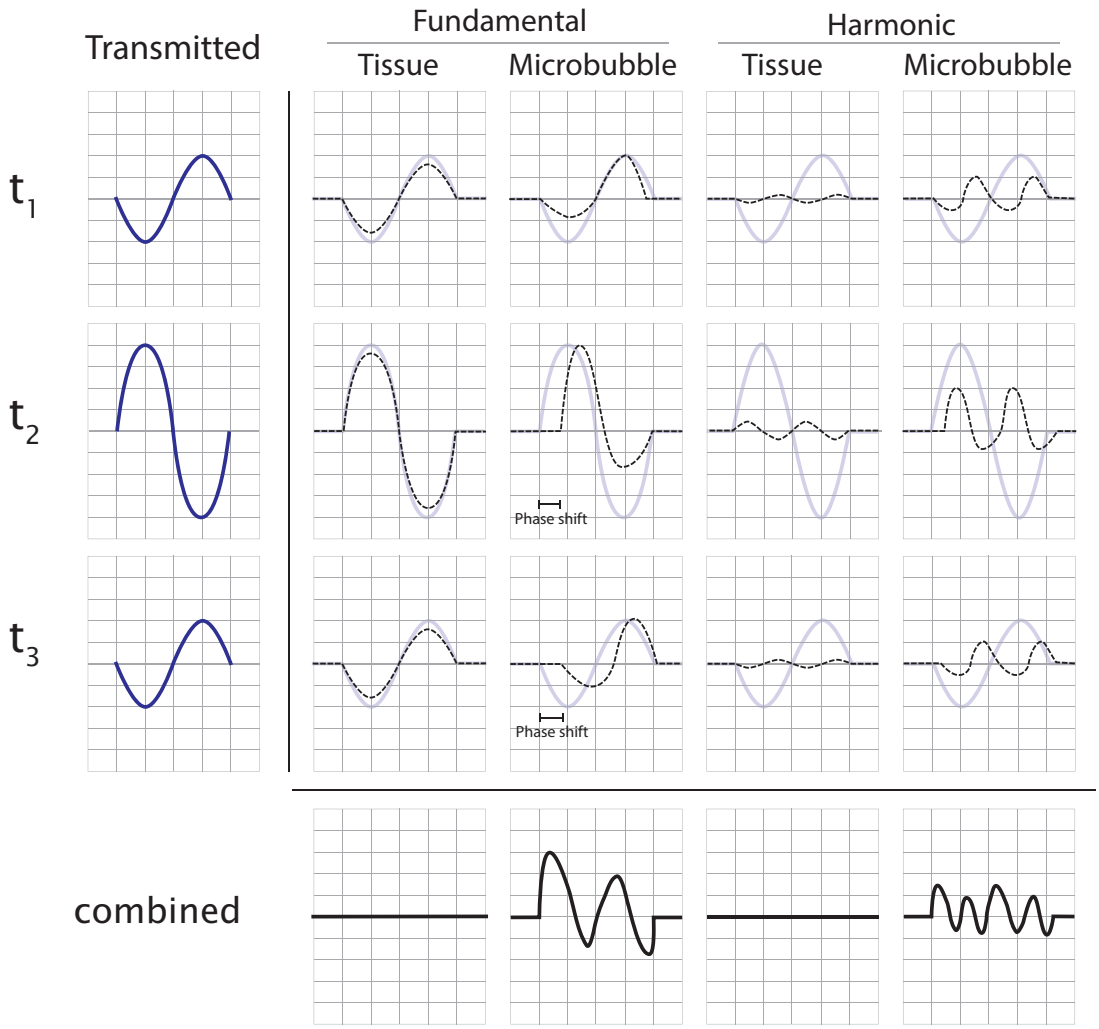

Figure 1.18: Simplified imaging protocol for Cadence contrast pulse sequencing used to differentiate signal of microbubbles from tissue.
A sequence of three pulses are transmitted. The second pulse at t_2 is inverted by 180° with an amplitude twice as high as t_1 or t_3.
Signals with the same travel time are combined and total results for tissue are canceled out. Microbubbles produce a complex backscatter due to their non-linear behavior, including phase shift, that results in a signal after calculation.
The tissue react mostly with the fundamental frequency of the transmitted sound-pressure and show no harmonic behaviour. Microbubbles, however, oscillate not only with at the fundamental, but also at harmonic and sub-harmonic frequencies that can be utilized as well to detect backscatter originated from microbubbles.

1.7.4 Requirements of contrast enhanced ultrasound agents

In ultrasound molecular imaging there are specific requisites both for the targeted contrast agents as well as the targeted epitopes (see figure 1.19).

The epitopes that can be targeted with microbubbles are limited to the endothelial surface, because the diameter of microbubbles prevents them to pass the endothelial barrier. However contrast enhanced ultrasound of extravascular epitopes is possible with the use of echogenic liposomes or perfluorocarbon nanoparticles. The epitopes in question optimally is specific for the disease or condition and is not expressed ubiquitously in the whole vascular system.

The targeted contrast agent optimally has a high ligand density on its surface to maximize adhesive bonds. For optimal imaging results, the ligand itself needs to have a high affinity to facilitate quick binding to its target and a high specificity to minimize cross-reactivity. The ligand:epitope interaction is vital for the targeted imaging process and inhibitors or proteases that reduce the ligands capabilities to bind the epitope or shear forces that prevent the molecular interaction will decrease the specific molecular imaging signal.

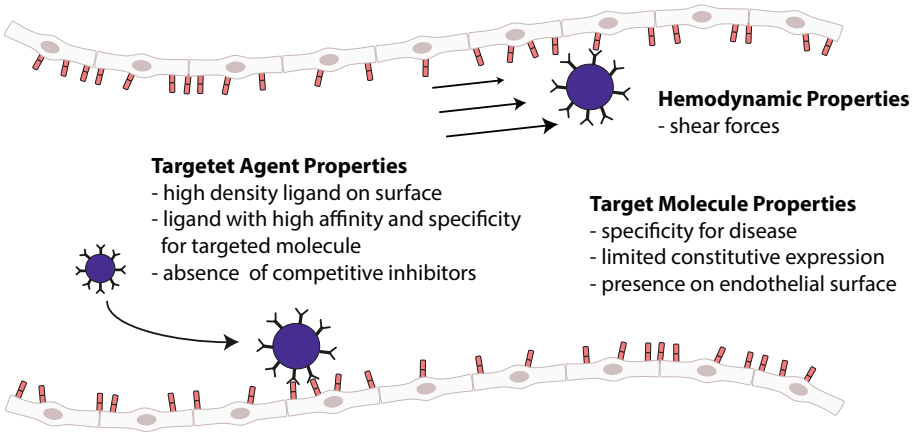

Figure 1.19: Requirements for molecular ultrasound imaging. The targeted agent optimally has a high density ligand on its surface with high affinity and specificity for the epitope in question.
The targeted molecule (epitope) optimally is specific for the disease and has a limited expression. Only epitopes present on the endotheliala surface can be targeted by microbubbels with a diameter of >1 μm.
Least, the contrast agent has to be able to tolerate the shear forces present in the vasculature at least for a short term to allow imaging.

1.7.5 Application protocols for contrast enhanced ultrasound

Contrast enhanced ultrasound can be used to answer several questions. For example it can be used to opacify the microvasculature in organs to assess a malignant development. The imaging can be performed after a short latency to allow a homogeneous distribution of the contrast agent.

However, the use can be extended beyond backscatter enhancement.

Dynamic assessment in perfusion imaging

When the injected microbubbles are homogenously distributed in the circulation, the signal enhancement is evident in almost every tissue. But taking advantage by the vulnerability of microbubbles, they can be strategically destroyed in an imaging plane.

One application is the perfusion imaging of a tissue to assess blood flow. In echocardiography, the quantification of blood volume and blood flow in the myocardium can be achieved by a continious injection of microbubbles to ensure a homogeneous distribution in the circulation. The image intensity in an assessed tissue volume will be constant at an intensity platea (see figure 1.20). Several high intensity ultrasound pulses with a maximum MI of 1.9 can now be used to destroy all microbubbles present in the imaging plane and the signal intensity will be severely reduced. When the intensity is minimal, the contrast enhanced imaging will be switched to a lower MI to allow a non-destructive imaging. The blood flow will bring new microbubbles into the imaging plane and after a period of time the plateau intensity will be reached again because the microbubble pool in the circulation is undisturbed by the locally applied destruction pulses. By monitoring the dynamical signal increase over time, the plateau and the rate of replenishment can be quantified.

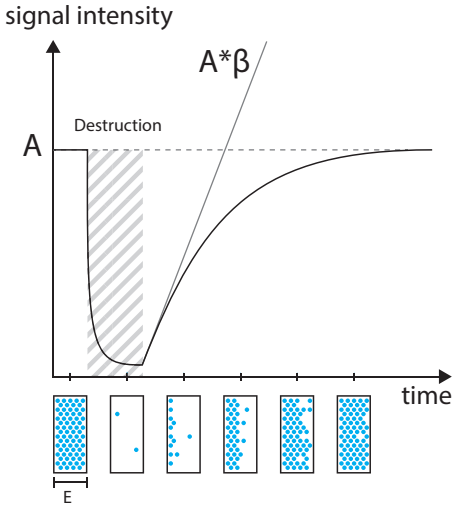

Figure 1.20: Intensity function of myocardial perfusion in a tissue volume penetrated by ultrasound beam with elevation width E. Intensity plateau A is re-established after destruction with an initial blood flow represented by A×β.

Assessment of signal in ultrasound molecular imaging

Targeted microbubbles can be used to assess the expression of an epitope on the endothelial surface with the use of non-invasive ultrasound.

A bolus of targeted microbubbles is injected into the circulation and a subsequent latency of 5-10 minutes allows a homogeneous microbubbles distribution throughout the circulation. During the equilibration time, targeted microbubbles that have been conjugated with a ligand or are assembled with a specific shell element will adhere to their specific target. The amount of free floating microbubbles on the other hand will be reduced over time through phagocytosis by hepatic kupffer cells.
The total video intensity of a taken ultrasound image is the sum of signals generated both from adhered and freely circulating microbubbles (see figure 1.21).

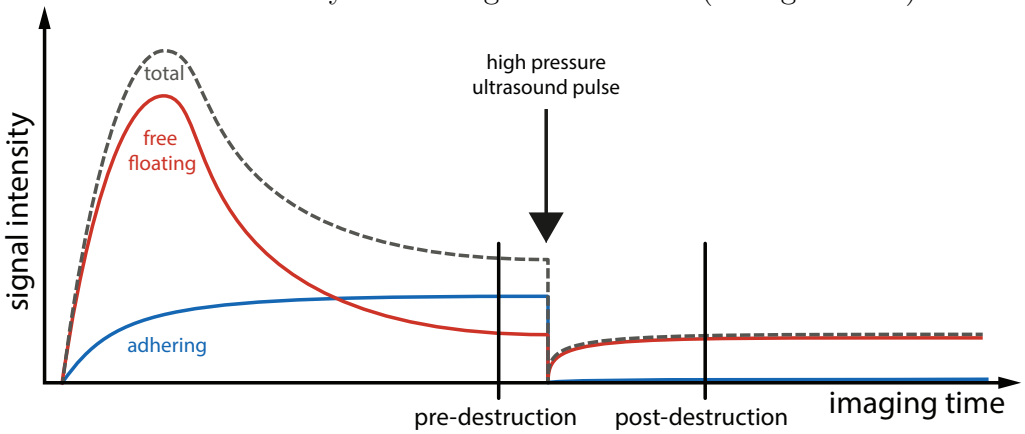

Figure 1.21: Schematic representation of molecular imaging. A bolus injection of microbubbles will increase the total signal intensity. A period of 8 minutes allowed adhesion of microbubbles. A pre-destruction frame was captured before a high pressure ultrasound pulse during multiple frames was used to destroy all microbubbles in the imaging plane. Molecular imaging data of adhered microbubbles were determined by the difference of pre- and post-destruction frames.

To assess the video intensity that is generated by adhered microbubbles alone, an inverse approach is used. A pre-destruction frame is acquired that consists of both signals generated from adhered as well as freely circulating microbubbles. All existing microbubbles in the imaging plane will be destroyed by application of multiple high intensity ultrasound pulses to ensure total destruction all microbubbles in the imaging plane. The total amount of microbubbles freely circulation is of several magnitudes higher than the number of microbubbles in the imaging plane, so that the reservoir of circulating microbubbles is not affected by a destructive pulse over a short period.

After the destruction period, a post-destruction frame is recorded that does consist predominantly of signal from freely circulating microbubbles in the tissue and will serve as a base-line. Subtraction of pre- and post-destruction frames will yield the signal intensity of adhered microbubbles.

2 Contrast Imaging in acute Myocarditis

2.1 Introduction

Myocarditis is defined as inflammatory infiltration of the myocardium with myocyte degeneration and necrosis in the absence of ischemia [1]. It has been found in 1-9% of routine autopsies [2], and in a higher proportion (5-12%) in young individuals with sudden unexplained cardiac death[3]. This is in contrast to the perceived low frequency of a diagnosis of myocarditis in patients.
Myocarditis can be caused by a variety of infectious agents, including viruses, bacteria or other pathogens but can as well be secondary to autoimmune pathologies and other exposures like systemic diseases, drugs and toxins [4] (see Table 2.1).

The most frequent cause for myocarditis are cardiotropic viruses 2.1 [5, 6] with Coxsackie B3 being responsible for half of the observed cases. Interestingly, only few viruses inflict direct cardiomyocyte damage. For example Coxsackie virus B3, which infects a variety of cell types including lymphocytes, macrophages, fibroblasts and cardiomyocytes and leads to virus-mediated cell-lysis. Virus-mediated cell lysis and more importantly the ensuing immune response that is targeted against infected cardiomyocytes [7] leads to a pro-inflammatory milieu that amplifies myocardial tissue damage and dysfunction.
In contrast, most viruses induce myocardial damage only indirectly via inflammatory pathways. For example, HIV or Parovirus B19, that predominantly infect T-cells and macrophages or endothelial cells, respectively [8] do not lead to direct myocyte damage.For these viruses, the exact link between infection and myocardial damage is less well understood but autoimmune processes seem to be the decisive.

Table 2.1: Various causes of Myocarditis. Adapted from Sagar et al. [4]

Causes	Etiologies
Viral	Coxackievirus, Adenoviruses, HIV, Hepatitis C virus, Parvovirus B19, Influenza viruses
Bacterial	Legionella, Mycobacterium tuberculosis, Corynebacterium diptheriae, Staphylococcus aureus
Fungal	Candida, Aspergillus
Parasitic	Trypanosoma cruzi, Toxoplasma gondii
Autoimmune diseases	Giant cell myocarditis, Rheumatoid arthritis, Celiac disease, Sarcoidosis, Scleroderma
Hypersensitivity	Allergic reactions e.g. against Penicillin,
Toxins	Ethanol, Arsenic, Chemotherapeutic agents

2.1.1 Pathogenesis of Myocarditis.

Most of our understanding of myocarditis has been gained by work on animal models, specifically on small rodents. The artificial induction of myocarditis can be achieved in laboratory models by either infecting the mice with cardiotropic viruses (e.g. Coxsackie B3) or challenging the immune system with self-peptides (e.g. cardiac myosin) to induce cardiomyocyte damage. In the latter, the immune system is activated by a challenge with strong boosting adjuvants that maximize the cell-mediated immune reaction (e.g. inactivated mycobacteria in mineral-oil). To optimize the induction rate, the animals usually are treated prior to peptide-vaccination with Pertussis toxin to induce lymphopenia in the $CD4^+CD25^+$ regulatory T-cell population to remove their dampening control on B- and T-cell effector function [9].

Acute Phase. In the acute phase of virus-induced myocarditis (see figure 2.1), infected cardiomyocytes are recognized by natural killer cells and driven into apoptosis. The first line of defense are residing macrophages, dendritic cells and a wave of invading neutrophil and natural killer cells that help clearing the virus and cell debris. This innate mechanism helps to control the virus titer effectively but due to the secretion of granzyme and perforin and the accumulation of cell debris, the surrounding myocardial tissue can be damaged extensively.

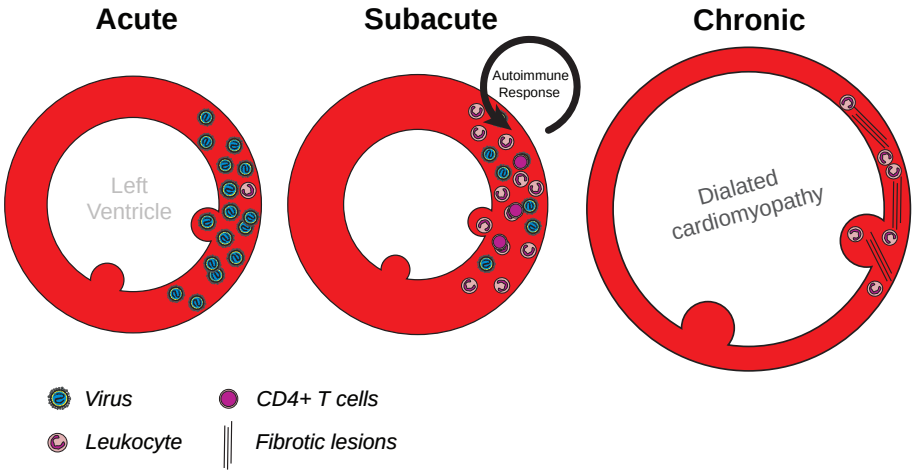

Figure 2.1: Stages of myocarditis. In the pathogenesis of myocarditis, direct viral injury during the acute phase and the ensuing host immune response with leukocyte infiltration during the subacute phase can lead to dilated cardiomyopathy with fibrosis and reduced systolic function in the chronic phase. CD4 positive T-lymphocytes are crucial in mediating the autoimmune response in the subacute phase by secreting interleukin 17.

Residing dendritic cells and macrophages detect pathogens with pattern recognition receptors (e.g. Toll-like receptors, C-type lectin receptors etc.) and secrete pro-inflammatory soluble mediators, most importantly TNFα, IL-6, Nitric oxide and IL-1, which can worsen tissue damage further [10].
The expression of TNFα, IL-6, and IL-1β was found to be essential for development of EAM [11]. One specific action of TNFα in the autoimmune processes is the increased activation of residing dendritic cells that have a central role in the pathogenesis of myocarditis .

Subacute Autoimmune Phase. The immune response has as its goal virus clearance and it has been shown that with viral persistence is much worse (requirement for transplantation, sudden death) [12] Once viral reproduction is controlled, the immune system should be down-regulated.
However, due to the intense inflammatory milieu and non-specific cellular damage, certain processes can initiate auto-immune pathways. Although the processes involved are less well understood, they include collateral activation of auto-reactive $CD4^+$ T-cells and molecular mimicry of virus antigens. Here, epitopes are shared between virus and cardiac proteins or polysaccharids that trigger T-cell activation against intrinsic self-antigens. Virus antigens may also trigger a predominant re-

sponse that activate more $CD8^+$ cytotoxic T-cells that additionally fuel the immunologic circle, which leads towards auto-immunity and is usually driven by T_h1 cells [13].

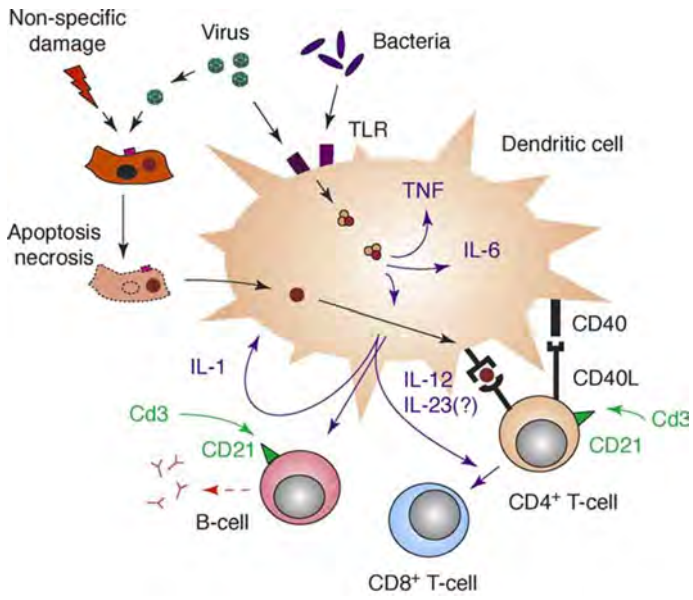

Figure 2.2: Role of dendritic cells in Myocarditis. The interaction of $CD4^+$ cells with DC via the antigen:T-cell receptor axis and a survival-signal via CD40:CD40 Ligand axis can lead to the expansion of auto-reactive B- and T-helper cells and a prolonged $CD8^+$ T-cell activity. Pro-inflammatory cytokines as TNFα, IL-1, IL-6 and IL-12 keep the activation on a persistent level. Adapted after [14].

The cytokine profile in the inflamed spots however, is dominated by TNFα, IL-6, -1, -12, -23, IL-4 and -17, secreted predominantly by natural killer cells, dendritic cells and macrophages. With the influx of T-cells, that is initiated around day 7 in the induced animal models and peaks around day 21, the cytokine profiles would determine a shift to either a T_h2 response (B-cell activation, humoral immunity, IL-4, -5 , -10 and IgE production) or a T_h1 response (hypersensitivity, macrophage activation, pro-inflammatory T-cell response with IFN-γ and IL-12) [15].

However, the balance of pri... (alte text) is variable for at least two reasons

First, there seems to be a differences between animals with genetic background in models of myocarditis, regarding the pathological severity and prevalence. Induced autoimmune myocarditis provokes a T_h2 cytokine profile in A/J mice that can be blocked with anti-IL-4 antibody [16], while in other strains or in lewis rats myocardi-

tis is promoted by a T_h1 response [17]. Similarly, female BALB/c mice lacking the IL-4 receptor are not protected against the development of myocarditis, which is in contrast to the findings in A/J mice. This might be partially be explained due to the different H2 haplotypes (BALB/c: $H2^d$; A/J: $H2^k$ [18]).

Second, the general mechanisms of trans-inhibition of the opposite T_h response is disturbed in autoimmune diseases and other subsets of $CD4^+$ cells, namely T_h17 and especially T_{regs} are regulated differently in autoimmune myocarditis. The classical T_h2 cytokine IL-10 or the T_h1 primary cytokine Interferon γ have an inhibitory effect that prevent the development of myocarditis and show overlapping expression as well.

Pro-inflammatory cytokines like IL-4 and IL-1 have been shown to play a major role in expansion and differentiation of auto-reactive $CD4^+$ T-cells in presence of professional antigen-presenting cells [19], most importantly dendritic cells. IL-1β expression additionally correlates with fibrotic lesions that leads to dilated cardiomyopathy and an increased heart weight in the chronic phase [20].

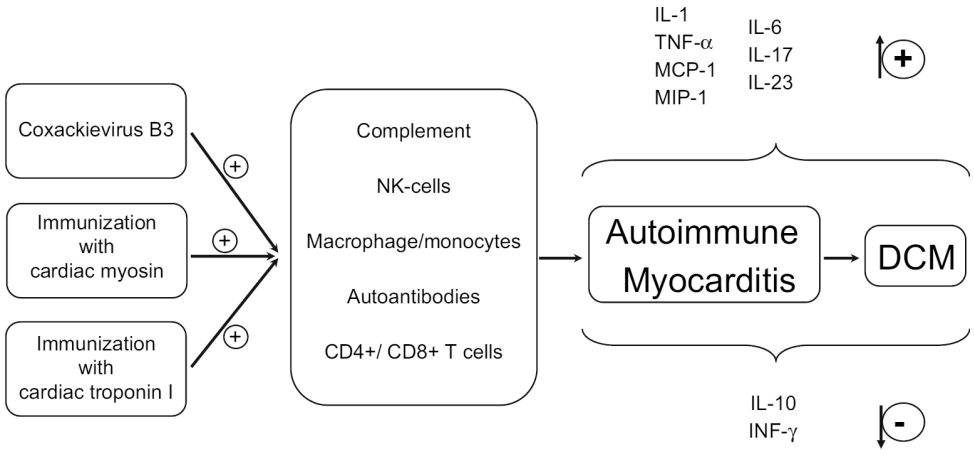

Figure 2.3: Development of Myocarditis. Adapted from Leuschner et al. [21]

Dendritic cells also express IL-12 and most importantly its closest relative IL-23. Both play a crucial role in activation and differentiation of $CD4^+$ T_h17 T-cells, an important subset involved in pathogenesis of myocarditis [22]. IL-23 knockout animals appear to be resistant against the induction of myocarditis and in those animals, transplantation of α-myosin specific $CD4^+$ T_h17 cells are sufficient to induce autoimmune myocarditis [23]. The effector function of $CD4^+$ T_h17 cells includes the

broad induction of many pro-inflammatory chemo- and cytokines and prostaglandins that increase the cellular influx of monocytes and neutrophils into the myocardium significantly.
The effect of T_h17 activation in this scenario is the initiation of a delayed-type immune reaction that is not terminated despite pathogen clearance.

Chronic phase with dilated cardiomyopathy. Ongoing inflammation in the myocardium can lead to severe tissue damage. Myocytes are replaced with connective tissue. On the one hand this leads to a decrease in myocardial elasticity and thus to impaired ventricular filling during diastole. On the other hand, loss of myocytes and thus a reduction of contractile elements leads to systolic dysfunction. Together, systolic and diastolic dysfunction lead to left ventricular filling at increased pressures, dilatation of the left ventricle with increased wall tension. Increased wall tension is counterbalanced by myocyte hypertrophy which worsens diastolic function. Thus, a vicious cycle is started which results in further dilatation and the development of dilated cardiomyopathy. In the clinical field, dilated cardiomyopathy is defined as a left ventricular volume above the 99th percentile of values encountered in a normal population, whereas a reduction in systolic function is generally defined as a reduction of the left ventricular ejection fraction below 45%. Dilated cardiomyopathy with reduced ejection fraction leads to clinical signs of heart failure (dyspnea, impaired exercise tolerance) and can result in the necessity for heart transplant. Due to arrhythmias, dilated cardiomyopathy can result in sudden cardiac death.

2.1.2 Diagnosing Myocarditis.

The clinical presentation of myocarditis is highly variable, and symptoms can even be absent. If present, symptoms can be non-specific (eg. fatigue, fever, dyspnea, chest pain). Routine cardiac tests either lack sensitivity (e.g. ECG) or specificity (e.g. troponins) for diagnosing myocarditis. The endomyocardial biopsy (EMB) is considered the gold standard to confirm the diagnosis of a suspected myocarditis [24]. However, EMB is invasive and suffers from low sensitivity and a high inter-observer variability in interpretation [25].
Thus, there is a need for non-invasive imaging methods for the diagnosis and detailed characterization of myocarditis. Echocardiography, radionuclide imaging and

cardiac magnetic resonance (CMR) imaging have all been used for the detection of myocarditis in clinical and pre-clinical studies.
Echocardiographic features of myocarditis include left ventricular dilatation, segmental wall motion abnormalities, increased left ventricular sphericity and transient increases in left ventricular wall thickness [26–28] but unfortunately are limited in diagnostic accuracy.
For nuclear imaging, Indium-111 radiolabeled anti-myosin antibodies have been used for the detection of myocardial necrosis in murine models of myocarditis and in clinical studies [29, 30]. CMR imaging allows detection of myocardial edema or irreversible tissue damage inflicted by the inflammatory infiltrate [31, 32] but sensitivity is variable and may be reduced in the absence of tissue necrosis [33].
Recently, fluorine-19 CMR has been used for detecting the inflammatory infiltrate in murine autoimmune myocarditis [34].
Thus, with the exception of fluorine-19 CMR, a common weakness of the aforementioned techniques is that they detect tissue injury (edema, necrosis), which can also be due to, for example, myocardial ischemia rather than the inflammatory infiltrate.
Animal models of both virus-induced and autoimmune myocarditis suggest that heart-specific auto-aggressive inflammatory responses are important in the development of chronic cardiomyopathy after acute viral infection, and that $CD4^+$ lymphocytes are instrumental in driving these processes [7, 13, 35].

2.1.3 Ultrasound molecular imaging in myocardial tissue

In the last years, microbubble ultrasound contrast agents have been modified for the purpose of molecular imaging. Either modifications in the shell properties or the conjugation of specific ligands to the microbubble shell surface have been successfully used to promote adhesion of microbubbles to disease-specific events on the endothelial surface of blood vessels.
The feasibility of this strategy for molecular imaging in the myocardium has been proven *in vivo* with targeted microbubbles against P-Selectin. In the ischemic myocardium, the endothelial cells react very quickly to the disturbed blood supply and increase in cellular stress (e.g. reduction of pH, oxidative stress). One result of the induced endothelial dysfunction is the rapid exposure of leukocyte-specific adhesion

molecules and chemokines that are stored in Weibel-Palade bodies, predominantly P-Selectin and IL-8. The increase of P-Selectin on the endothelial surface is facilitated within minutes and can prevail on elevated levels even after resolving of ischemia, a phenomenon called ischemic memory of the endothelium. Microbubbles targeted to P-Selectin either using a monoclonal antibody or the P-Selectin ligand sialyl Lewis^x were successfully used to identify ischemic myocardium [36, 37].

2.1.4 Aim of the study.

In this study, we therefore hypothesized that contrast enhanced ultrasound (CEU) molecular imaging can be used to detect (1) the inflammatory cell recruitment and endothelial inflammatory activation, and (2) the recruitment of $CD4^+$ lymphocytes in a murine model of myocarditis.

2.2 Material & Methods

2.2.1 Study design and animal model

All experiments were performed in accordance with Swiss Federal Legislation and were approved by the Animal Care Committee of the Canton of Basel. A total of 48 female BALB/c mice were used for this study.

Imaging of the acute phase in Myocarditis. In 44 mice, experimental autoimmune myocarditis (EAM) was induced by intra-peritoneal injection of 400 ng Pertussis toxin (List Biological Laboratories, Campbell CA) followed one hour later by subcutaneous injection of 120 µg of αMyHC peptide (α myosin heavy chain, Ac-RSLKLMATLFSTYASADR-OH, GeneCust, Dudelange, Luxemburg) emulsified 1:1 v/v with complete Freud's adjutant (CFA, Sigma Aldrich, Buchs, Switzerland) on day 0. On day 7, the animals were re-challenged with an αMyHC peptide injection. 4 animals injected with saline/CFA served as controls. The immunization with this particular αMyHC peptide results in development of EAM in about 60% of injected animals with an inflammatory infiltrate that peaks around day 21.

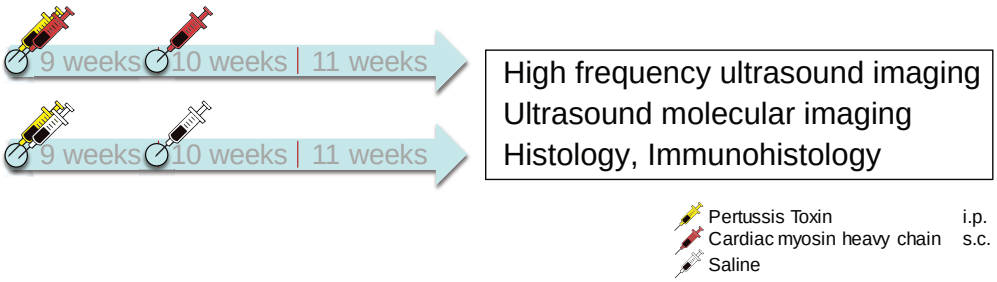

Figure 2.4: Study design. Animals were challenged with 2 injections containing cardiac α-myosin peptide and analyzed 3 weeks after induction of experimental autoimmune myocarditis. Control animals, that did not receive α-myosin peptide injections were analyzed as well. The animals were sacrificed after the analysis on day 21 and tissue was collected for histology.

Assessments at day 21 included:

Day 21 imaging acute phase

- high frequency ultrasound imaging including strain imaging,
- ultrasound molecular imaging targeting leukocytes, P-Selectin and $CD4^+$ lymphocytes as well as

- measurement of myocardial perfusion
- histology and immunohistology.

Histology of the hearts at the mid-ventricular level was performed for assessment of myocarditis severity and immunohistology was used to quantify $CD4^+$ lymphocytes in the tissue.

2.2.2 Microbubble Preparation

Perfluorocarbon-filled, lipid-shelled microbubbles were prepared by sonification of a gas-saturated aqueous suspension of distearoyl-phosphatidylcholine (2 mg/ml; Avanti Polar Lipids, Alabaster AL, USA) and polyoxyethylene-(40)-stearate (1 mg/ml; Sigma-Aldrich, Buchs). These non-targeted microbubbles were used for the assessment of myocardial perfusion. Microbubbles for targeting of leukocytes (MB_{Lc}) were prepared by adding distearoyl-phosphatidylserine (0.3 mg/ml; Avanti Polar Lipids) to the aqueous suspension before sonification [38].

For targeting of P-Selectin and CD4, distearoyl-phosphatidylethanolamine- PEG(3400)-biotin (0.14 mg/ml; Creative PEG Works, Chapel Hill, NC, USA) was added to the lipid suspension. Microbubbles targeted to P-Selectin (MB_{PSel}) and to CD4 (MB_{CD4}) were then prepared by conjugation of biotinylated anti-P-Selectin antibody (RB40.34, BD Bioscience) or anti-CD4 antibody (H129.19, BD Bioscience) to the microbubble surface using biotin-streptavidin-biotin linking as previously described [39]. Control microbubbles (MB_{Iso}) bearing a non-specific isotype control antibody (R3-34, BD Bioscience) were also prepared. Microbubble concentration and size were measured by electro-zone sensing (Multisizer III, Beckman-Coulter). Microbubble mean size was not statistically different for the three microbubble preparations (2.7 $\pm$0.2 µm for MB_{Iso}, 2.5 $\pm$0.2 µm for MB_{Lc}, 2.7 $\pm$0.2 µm for MB_{PSel}, 2.7$\pm$0.2 µm for MB_{CD4}; p=n.s.).

2.2.3 In vitro assessment of microbubble-CD4 interaction

Flow chamber experiments were used to assess the specific attachment of MBCD4 to CD4 protein under flow conditions. $CD4^+$ protein was adsorbed to culture dishes (35mm, Corning, Corning NY) at a concentration of 5 ng/µl by overnight incubation at 4°C. The dishes were then washed with PBS containing 0.05% Tween 20 and blocked with 1% albumin in PBS/0.05% Tween 20 for 1 hour at room temperature.

The culture plates were mounted on an inverted parallel plate flow chamber (Glycotech, Gaithersburg, MD, USA) with a gasket thickness of 0.127 mm and a channel width of 2.5mm. The flow chamber was placed in an inverted position on a microscope (Olympus BX51W). A suspension of either MB_{Ctr} or MB_{CD4} at a concentration of $3 \times 10^6 ml^{-1}$ was drawn through the flow chamber at a shear rate of 2 dynes/cm^2. After five minutes of continuous flow, the number of attached microbubbles was counted in 40 randomly selected, non-overlapping optical fields (20× magnification, total area 2.94 mm^2). Experiments were carried out in triplicate.

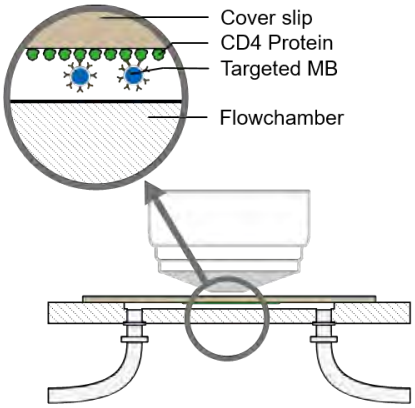

Figure 2.5: Schematic of the used parallel plate flow chamber coated with CD4 protein.

A cell-based adhesion assay was used to determine whether MB_{CD4} specifically attach to lymphocytes expressing CD4. Single cell suspensions of murine spleen cells from 4 mice were generated using a cell strainer (40 µm, nylon, BD Falcon 352340). CD4$^+$ T cells were enriched in the cell suspension by depletion of magnetically labeled non-target cells using a cocktail of biotin-conjugated monoclonal antibodies and anti-biotin MicroBeads (CD4$^+$ T Cell Isolation Kit II, Miltenyi Biotec) according to the manufacturer's instructions. Both the separated non-target cells and the CD4$^+$ cells were resuspended at a concentration of 2×10^7 cells per 100 µl. Static preparations of either 1×10^6 CD4$^+$ leukocytes or CD4$^-$ leukocytes respectively were then incubated with 1×10^7 microbubbles (MB_{Ctr} or MB_{CD4}) at room temperature for 10 minutes followed by washing with PBS twice. Cells were counter stained with nuclei-specific Hoechst 33342 (ThermoFischer, Reinach). Microscopy at 20× magnification (Zeiss LSM 710) was used to assess microbubble attachment to the cells.

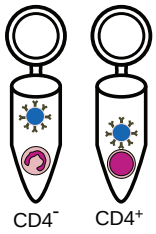

Figure 2.6: CD4$^-$ or CD4$^+$ cells incubated with MB_{CD4}

2.2.4 Animal instrumentation

On day 21 after immunization the mice were anesthetized with 5% isoflurane, which was subsequently reduced to 2% and adapted to stabilize the heart rate between 350 and 450 bpm. The animal core temperature was maintained at 37 °C at all times by the use of a temperature controlled heating stage. Chest and neck were depilated with a chemical hair remover and cleaned thoroughly. For microbubble injections, the right internal jugular vein was cannulated with a 0.97 mm polyethylene tubing (PE-50, BD Diagnostics).

The animals were then transferred onto a temperature-regulated imaging stage (Vevo Imaging Station).

2.2.5 2-dimentional and M-Mode Echocardiography

High frequency (40MHz, MS 550D transducer) ultrasound imaging (Vevo 2100, VisualSonics Inc., Toronto, Canada) was performed for assessment of cardiac structure and function.

M-Mode images of the left ventricle at the height of the papillary muscles were used to measure anterior and posterior wall thickness, left ventricular diameter both during systole and diastole (see Figure 2.7).

Left ventricular ejection fraction (EF) and left ventricular mass were derived from these measurements as described previously [40].

E-wave and A-wave velocities were measured using pulse-wave Doppler tracings from a modified apical 4-chamber view to assess flow across the mitral valve.

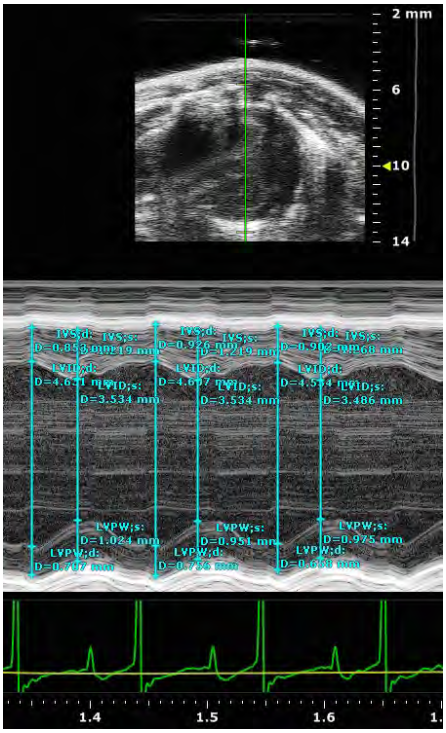

Figure 2.7: Assessment of wall thicknesses in M-Mode images. Differences of diastole and systole were averages of three measurements.

Strain imaging

Usually, left ventricular ejection fraction assesses systolic function accurately. However, the ejection fraction does depend as well on the ventricular contractility and pre- and after-load. Therefore, other measurements that assess contractile function, have been developed.
Strain imaging is a method in echocardiography to assess deformation of the contracting and relaxing myocardium over time. That is of importance, because in myocardial ischemia or infarction, parts of the myocardium will have reduced systolic function through transient or permanent impairment of their contractile capabilities. A passive area however can appear moving fully functionally in a B-mode exam through forces exerted by surrounding segments. Strain imaging is especially useful in these situations, because the whole myocardium in the imaging plane can be tracked for its deformation and nonfunctional areas can be identified.
Strain imaging can be performed either by tissue doppler or by speckle tracking echocardiography. Speckle tracking is based on interference patterns (speckles) within the myocardial tissue that can be tracked between at least two frames in B-mode images. These unique patterns are being tracked between frames and a global vector map of the myocardial tissue will be generated with information about velocities and directions for every point in the myocardium over time. In that way, the myocardial tissue deformation and movement can be assessed and quantified.

For strain measurements, parasternal long- and short-axis B-mode images were acquired at a frame rate of >200 frames per second. Longitudinal, radial and circumferential global peak strain values were derived from the B-mode images using a speckle tracking algorithm (VevoStrain, VisualSonics) [41].

Briefly, cine-loops with two cardiac cycles not distorted by respiratory movements were selected and the endocardial and epicardial borders were traced on end-diastolic frames (see Figure 2.8). After automated tracing, manual adjustments were made as necessary for good tracking throughout the cardiac cycles. The strain measurements were then averaged over the two cardiac cycles without the use of temporal smoothing filters.

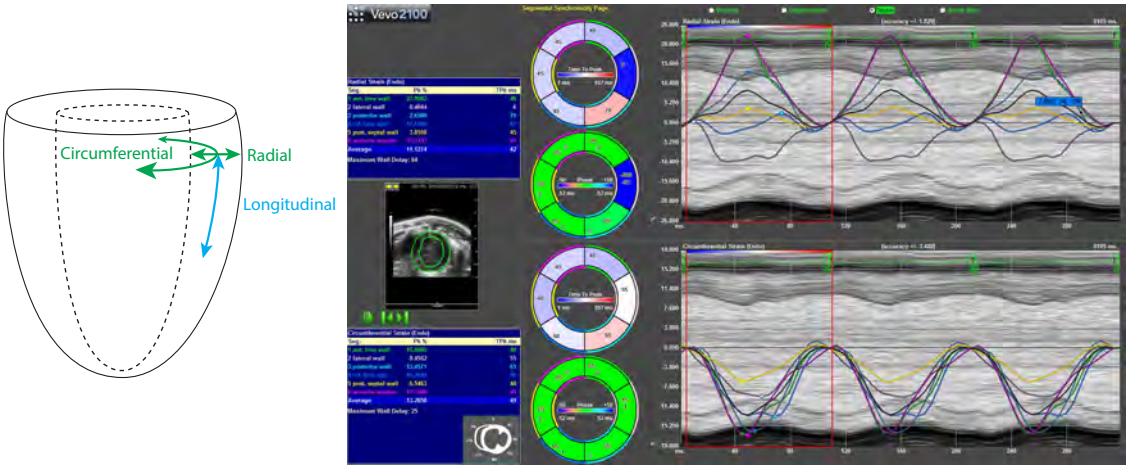

(a) **(b)**

Figure 2.8: (a) Strain in three dimensions. Measurements were performed in the short axis imaging plane (radial & circumferential strain) and in the long axis imaging plane (longitudinal strain). **(b)** Exemplary strain measurement of the endocardium in the short axis plane. After tracing the region of interest, motion vectors are calculated based on specle-noise movements in the tissue. An average of all 6 segments is then calculated for the whole endocard in the particular imaging plane.

2.2.6 Contrast Enhanced Ultrasound Imaging

Contrast ultrasound imaging (Sequoia Acuson C512; Siemens Medical Systems USA Inc., Mountain View, CA) was performed with a high-frequency linear-array probe (15L8) held in place by a railed gantry system. The left ventricle was imaged in short axis at the papillary muscle level from a left parasternal window. ECG-gated triggering was used to acquire end-systolic frames. For the detection of the contrast agent, power modulation and pulse inversion (Contrast Pulse Sequence) imaging at a centerline frequency of 7 MHz and a dynamic range of 50 dB was used.

Molecular CEU imaging.

The gain settings were adjusted to levels just below visible noise speckle and held constant. MB_{Iso}, MB_{Lc}, MB_{PSel}, or MB_{CD4} (3×10^6 microbubbles per injection) were injected intravenously in random order. Ultrasound imaging was paused from the time of injection until eight minutes later when imaging was resumed at a mechanical index of 0.87. The first acquired image frame was used to derive the total amount of microbubbles present within the left ventricular myocardium.

The microbubbles in the ultrasound beam were then destroyed with several (>10) high intensity image frames with a mechanical index of 1.9. Several image frames at a long pulsing interval (every 9 heartbeats) were subsequently acquired to measure signal attributable to freely circulating microbubbles. After log-linear conversion using known dynamic range lookup tables, frames representing freely circulating microbubbles were digitally subtracted from the first image to derive signal from attached microbubbles alone. Contrast intensity was measured from a region of interest encompassing the whole left ventricular myocardium. The selection of the region of interest was guided by fundamental frequency anatomic images of the left ventricle acquired at 14 MHz at the end of each individual imaging sequence. In 7 additional animals with myocarditis, imaging was performed 10 minutes after blocking of CD4 by intravenous injection of anti-mouse CD4 mAb (H129.19, BD Bioscience, 5μg).

Myocardial perfusion After CEU molecular imaging, microvascular perfusion was assessed using constant infusions of non-targeted microbubbles at an infusion rate of 3×10^6 microbubbles per minute. A high energy destruction impulse spanning 5 frames with a mechanical index of 1.9 was performed to destroy all microbubbles in the image plane. End-systolic short-axis image frames of the left ventricle were acquired over several heartbeats (>10) at a low mechanical index of 0.2.
On the resulting destruction-replenishment sequences, the average signal intensity of the myocardium was fitted to the mono-exponential function $f(t) = A(1 - e^{-\beta t})$, where $f(t)$ is the signal intensity at a given time point, β is the rate of rise of the curve, and A is the plateau intensity. Myocardial blood flow (MBF) was estimated by the product of A×β [42].

2.2.7 Histology and immunohistology

Two 5μm thin tissue slices at the height of papillary muscles where the contrast-enhanced ultrasound imaging was performed were processed for histological analysis. For the assessment of myocarditis severity, Hematoxylin and Eosin stained short axis cross-sections of the hearts were analyzed by an independent pathologist blinded for all other experimental data. Myocarditis was assessed following an accepted guidelines [35] on a scale ranging from 0 to 4 by a pathologist blinded to animal

treatment.

score 0 representing no inflammatory infiltrate
score 1 small foci of leukocytes between cells
score 2 larger foci of >100 leukocytes
score 3 >10% of the cross section involved
score 4 >30% of the cross section involved

For immunohistochemistry, snap frozen heart sections were stained with antibodies for CD4 (MCA4635T, AbD Serotec).A fluorescent secondary antibody (A-11006 Alexa 488, Invitrogen) was used to visualize CD4, and the cells per mm^2 of tissue staining positive for CD4 were quantified. P-Selectin was visualized using a biotinylated goat anti-rabbit secondary antibody (biotinylated goat anti-rabbit IgG, Vector laboratories) and staining with a peroxidase kit (ABC Vectastain Elite, Vector Laboratories).

2.2.8 Statistical Analysis

The data was analyzed on GraphPad Prism (version 6.07).
Experimental data is expressed as mean ±SD unless stated otherwise. Echocardiographic *in vivo* data is presented as median (25th - 75th percentile) and non-parametric statistical tests were used. Analysis of more than two unpaired, non-parametric sets (e.g. attachment of microbubbles to $CD4^+$ versus $CD4^-$ cells vs. negative control or microbubble signals within and between animal groups) were compared using a Kruskal-Wallis ANOVA with Dunn's post hoc test. Correlations between 2 parameters (e.g. microbubble signal vs. $CD4^+$ cell number in tissue) were assessed using Spearman correlation.
A two-sided p value <0.05 was considered as statistically significant.

2.3 Results Imaging of the acute phase

2.3.1 Scoring of Myocarditis

Animals developed experimental autoimmune myocarditis that was scored positively by the pathologist in 52% of all cases. Animals that showed no myocarditis, were **scored 0** in 48% of all cases.

The detailed percentages for animals with detected myocarditis was 13% for **score 1**, 22% for **score 2**, 6% for **score 3** and 11% for **score 4**. Due to the small number of animals per group, mice with severity degree 3 and 4 were grouped as "severe myocarditis", severity degrees 1 and 2 as "moderate myocarditis, while injected mice that did not develop myocarditis were grouped with sham-injected mice as "no myocarditis".

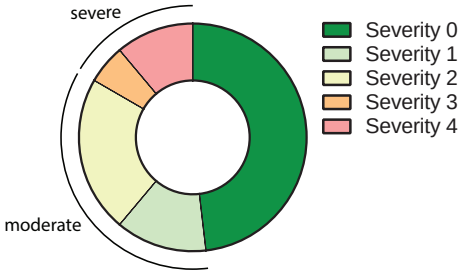

Figure 2.9: Induction efficacy.

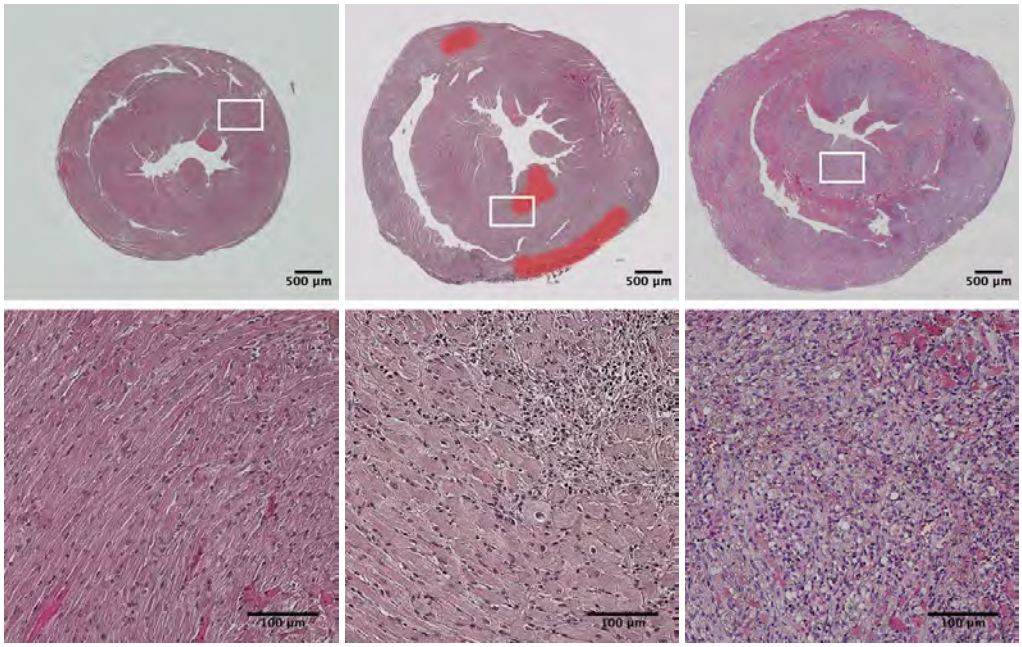

(a) **(b)** **(c)**

Figure 2.10: Exemplary H&E stainings for (a) no myocarditis (b) moderate myocarditis and (c) severe myocarditis. Red markings shows the area of intense leukocyte infiltration in the example for moderate myocarditis.

2.3.2 In vitro assessment of microbubble CD4 interaction

Flow chamber and *in vitro* cell-based assays were used to characterize MB_{CD4} interactions with CD4.

In cell-based assays, MB_{Ctr} showed no attachment to either $CD4^-$ (0.11 ±0.06) or $CD4^+$ leukocytes (0.06 ±0.05), nor did MB_{CD4} to $CD4^-$ cells (0.06 ±0.04). In comparison, MB_{CD4} attachment to $CD4^+$ cells was significantly higher ($p<0.001$) with an average of 0.55 ±0.06 microbubbles per cell (see Figure 2.11).

Under flow conditions in a parallel flow chamber, attachment of MB_{CD4} (3.8 ±3.2) was significantly greater ($p<0.001$) than MB_{Ctr} (0.8 ±1.0) (see Figure 2.12).

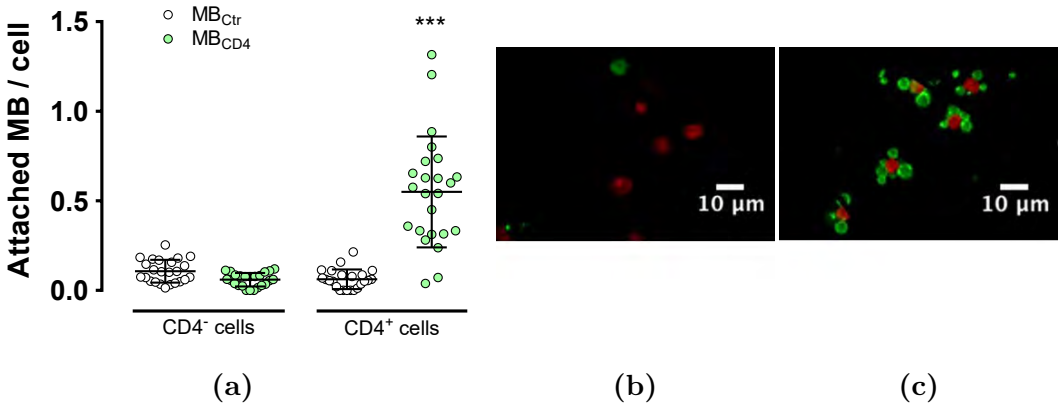

Figure 2.11: (a) CD4-targeted Microbubble adhesion to differential CD4 expressing cells. Exemplary microscopy images of MB_{CD4} incubated with $CD4^-$ (b) or $CD4^+$ cells (c).

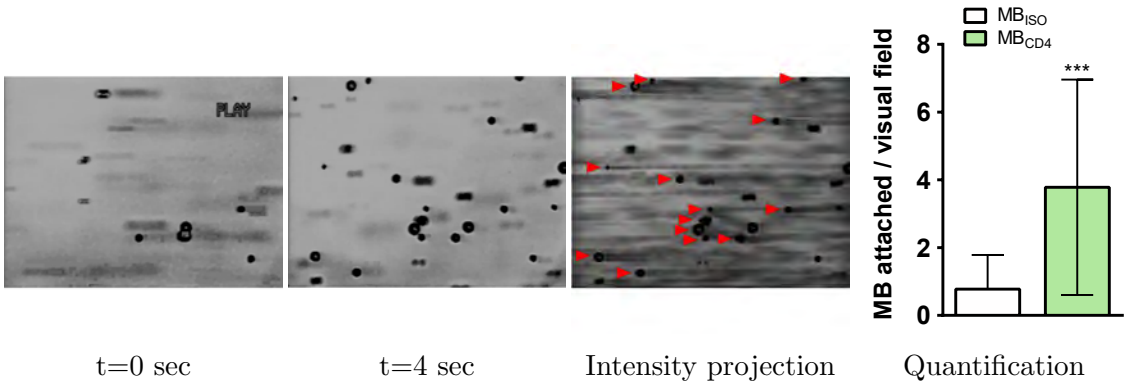

Figure 2.12: Examples of CD4-targeted microbubbles adhering to a CD4-coated flow chamber. First (a) and last frame (b) of a 4 second video sequence are shown. A maximum intensity projection of 120 acquired frames over a 4 second video illustrates the slowing and eventually firm adhesion of individual microbubbles (red arrowheads). Quantification of adhered microbubbles was done on 120 different field of views per condition.

2.3.3 Baseline characteristics and echocardiographic parameters

Mice with severe myocarditis were significantly lighter than both mice with no or moderate myocarditis (see Table 2.2).

Both the heart weight (determined post-mortem) as well as the left ventricular mass (determined by echocardiography) were higher in mice with severe myocarditis compared to the moderate or no myocarditis groups.

E-wave velocity was lower in mice with severe myocarditis compared to the other groups, while A-wave and the ratio E/A was not.

Table 2.2: Physiological and echocardiographic measures. Values are presented as median (25th - 75th percentile). P-values were calculated in comparison to "no myocarditis". * p <0.05; ** p <0.01; *** p <0.001.

	No Myocarditis (n=20)	Moderate Myocarditis (n=14)	Severe Myocarditis (n=7)
Body weight (g)	22.5 (18.6 – 24.8)	20.0 (19.4 - 22.7)	**15.5 (14.9 - 16.4)****
Heart rate (bpm)	388 (349 – 490)	413 (392 - 473)	403 (351 - 461)
Heart weight (mg)	112 (105 – 126)	119 (113 - 132)	**171 (147 - 207)*****
LV mass (mg)	76 (65 – 90)	88 (72 - 96)	**117 (82 - 137)****
LV AW_d (mm)	0.9 (0.8 - 1.0)	1.0 (0.8 - 1.1)	**1.4 (0.9 - 1.7)***
LV AW_s (mm)	1.3 (1.2 - 1.7)	1.5 (1.2 - 1.6)	1.8 (1.3 - 2.0)
LV PW_d (mm)	0.8 (0.7 - 0.9)	0.7 (0.7 - 1.0)	1.0 (0.8 - 1.1)
LV PW_s (mm)	1.2 (1.0 - 1.3)	1.1 (1.0 - 1.3)	1.1 (1.0 - 1.3)
LV ID_d (mm)	3.5 (3.2 - 3.7)	3.4 (3.3 - 3.7)	3.0 (2.5 - 3.5)
LV ID_s (mm)	2.1 (1.5 - 2.5)	2.0 (1.9 - 2.3)	1.7 (1.6 - 2.9)
LV Vol d (µl)	52 (40 – 57)	46 (44 - 57)	38 (24 - 52)
LV Vol s (µl)	15 (7 – 22)	13 (10 - 18)	9 (7 - 27)
EF (%)	73 (61 – 83)	70 (69 - 77)	69 (42 - 76)
β (s^{-1})	0.8 (0.5 – 1.2)	0.6 (0.4 - 1.0)	0.7 (0.2 - 0.8)
A*β	10 (2 – 29)	18 (8 - 31)	26 (6 – 49)
E-wave (mm s^{-1})	613 (563 – 734)	695 (567 - 802)	**527 (405 - 561)***
A-wave (mm s^{-1})	415 (371 – 454)	400 (346 - 531)	354 (154 - 428)
E/A	1.5 (1.3 – 1.7)	1.7 (1.3 - 1.8)	1.5 (1.0 - 2.0)

LV $AW_{d/s}$ left ventricular anterior wall during diastole/systole; **LV $PW_{d/s}$** left ventricular posterior wall during diastole respectively systole; **LV $ID_{d/s}$** left ventricular internal diameter during diastole respectively systole; **LV $Vol_{d/s}$** Left ventricular volume during diastole respectively systole; **EF** ejection fraction; β Microbubble replenishment rate; **A*β** Myocardial blood flow estimate **E-wave/A-wave velocity** early/atrial filling velocity; **E/A** early/atrial filling velocity ratio.

Last, the anterior wall thickness during diastole in the severe myocarditis group was significantly increased compared to no myocarditis. For all other echocardiographic parameters there were no significant differences between the groups.
Of note, A*β as an estimate of myocardial blood flow was not different between groups, albeit with large differences between individual animals.

Left ventricular strain parameters

Speckle tracking based strain measurements have been reported to be more sensitive for the detection of global changes in left ventricular function when compared to conventional echocardiographic measures listed above [41]. Global peak strain and peak strain rate were assessed on left ventricular long-axis and short axis images.

In mice with severe myocarditis, radial and circumferential strain showed a trend towards lower values while longitudinal strain was significantly decreased compared to animals without myocarditis (p=0.009) or moderate myocarditis (p=0.005). However, strain rates did not differ between animals with severe and moderate myocarditis and both strain and strain rate values were identical between mice with moderate and mice with no myocarditis (see Figure 2.13).

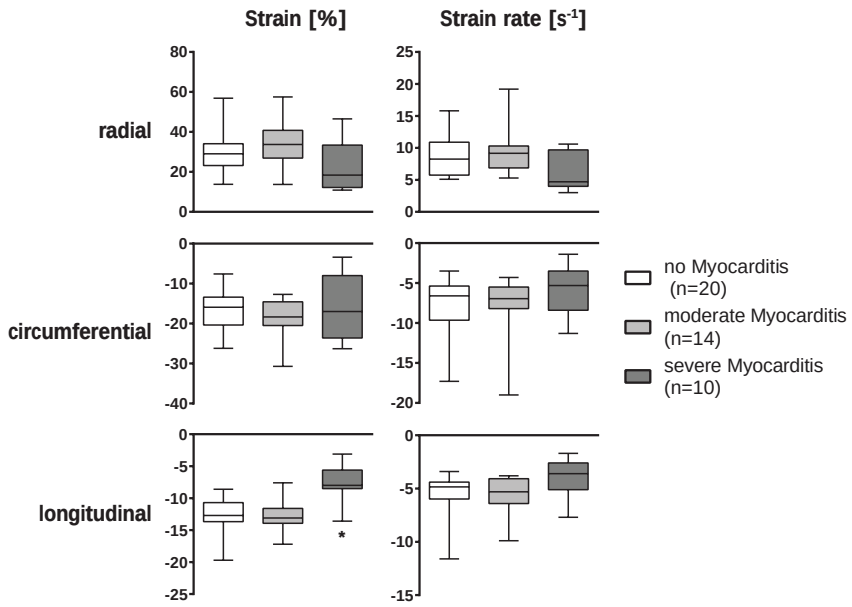

Figure 2.13: Strain imaging data according to myocarditis severity. Data is presented as 25th to 75th percentile boxplots with median and total range of values of video intensities. P-value: * p=0.009 compared to no myocarditis.

2.3.4 Ultrasound molecular imaging

Representative examples of color-coded intensity images for an animal without and for one with severe myocarditis respectively are shown in figure 2.14.
The selected animal with severe myocarditis showed visibly increased signals for the epitope-specific MB_{CD4}, MB_{PSel} and MB_{LC} as well as moderate increase in control microbubble signal.

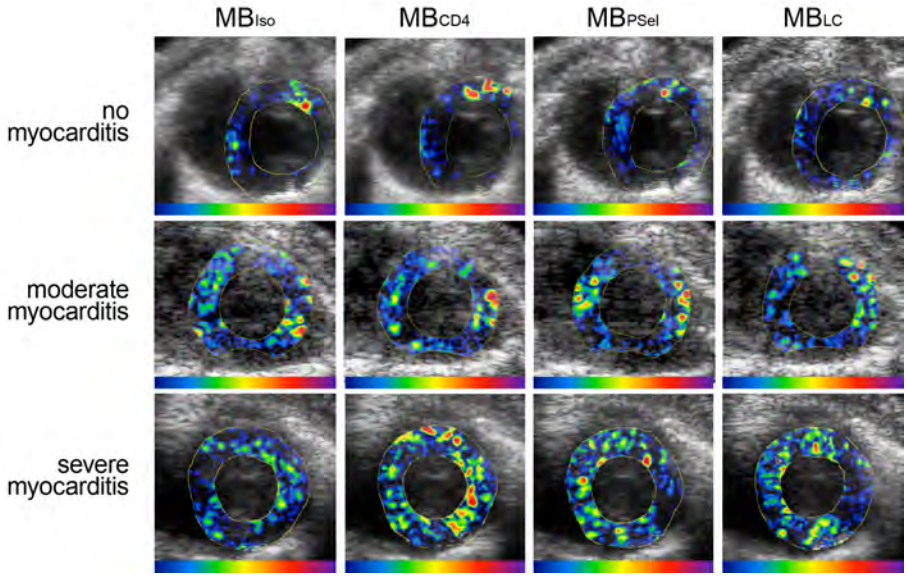

Figure 2.14: Examples of color-coded contrast-enhanced ultrasound (CEU) molecular images in an animal with no, moderate or severe myocarditis, respectively for microbubbles bearing isotype control antibody (MB_{Iso}), MB bearing antibody targeting lymphocyte CD4 (MB_{CD4}) or endothelial P-Selectin (MB_{PSel}) and MB with a negative electric charge for targeting of leukocyte (MB_{LC})

Figure 2.15 shows the data for ultrasound molecular imaging in all three groups of mice.
Signal enhancement was similarly low for all microbubbles in mice without myocarditis. In comparison, in mice with myocarditis the signals for MB_{CD4}, MB_{PSel} and MB_{Lc} were all significantly higher than signal from MB_{Iso}. Importantly, this was not just the case in severe but also in moderate myocarditis.
In mice with severe myocarditis, an increase in signal from MB_{Iso} could be observed, which was, however, not significant when compared to the corresponding signals in the two other groups ($p=0.99$ or $p=0.15$ respectively).
While the absolute signal intensities for MB_{CD4}, MB_{PSel} and MB_{Lc} increased in se-

vere myocarditis compared to mice with moderate myocarditis, the ratios for the targeted versus the control microbubbles remained constant at a two to three-fold increase due to non-significantly elevated signal from internal controls (MB_{Iso}).

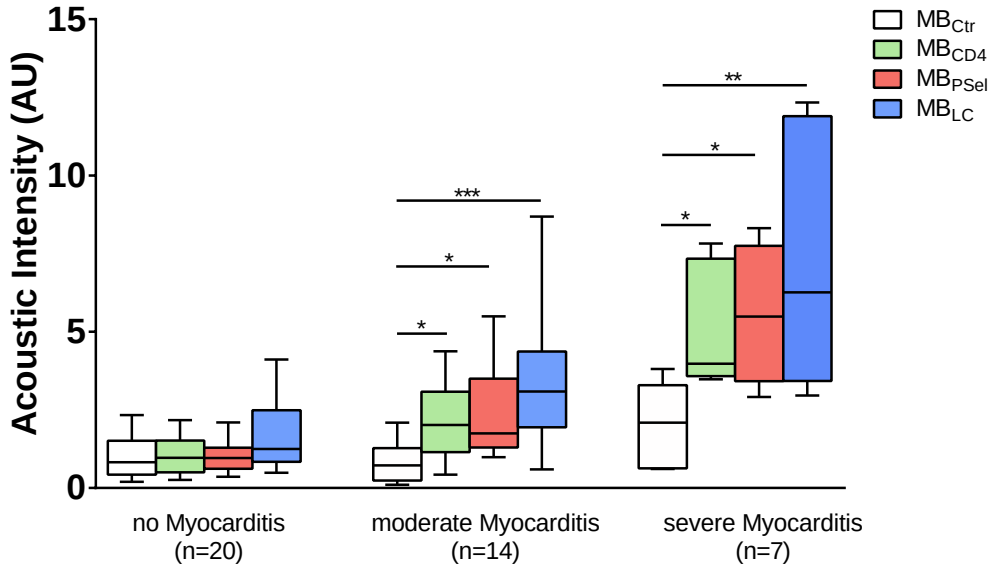

Figure 2.15: Signal enhancement from targeted microbubbles (MB_{CD4}, MB_{PSel}, MB_{LC}) compared to isotype control microbubbles (MB_{Iso}). Data is presented as 25th to 75th percentile boxplots with median and total range of values of video intensity. P-values: * $p<0.05$, ** $p<0.01$, *** $p<0.001$

Signal for MB_{CD4} was abolished after blocking with anti-CD4 antibody as demonstrated in 7 additional animals (see Figure 2.16). The reduction was significant ($p=0.03$) when compared to signals for MB_{CD4} of animals without treatment with the blocking antibody prior to imaging.
Correlation analysis of $CD4^+$ leukocyte counts in myocardia sections with molecular imaging data showed a signal correlation, albeit modestly, with MB_{CD4}, MB_{PSel} and MB_{Lc} (Figure 2.17).

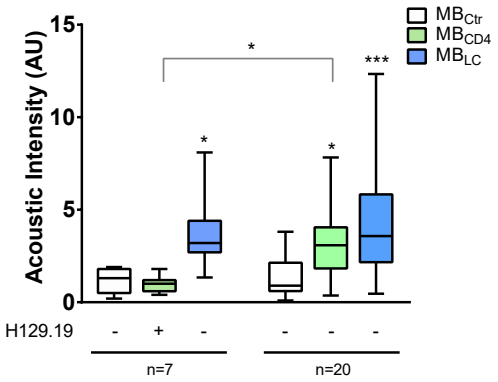

Figure 2.16: Blocking of CD4 (n=7) with a monoclonal antibody (H129.19) abolishes signal from MB_{CD4} compared to animals without the treatment (n=20).

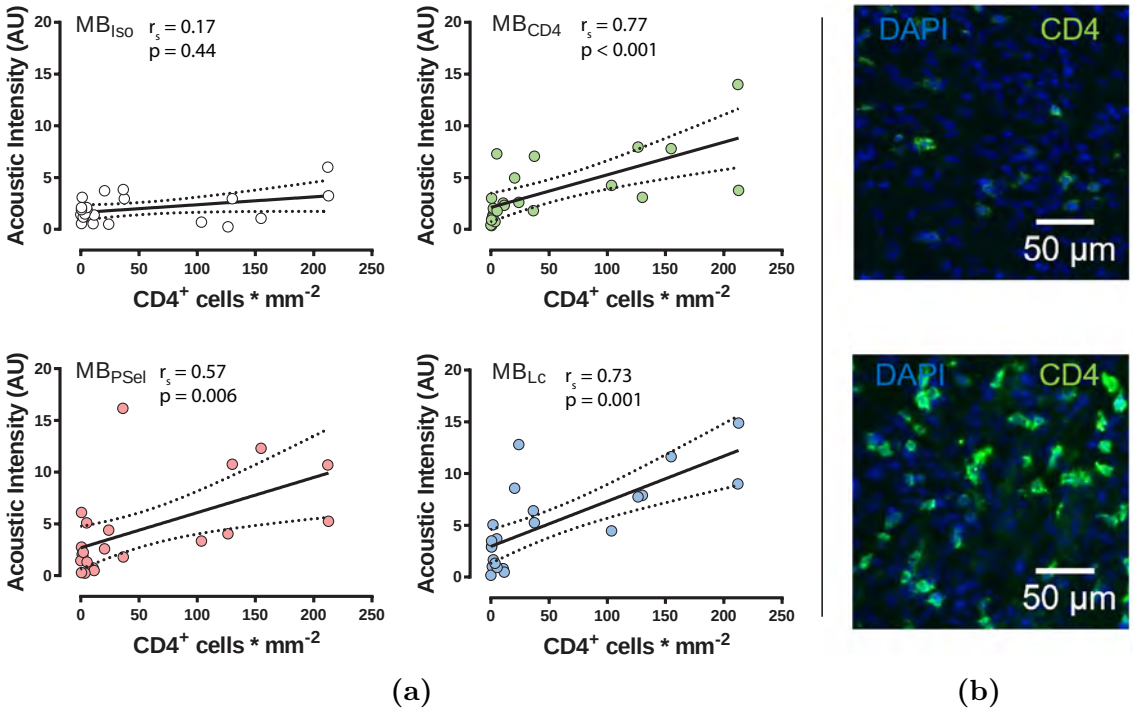

Figure 2.17: (a) Correlation of contrast-enhanced ultrasound molecular imaging data for MB_{Iso}, MB_{CD4}, MB_{PSel} and MB_{LC} in respect to number of $CD4^+$ cells per mm^2 in corresponding tissue sections. **(b)** Examples of low-level and extensive myocardial $CD4^+$ leukocyte infiltration.

To assess whether a measured parameter is a diagnostic test for myocarditis, receiver-operating-characteristic (ROC) curves have been calculated for selected parameters (see figure 2.18). The accuracy of a test is determined by how well the parameter can distinguish the animals into groups with or without myocarditis.
The area under the curve was determined and values > 0.80, $0.7 - 0.79$ or < 0.69 were considered as good, fair or poor tests, respectively.
A fair diagnostic parameter for myocarditis was found to be heart-weight (area=0.77) and bodyweight (area=0.73) while left ventricular mass (area=0.67) was ranked as poor. Most importantly, signals in molecular imaging from MB_{CD4}, MB_{PSel} and MB_{LC} showed a good ability to predict myocarditis (area> 0.8). The ROCs for MB_{Iso}, ejection fraction, wall thicknesses and strain measurements did not show a predictive value for acute myocarditis.

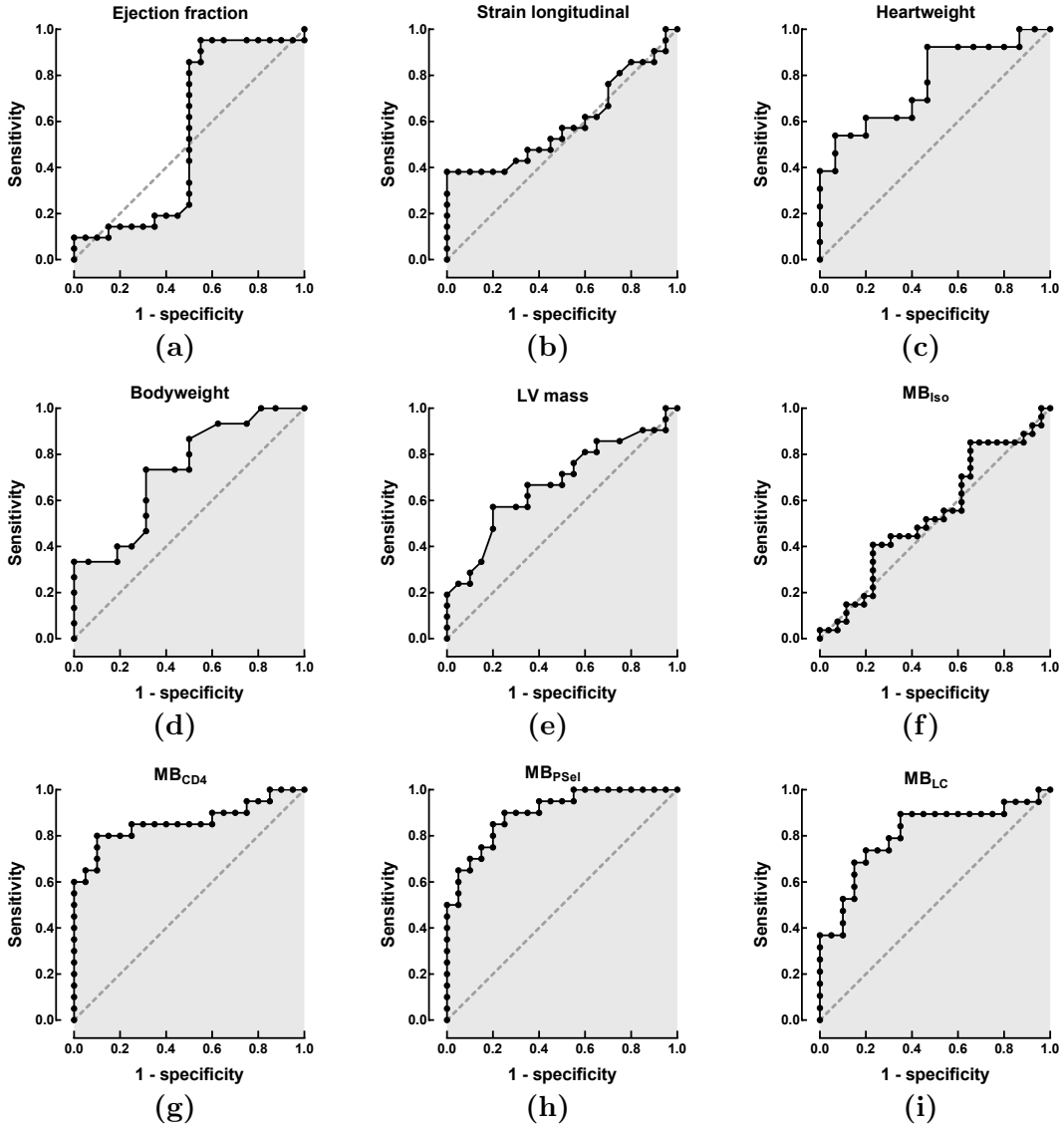

Figure 2.18: Receiver-operating-characteristic (ROC) curves in diagnosing myocarditis shown for selected parameters. Data presented is area under curve with respective p values (n=20 mice without myocarditis, n=21 mice with myocarditis).
(a) Ejection fraction (area=0.54, p=0.63); **(b)** Strain longitudinal (area=0.56, p=0.51); **(c)** Heartweight (area=0.77, p=0.02); **(d)** Bodyweight (area=0.73, p=0.03); **(e)** Left ventricular mass (area=0.67, p=0.05); **(f)** Signal for MB_{Iso} (area=0.54, p=0.62); **(g)** Signal for MB_{CD4} (area=0.86, p<0.001); **(h)** Signal for MB_{PSel} (area=0.90, p<0.001); **(i)** Signal for MB_{LC} (area=0.81, p<0.001)

2.4 Discussion

Myocarditis and the ensuing inflammatory autoimmune phenomena can lead to chronic dilated cardiomyopathy and heart failure. Currently available non-invasive imaging methods detect the functional or structural consequences of infection or inflammation such as tissue necrosis or edema and are limited in diagnostic accuracy. Therefore, the use of contrast enhanced ultrasound molecular imaging to detect the inflammatory process in myocarditis was investigated. The obtained results indicate that **(1)** CEU ultrasound molecular imaging detects myocardial inflammatory infiltration and endothelial cell activation independent of functional consequences in autoimmune myocarditis, and **(2)** CEU molecular imaging allows for the detection of $CD4^+$ lymphocytes which contribute to the pathogenesis of myocarditis and dilated cardiomyopathy.

CEU molecular imaging detects myocarditis independent of functional impairment.

Despite advances in non-invasive imaging, myocarditis continues to represent a challenging diagnosis. While conventional echocardiography can detect structural and functional alterations in fulminant myocarditis [43], it is limited in sensitivity and specificity in lower grade acute myocarditis, which has a higher likelihood of progression to dilated cardiomyopathy.

In this study, left ventricular mass and heart-weight was found to be increased while left ventricular function (E-wave velocity, longitudinal strain) tended to be decreased in the group with severe myocarditis. An increase in anterior wall thickness both in systole and diastole was observed and does fall in line with the increase in heart-mass in respect of the peaking inflammatory processes. However, despite the use of high-resolution ultrasound and highly sensitive speckle tracking analysis, there were no differences in left ventricular size and function between the group without myocarditis and the group with only moderate myocarditis.

Direct assessment of the inflammatory process - responsible not only for acute myocarditis, but also for the progression to dilated cardiomyopathy through autoimmune mechanisms - may improve the diagnostic performance of cardiac ultrasound.

This study shows that CEU molecular imaging with microbubbles targeted to leukocytes and P-Selectin yields increased signal not only in the group with severe myocarditis, but also in the group with moderate myocarditis, suggesting that the direct detection of the inflammatory infiltrate rather than its functional consequences results in better sensitivity in detecting myocarditis.

In addition to relatively non-specific targeting of activated leukocytes using negatively charged microbubbles [38], antibody-targeting of microbubbles toward the endothelial cell adhesion molecule P-Selectin was applied. P-Selectin is expressed on the surface of the vascular endothelium upon inflammatory stimulation. In myocarditis, P-Selectin plays an important role by mediating the recruitment of pathogenic T-cells into the myocardial tissue [44]. The obtained results are in line with earlier reports, which show that CEU molecular imaging can detect cardiac transplant rejection by targeting activated leukocytes or inter-cellular adhesion molecule-1 [45, 46]. However, while the inflammatory process in transplant rejection shares certain similarities with myocarditis, an important difference that complicate the diagnostic challenges is the low-grade and focal nature of the inflammatory infiltrate in moderate myocarditis. Also, the finding that CEU molecular signal for both leukocyte- and P-Selectin targeted microbubbles was much greater in severe compared to moderate myocarditis indicates that various degrees of disease activity can be discerned.

CEU molecular imaging assesses the infiltration with pathogenic $CD4^+$ lymphocytes

In animal models of both viral and autoimmune myocarditis, $CD4^+$ lymphocytes represent a relatively small subset of leukocytes infiltrating the myocardium [47]. However, development of myocarditis upon transfer of appropriately activated $CD4^+$ lymphocytes in host animals suggests a decisive role of $CD4^+$ lymphocytes in myocarditis [35]. In addition, the number of $CD4^+$ lymphocytes within tissue correlates with cardiac functional impairment in the chronic stage of experimental autoimmune myocarditis [48]. Therefore, a novel, $CD4^+$-targeted microbubble using was developed and validated. Flow chamber assays and in vitro experiments showed that this targeting ligand displayed on the microbubble surface mediates specific attachment

to $CD4^+$ lymphocytes, and that attachment occurs also under flow conditions.
In vivo, CEU molecular imaging showed increased signals both in moderate and in severe myocarditis, and the signal correlated with the numbers of $CD4^+$ lymphocytes present in tissue. While direct observation of microbubble-lymphocyte interactions in vivo was not possible, abolishment of signal by blocking of $CD4^+$ indicates selective targeting similar to in vitro observations.

Limitations of this study.

There are several limitations of this study that deserve attention. The used model of experimental autoimmune myocarditis was induced with peptide-based self-antigens rather than by virus-induction. However, EAM shares many patho-physiological features with virus-induced myocarditis, and has been used extensively to study the autoimmune processes caused by initial viral myocyte infection [49].
Regarding CEU molecular imaging, differences in myocardial perfusion between groups could potentially influence the results. While there was a high variability in myocardial perfusion in mice with severe myocarditis, we did not find significant differences between groups, and in particular perfusion was identical in mice without and mice with moderate myocarditis. In addition, the low signals for control microbubbles in both groups with myocarditis argue against an influence of myocardial flow on CEU molecular imaging results.
Last, the limited spatial resolution of CEU at 7MHz in the mouse model that was used precluded a regional assessment of disease activity, which would be desirable for example for the guidance of endomyocardial biopsies in patients.

2.5 Summary

In summary, the results of this study indicate that CEU molecular imaging can be used to detect the inflammatory process in myocarditis and discriminate the disease severity independent of cardiac function.
In addition, specific molecular imaging of a leukocyte subset that is driving the autoimmune process in myocarditis is possible.
As a consequence, CEU molecular imaging can potentially be useful in the diagnosis of myocarditis.

3 Contrast imaging for the prediction of long-term consequences of acute myocarditis

3.1 Introduction

The inflammatory processes in myocarditis have been described in chapter 2.1.1. The natural course of myocarditis is spontaneous recovery in 40-60% of biopsy-proven cases [50] without any impact on heart function. However, at least a fifth of patients diagnosed with myocarditis progress to dilated cardiomyopathy with myocardial remodeling that results in ventricular dysfunctions [51]. The long-term prognosis for patients developing reduced ejection fraction is unfavorable with mortality rates of more than 50 % after 4 years [52], and only a third of patients report partial or complete recovery [53] of left ventricular function. Clinically, dilated cardiomyopathy with reduced ejection fraction manifests with symptoms of heart failure (eg. dyspnea, decreased exercise tolerance). In addition, dilated cardiomyopathy with reduced ejection fraction represents arrhythmogenic substrate [54] and entails the risk for sudden cardiac death. While the numbers are not dramatically high, disease progression can be dramatic and myocarditis is responsible for 10% of heart transplantations worldwide [55].

The change in myocardial tissue composition is the driving force for ventricular dilatation and decrease of heart function. The main components in the myocardial extracellular matrix are fibrillar collagens of type I (>60%) and type III (10-40%) and to a lesser extend type V (<5%) and other elements (laminins, proteoglycans etc.) [56]. The collagen network in the myocardium can be divided into 3 separate components and their organization is important for the maintenance of myocardial

compliance: **(1)** the endomysial collagen surrounds individual myocytes and interconnects them by struts, **(2)** the perimysal collagen surrounds groups of myocytes and **(3)** the epimysial collagen surrounds entire muscle bundles in the myocardium. Upon cardiomyocyte damage, either by direct injury or by an uncontrolled host immune response, the myocytes damage will be cleared. The turnover rates of cardiomyocytes are very low at 0.5% to 1% of total cardiac cells per year [57] and the regenerative capacity of the myocardium is very limited. Resident cardio-fibroblasts will replace damaged myocytes with extracellular matrix, mainly collagen type I. In humans, the global collagen ratio of typI/typeIII increases in dilated cardiomyopathy from 0.6 to 1.3 [58]. Less collagen type III leads to a reduction of the elastic properties of the myocardium and impacts the diastolic function. In addition, a decrease in interchain cross-linking results in myocyte sliding and thus contributes to chamber dilatation [59].

Important players in the degradation of existing myocardium that is subsequently replaced with extracellular proteins are proteases. The proteases can originate from infecting viruses. However, the most important source of proteases are myocardial cells. Upon stimulation by pro-inflammatory cytokines, endothelial cells, fibroblasts and cardiomyocytes secrete a set of proteases (matrix metalloproteinases (MMPs), thrombin, elastase). In infarction models, cytokines like IL-1, IL-6 and TNF-α induce proteases (e.g. MMP-2, thrombin) [60]. Higher MMP activity increases trans-endothelial migration of leukocytes (see figure 3.1). The invading neutrophils and macrophages secret a different set of proteases, including MMP8, MMP9 and MMP12 as well as elastase, cathepsin G that augment leukocyte recruitment and initiate a vicious cycle.

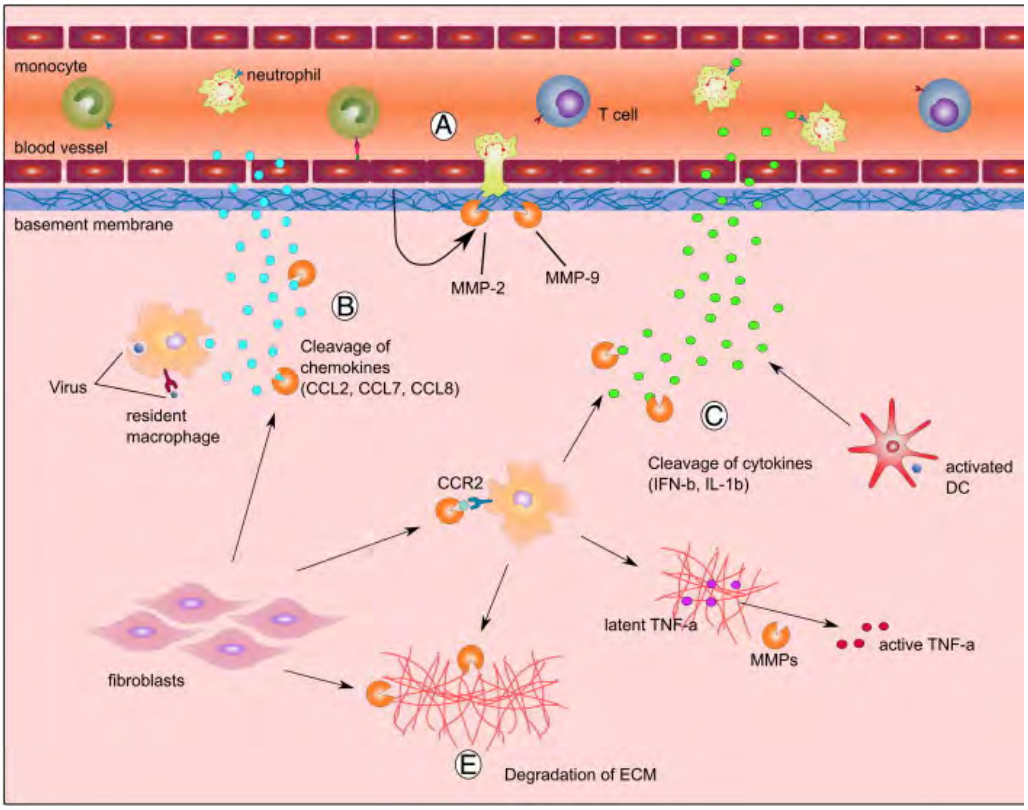

Figure 3.1: Proteases in Dilated cardiomyopathy. (A) MMPs are responsible for degrading the basement membrane and increase transendothelial migration of immune-cells. (B) Cardiac cells (macrophages, cardiomyocytes, dendritic cells, endothelial cells, fibroblasts) get activated and secrete chemokines. Activated MMPs cleave these chemokines, modulating their activity and gradients (activation or inactivation). (C) Secreted cytokines get processed by MMPs as well and change their activity, contributing to an exacerbation or resolution of the inflammation. (E) MMP up-regulation leads to cleavage of ECM components, myocardial slippage and a change in the normal ventricular structure and function. Adopted from Westermann et al. [61].
CCL, CC-chemokine ligand; CCR, CC-chemokine receptor; MMP, matrix metalloproteinase; IL, interleukin; IFN, interferon; TNF, tumor necrosis factor; DC, dendritic cell; ECM, extracellular matrix.

Beside the effect of vascular permeability and degradation of extracellular-components (predominantly collagens), the activated proteases can cleave specific chemokines and cytokines and thus modulate their properties. The proteolytic cleavage is a natural way to clear pro-inflammatory cytokines (e.g. CCL7 is cleaved by MMP2). However, IL-1β and IFN-β for example are degraded by MMP9, while latent TNF-α that is bound to ECM gets activated through cleavage and subsequent release by MMPs[62, 63], both processes that increase inflammation and drive the car-

diac remodeling. Another effect of increased protease activity is the activation of protease-activated receptors (PAR). PAR-1, 2 and 4 are expressed on endothelial cells, cardiomyocytes and cardiac fibroblasts [64] and are involved in sensing conditions of the extracellular matrix. PAR-1 is especially important in heart remodeling while PAR-2 is associated with the inflammatory processes. The receptors are individually activated by a different set of specific MMPs, thombin, elastase, and coagulation proteases.
Upon activation, PAR-1 trans-activates the epidermal growth-factor receptor and stimulates multiple signaling pathways (via ERK, p38, AKT) [65] that lead to increased proliferation of cardiac fibroblasts and an increase in cytokine expression. The expression of IFN-β and CXCL10 is upregulated as well [66]. Both increase NK cell recruitment and fuel the inflammatory processes in myocarditis. PAR-2 and -4 is expressed on myocardial cells, neutrophils, mast cells and other leukocytes and strongly increase chemotaxis [67] and the release of inflammatory mediators [68].
IL-1β expression correlates with fibrotic lesions and heart weight in the chronic phase of myocarditis [20]. IL-6 neutralization increases myocardial fibrosis in cardiac graft models [69], suggesting a pivotal role in the development of DCM. IL-17A deficient mice show reduced gene transcription of various MMPs and are protected from post-myocarditis remodeling [70]. Additionally IL-1, IL-6 and IL-17 induce MMP secretion in myocardial fibroblast and myocytes suggesting a pivotal role in matrix remodeling [71] that leads to the progression of DCM.

Together, the changes in the extracellular matrix and the decrease of myocytes numbers lead to dilated cardiomyopathy with cavity enlargement of left and/or right ventricle with an reduced ejection fraction. Defined thresholds of an ejection fraction $<45\%$ and left ventricular end-diastolic diameter $>112\%$ in humans [72] are considered diagnostically relevant.
The described changes that occur at the cellular level have a impact on the function of the myocardium. The heart action can be simplified as a periodic contraction during systole and relaxation during diastole with the goal of pumping blood into the body (see figure 3.2). During systole, the myocytes shorten and this force is sustained and distributed by the ECM and thus the cavity volume decreases. In this process Spiraling arrangement of muscle fibers in the myocardium contribute

to the augmentation of a 15-20% shortening of myofibers into an ejection fraction of around 60% [73]. During diastole, relaxation of the myocytes in combination with the elastic properties of the ECM allows the cavity to fill again.
Any changes in either the complex system of myocardial muscle-fibers or the composition of the ECM leads to reduced forces that can be generated against the volume-load of the heart, and lead to chamber dilatation and reduced systolic function.

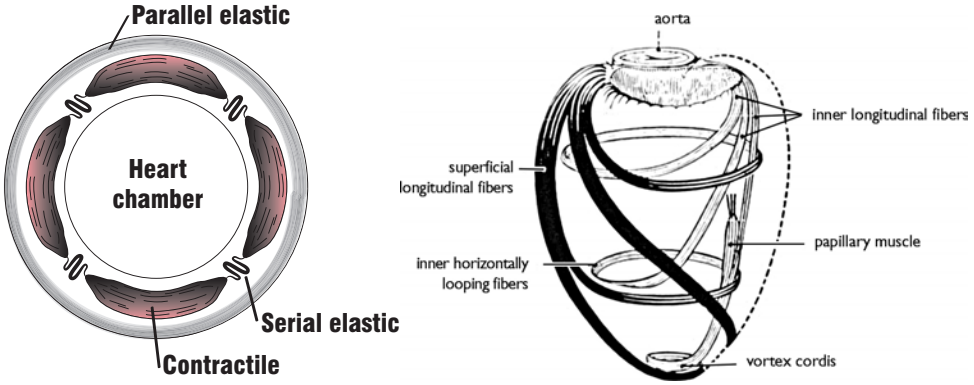

(a) (b)

Figure 3.2: (a) Simplified model of longitudinal heart forces, generated by contractile muscles and sustained by extracellular matrix network. After Fry et al. [74] **(b)** Schematic of spiraling heart fibers in the left ventricle. Adapted from "The Dynamic Heart and Circulation" [75]

Aims of the study

Clinically used imaging techniques such as echocardiography or CMR enable the assessment of the functional consequences of myocarditis. However, there is no imaging technique available, that offers robust prognostic information during the inflammatory process that predicts the cardiac remodeling and development of dilated cardiomyopathy. Therefore the aim of the study was to assess the prognostic value of ultrasound molecular imaging of myocardial inflammation during the acute phase of myocarditis for late changes in the chronic phase.

3.2 Material & Methods

3.2.1 Study design and animal model

All experiments were performed in accordance with Swiss Federal Legislation and were approved by the Animal Care Committee of the Canton of Basel. A total of 54 female BALB/c mice were used for this study.

Imaging of the acute phase (Time point 1, T_1) in Myocarditis. In 54 mice, experimental autoimmune myocarditis (EAM) was induced as described (see chapter 2.2.1). On day 21 after induction, the following imaging datasets were acquired:

Day 21 imaging during acute phase

- high resolution transthoracic echocardiography,
- speckle tracking strain imaging,
- CEU molecular imaging for leukocytes, P-Selectin and $CD4^+$ lymphocytes.

Imaging of the chronic phase (Time point 2, T_2) The animals were then recovered and imaging was again performed during the chronic phase during myocarditis to assess the potential predictive value of molecular imaging for late changes. Analysis at this second time point at 63 days post induction included:

Day 63 long term imaging

- high resolution transthoracic echocardiography,
- speckle tracking strain imaging,
- invasive left ventricular pressure measurements.

Histology of the hearts at the mid-ventricular level was performed for the assessment of myocardial fibrosis.

3.2.2 Microbubble Preparation

Perfluorocarbon-filled, lipid-shelled microbubbles were prepared by sonification of a gas-saturated aqueous suspension of distearoyl-phosphatidylcholine (2 mg/ml; Avanti Polar Lipids, Alabaster AL, USA) and polyoxyethylene-(40)-stearate (1 mg/ml; Sigma-Aldrich, Buchs). These non-targeted microbubbles were used for the assessment of myocardial perfusion. Microbubbles for targeting of leukocytes (MB_{Lc}) were

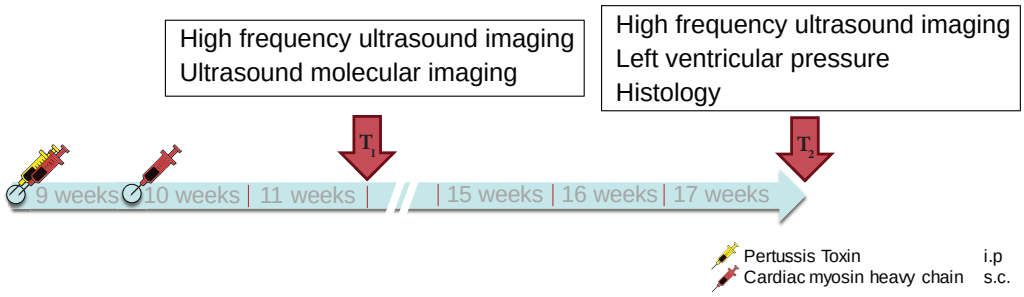

Figure 3.3: Study design. Animals were challenged with 2 injections containing cardiac α-myosin peptide and analyzed 3 weeks after induction of experimental autoimmune myocarditis. Mice were imaged again on day 63 post-induction and sacrificed only then for tissue collection.

prepared by adding distearoyl-phosphatidylserine (0.3 mg/ml; Avanti Polar Lipids) to the aqueous suspension before sonification [38].

For targeting of P-Selectin and CD4, distearoyl-phosphatidylethanolamine-PEG(3400)-biotin (0.14 mg/ml; Creative PEG Works, Chapel Hill, NC, USA) was added to the lipid suspension. Microbubbles targeted to P-Selectin (MB_{PSel}) and to CD4 (MB_{CD4}) were then prepared by conjugation of biotinylated anti-P-Selectin antibody (RB40.34, BD Bioscience) or anti-CD4 antibody (H129.19, BD Bioscience) to the microbubble surface using biotin-streptavidin-biotin linking as previously described [39]. Control microbubbles (MB_{Iso}) bearing a non-specific isotype control antibody (R3-34, BD Bioscience) were also prepared. Microbubble concentration and size were measured by electro-zone sensing (Multisizer III, Beckman-Coulter).

3.2.3 Animal instrumentation

On day 21 and day 63 post-immunization respectively, the mice were anesthetized as described (see chapter 2.2.4)
For microbubble injections on day 21, the right internal jugular vein was cannulated with 0.97 mm polyethylene tubing (PE-50, BD Diagnostics). The animals were transferred onto a temperature-regulated imaging stage (Vevo Imaging Station).
After the imaging procedure, the tube was removed and the right jugular vein ligated. The skin was sutured using a 6-0 mono-filament thread (Prolene, Ethicon, New Jersey). The animals were recovered from anesthesia and after regaining consciousness were treated with 0.1 mg/kg bodyweight buprenorphine s.c. (Temgesic, Schering-Plough, New Jersey) every 8 hours.

3.2.4 Echocardiography

High frequency (40MHz, MS 550D transducer) ultrasound imaging (Vevo 2100, VisualSonics Inc., Toronto, Canada) was performed for assessment of cardiac structure and function on both imaging time points T_1 and T_2.
M-Mode images of the left ventricle at the height of the papillary muscles were used to measure anterior and posterior wall thickness, left ventricular end-diastolic diameter (LVEDD) and left ventricular end-systolic diameter (LVESD). Left ventricular ejection fraction (EF) and left ventricular mass were derived from these measurements as described previously [40].
E-wave and A-wave velocity were measured using pulsed wave Doppler tracings from a modified apical 4-chamber view to assess flow across the mitral valve.
Para-sternal long- and short-axis B-mode images were acquired at a frame rate of >200 frames per second. Longitudinal, radial and circumferential global peak strain values were derived from the B-mode images using a speckle tracking algorithm (VevoStrain, VisualSonics) [41]. Briefly, cine-loops with two cardiac cycles not distorted by respiratory movements were selected and the endocardial and epicardial borders were traced on end-diastolic frames. After automated tracing, manual adjustments were made as necessary for good tracking throughout the cardiac cycles. The strain measurements were then averaged over the two cardiac cycles without the use of temporal smoothing filters.

3.2.5 Contrast Enhanced Ultrasound molecular Imaging

Contrast ultrasound imaging (Sequoia Acuson C512; Siemens Medical Systems USA Inc., Mountain View, CA) was performed with a high-frequency linear-array probe (15L8) held in place by a railed gantry system. The left ventricle was imaged in short axis at the papillary muscle level from a left parasternal window. ECG-gated triggering was used to acquire end-systolic frames. For the detection of the contrast agent, power modulation and pulse inversion (Contrast Pulse Sequence) imaging at a centerline frequency of 7 MHz and a dynamic range of 50 dB was used.

The gain settings were adjusted to levels just below visible noise speckle and held constant. MB_{Ctr}, MB_{Lc}, MB_{PSel}, or MB_{CD4} (3×10^6 microbubbles per injection) were injected intravenously in random order. Ultrasound imaging was paused from the

time of injection until eight minutes later when imaging was resumed at a mechanical index of 0.87. The first acquired image frame was used to derive the total amount of microbubbles present within the left ventricular myocardium (see Figure **??**). The microbubbles in the ultrasound beam were then destroyed with several (>10) high intensity image frames with a mechanical index of 1.9. Several image frames at a long pulsing interval (every 9 heartbeats) were subsequently acquired to measure signal attributable to freely circulating microbubbles. After log-linear conversion using known dynamic range lookup tables, frames representing freely circulating microbubbles were digitally subtracted from the first image to derive signal from attached microbubbles alone. Contrast intensity was measured from a region of interest encompassing the whole left ventricular myocardium. The selection of the region of interest was guided by fundamental frequency anatomic images of the left ventricle acquired at 14 MHz at the end of each individual imaging sequence.
At 63 days post-induction of myocarditis, the mice were not able to hemodynamically tolerate multiple fluid injections. Therefore, we abstained from performing perfusion imaging. In addition, it was not possible to perform ultrasound molecular imaging for all microbubble species in all animals. Thus, ultrasound molecular imaging data were acquired for 31 animals for MB_{CD4}, for 10 animals for MB_{PSel}, whereas data for MB_{Ctr} and MB_{Lc} were acquired for all animals.

3.2.6 Left ventricular pressure measurements

After high frequency echocardiographic assessments, mice were kept anesthetized (2% isoflurane) and transfered to a heating pad. The left internal carotid artery was surgically exposed. A 0.3 mm diameter manometer tipped catheter (PVR-1035, Millar, Oxford, England) was inserted through a small incision in the artery. The catheter was then carefully advanced through the aortic valve into the left ventricle (see figure).
Pressure parameters were recorded and analyzed with a MPVS System (AD Instruments, Dunedin, New Zealand).

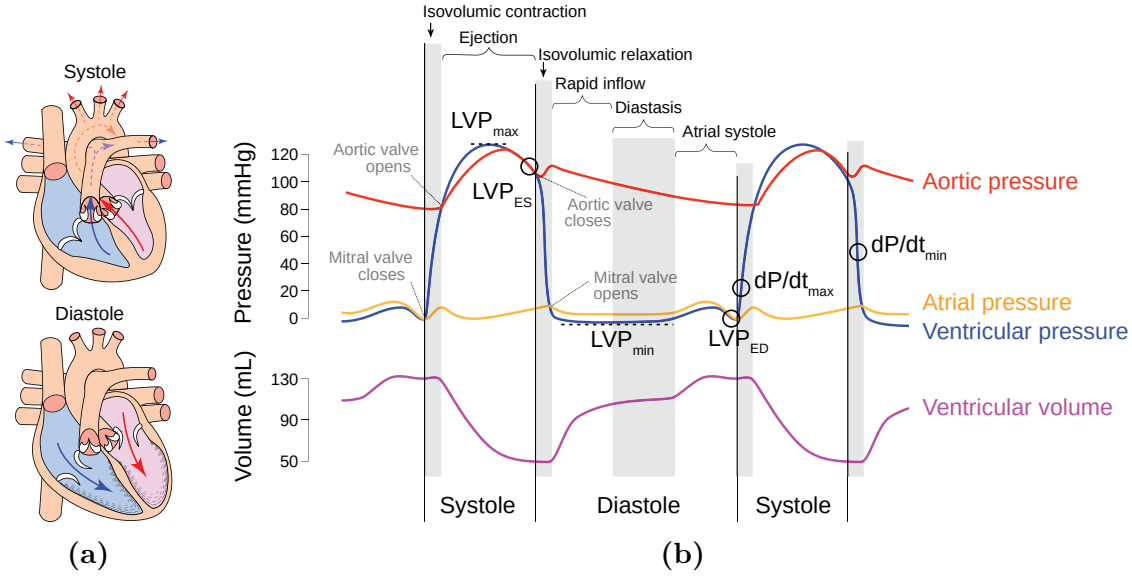

Figure 3.4: Schematic representation of the heart cycle. **(a)** Ventricular systole and diastole define the two major phases in the heart cycle. **(b)** Wiggers diagram of the heart cycle. Measured were left ventricular end systolic and end diastolic pressure respectively, maximal rate of left ventricular pressure rise and decrease respectively as well as the maximal aortic pressure.
LVP_{max}: Maximal left ventricular pressure; LVP_{min}: Minimal left ventricular pressure; LVP_{ES}: Left ventricular end systolic pressure; LVP_{ED}: Left ventricular end diastolic pressure; dP/dT_{max}: Maximal rate of left ventricular pressure rise; dP/dT_{min}: Maximal rate of left ventricular pressure decrease.

3.2.7 Histology

Collagen quantification in the myocardium was performed on short axis cross-sections of the hearts of animals that were sacrificed on day 63 post-induction of myocarditis. Heart tissue was fixed in 4% formaldehyde-solution and 5 µm thin sections were prepared using a water-slide microtome (HM 340E, Zeiss, Jena). The sections were stained with PicroSirius Red and counter-stained with hematoxyline. Full-spectrum RGB images of the stained myocardiums were recorded. The red channel was converted into a binary image using thresholding and the number of pixel above the threshold was averaged for 3 sections per individual animal. The area signal above the threshold in the left ventricular myocardium was normalized to the total tissue area and presented as a percentage value.

(a) **(b)** **(c)**

Figure 3.5: Fibrosis quantification. Red pixels display over-, blue underexposed pixels. The fibrosis score in this example was 7.2%. **(a)** original RGB image. **(b)** Binary image to retrieve total left-ventricular tissue area. **(c)** Binary image with threshold set to retrieve the collagen-positive area (red).

3.2.8 Statistical Analysis

The data was analyzed on GraphPad Prism (version 6.07).

Experimental data is expressed as mean ±SD unless stated otherwise. Echocardiographic *in vivo* data is presented as median (25th - 75th percentile) and preferential non-parametric statistical tests were used due to the distributions' non-Gaussian nature, small sample sizes and/or unresolvable outliers. Comparisons between two unpaired, non-parametric data sets were made using a Mann-Whitney rank sum test. Analysis of more than two unpaired, non-parametric sets were compared using a Kruskal-Wallis ANOVA with Dunn's post hoc test. Comparison between paired datasets (e.g. functional echocardiography at two different time points per animal) was done using a Wilcoxon matched-pair rank test. Correlations between 2 parameters (e.g. Fibrosis score vs. functional parameters) were assessed using Spearman correlation.

A two-sided p value <0.05 was considered as statistically significant.

3.3 Results Imaging of the chronic phase

3.3.1 Physiological parameters and structural and functional ultrasound imaging during the acute (T_1) and chronic phase (T_2) of myocarditis

Table 3.1 shows physiological parameters and ultrasound imaging data for structural and functional parameters assessed both during the acute phase (T_1, 21 days post-induction) and the chronic phase (T_2, 63 days post-induction) of myocarditis.

The physiological parameters included bodyweight and heart rate. Bodyweight increased significantly between time points T_1 and T_2, whereas heart rate was significantly decreased at time point T_2.

Physical heart weight was assessed only at time point T_2.

The dimensions of left ventricular anterior wall (LVAW) as well as posterior wall (LVPW) thicknesses decreased significantly between the two time-points (see Figure 3.6). In contrast, the left ventricular internal diameter (LVID) and subsequently the left ventricular volume increased both during diastole and systole.

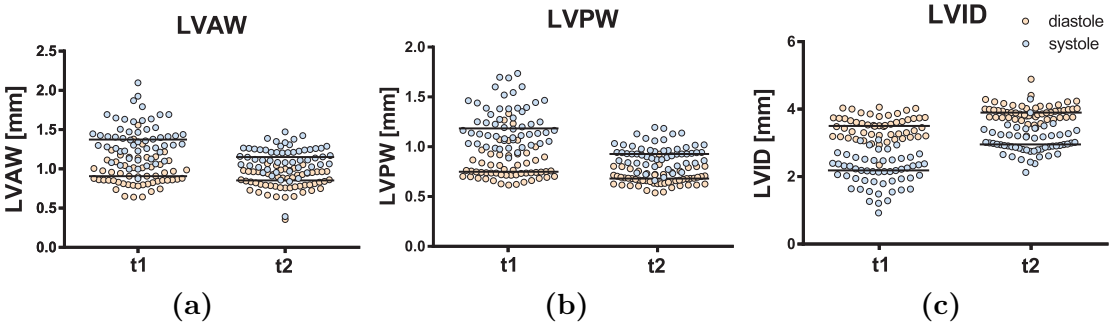

Figure 3.6: Dimensions of **(a)** left ventricular anterior wall, **(b)** posterior wall and **(c)** internal diameter for both time points T_1 (acute phase) and T_2 (chronic phase). Presented data is plotted as scatter with median.

For systolic functional parameters, the ejection fraction showed a significant decrease at time point T_2.

Global strain and strain rates decreased overall for radial, circular and longitudinal stain (see Figure 3.7 and Table 3.1).

Table 3.1: Comparisons of functional parameters measured during acute (T_1) and chronic phase (T_2) of myocarditis. Data is presented as median (25th - 75th percentile).

	Acute Phase (T_1)	Chronic Phase (T_2)	p-values
Physiological parameters			
Bodyweight (g)	21.1 (19.2 – 21.6)	22.7 (21.9 – 23.6)	**<0.001**
Heart rate (bpm)	421 (391 – 452)	364 (345 – 389)	**<0.001**
Heart weight (mg)	n/a	133 (127 – 144)	n/a
Echocardiographic parameters of LV structure			
LV Mass (mg)	84 (76 – 94)	86 (77 – 93)	n.s.
LV AW_d (mm)	0.91 (0.83 – 1.06)	0.85 (0.77 – 0.96)	**<0.01**
LV AW_s (mm)	1.37 (1.23 – 1.51)	1.15 (1.04 – 1.26)	**<0.001**
LV PW_d (mm)	0.75 (0.71 – 0.90)	0.68 (0.63 – 0.72)	**<0.001**
LV PW_s (mm)	1.19 (1.07 – 1.39)	0.93 (0.84 – 1.00)	**<0.001**
LV ID_d (mm)	3.50 (3.20 – 3.73)	3.90 (3.84 – 4.02)	**<0.001**
LV ID_s (mm)	2.10 (1.78 – 2.42)	2.87 (2.76 – 3.16)	**<0.001**
LV Vol_d (µl)	51 (41 – 59)	66 (60 – 71)	**<0.001**
LV Vol_s (µl)	14 (10 – 21)	32 (28 – 40)	**<0.001**
Echocardiographic parameters of LV systolic function			
Ejection fraction (%)	71 (65 – 78)	51 (44 – 56)	**<0.001**
$Strain_{rad}$ (%)	33 (25 – 42)	24 (19 – 27)	**<0.001**
$Strain_{circ}$ (%)	-18 (-22 – -16)	-13 (-15 – -10)	**<0.001**
$Strain_{long}$ (%)	8.7 (7.4 – 10.2)	6.9 (5.8 – 8.0)	**<0.01**
$Strainrate_{rad}$ (s^{-1})	-7.6 (-8.4 – -6.1)	-4.5 (-5.1 – -3.4)	**<0.001**
$Strainrate_{circ}$ (s^{-1})	-13 (-15 – -11)	-11 (-12 – -10)	**<0.001**
$Strainrate_{long}$ (s^{-1})	-5.6 (-6.8 – -5.1)	-4.4 (-4.7 – -3.7)	**<0.001**
Echocardiographic parameters of LV diastolic function			
E-wave velocity (mm s^{-1})	668 (586 – 744)	652 (559 – 811)	n.s.
A-wave velocity (mm s^{-1})	306 (178 – 359)	149 (51 – 209)	**<0.001**
E/A	1.9 (1.6 – 2.1)	4.0 (2.8 – 6.0)	**<0.001**

LV Mass Left ventricular mass; **LV AW_x** Left ventricular anterior wall during diastole or systole respectively; **LV PW_x** Left ventricular posterior wall during diastole or systole respectively; **LV ID_x** Left ventricular internal diameter during diastole or systole respectively; **LV Vol_x** Left ventricular volume during diastole or systole respectively; **Strain** Radial. circular or longitudinal strain respectively; **E-wave** early filling wave; **A-wave** atrial filling wave; **E/A** early/atrial filling velocity ratio

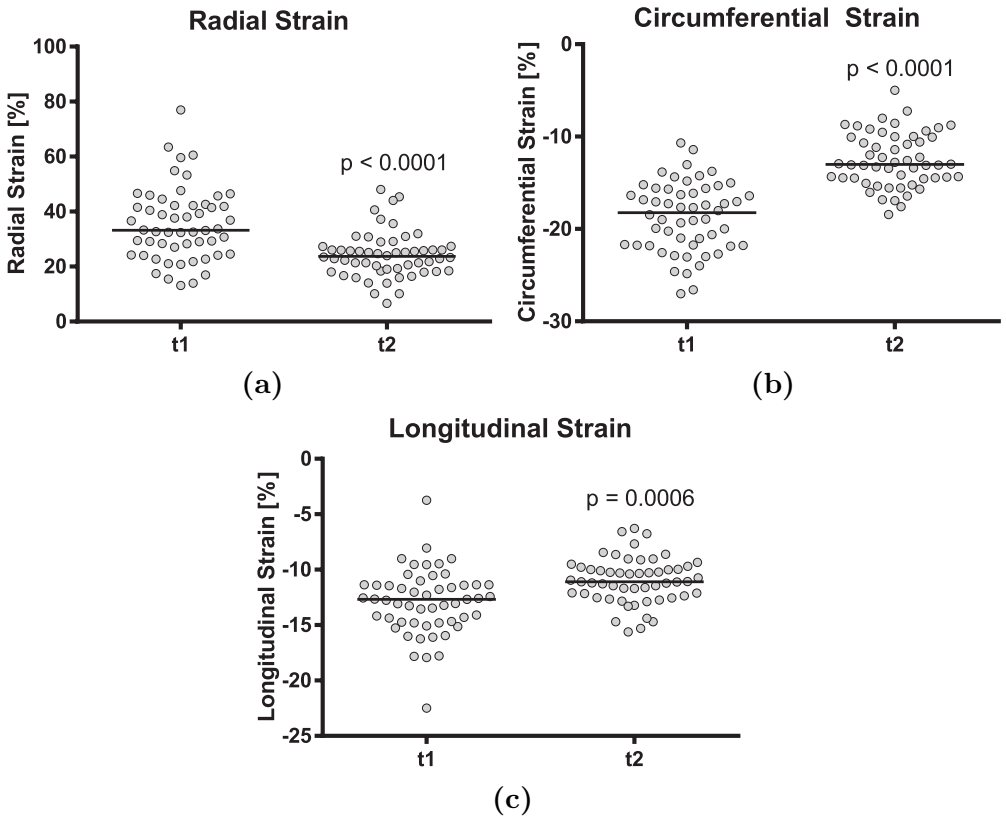

Figure 3.7: Strain data of both time points T_1 and T_2 for **(a)** radial strain, **(b)** circumferential strain and **(c)** longitudinal strain. Presented data is plotted with horizontal median.

Regarding diastolic indices, the E/A ratio was significantly increased (median of 1.9 for T_1 vs. 4.0 for T_2. see Figure 3.8) due to an increase in A-wave velocity (median of 306 mm/s vs. 149 mm/s) while E-wave velocities remained unchanged. Of note, the spread of E-velocities and thus E/A ratio was larger at T_2 than at T_1 potentially due to the different degrees of myocardial damage.

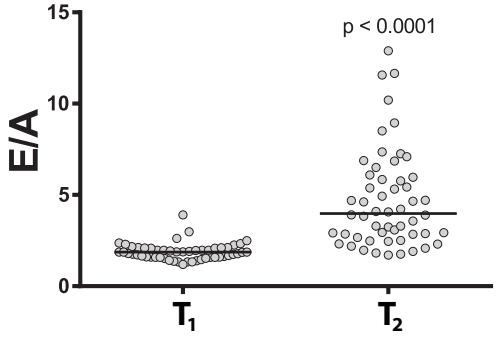

Figure 3.8: Spread of E/A ratios at time points T_1 and T_2.

3.3.2 Tissue fibrosis during the chronic phase (T_2)

Quantification of collagen-rich areas in PicroSirus-stained heart sections of 54 individual animals showed values ranging from 0.3% to 8.4% of the total myocardial area (Figure 3.9)

The extent of fibrosis did not show any correlation to the total myocardial area of the left ventricle.

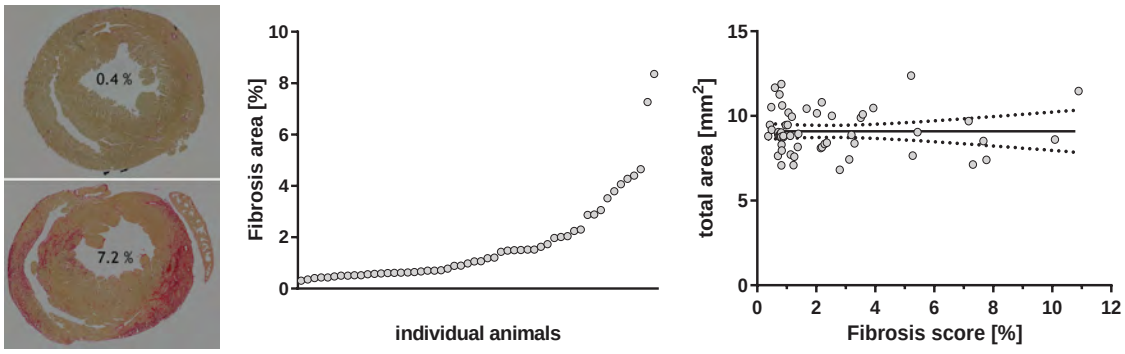

(a) **(b)** **(c)**

Figure 3.9: (**a**) Exemplary histology for an animal with low or high fibrotic area respectively. (**b**) Sorted plot of all scored animals. (**c**) Correlation of myocardial area against fibrotic area.

3.3.2.1 Correlation of functional parameters during T_1 with tissue fibrosis during T_2

Regression analysis was performed to assess whether functional parameters acquired during the acute phase of myocarditis (T_1) are able to predict structural changes that occur during the chronic phase (T_2) of myocarditis. The results of this regression analysis are presented in Table 3.2.

Significant but weak correlations to the extent of fibrosis were found for heart rate, left ventricular mass and the left ventricular posterior wall with higher values being predictive of more fibrosis.

Table 3.2: Correlation analysis of functional parameters measured during the acute phase (T_1) of myocarditis with the fibrosis score at the chronic phase (T_2). Data presented are nonparametric Spearman coefficients (r_s) and respective two-tailed p values.

	vs. Fibrosis (T_2)	
	r_s	p-value
Physiological parameters		
Bodyweight (g)	−0.09	0.51
Heartrate (bpm)	0.28	0.042*
Echocardiographic parameters of LV structure		
LV Mass (mg)	0.32	0.019*
LV AW_d (mm)	0.10	0.47
LV AW_s (mm)	0.01	0.92
LV PW_d (mm)	0.32	0.020*
LV PW_s (mm)	0.17	0.23
LV ID_d (mm)	0.03	0.84
LV ID_s (mm)	0.16	0.24
LV Vol_d (µl)	0.04	0.80
LV Vol_s (µl)	0.16	0.24
Echocardiographic parameters of LV systolic function		
Ejection Fraction (%)	−0.22	0.10
$Strain_{rad}$ (%)	−0.16	0.25
$Strain_{circ}$ (%)	0.22	0.11
$Strain_{long}$ (%)	0.24	0.09
$Strainrate_{rad}$ (s^{-1})	−0.18	0.20
$Strainrate_{circ}$ (s^{-1})	0.24	0.09
$Strainrate_{long}$ (s^{-1})	−0.02	0.88
Echocardiographic parameters of LV diastolic function		
E-wave velocity (mm s^{-1})	−0.08	0.55
A-wave velocity (mm s^{-1})	−0.16	0.25
E/A	0.12	0.40

LV Mass Left ventricular mass; **LV AW_x** Left ventricular anterior wall during diastole or systole respectively; **LV PW_x** Left ventricular posterior wall during diastole or systole respectively; **LV ID_x** Left ventricular internal diameter during diastole or systole respectively; **LV Vol_x** Left ventricular volume during diastole or systole respectively; **Strain** Radial. circular or longitudinal strain respectively; **E-wave** early filling wave; **A-wave** atrial filling wave; **E/A** early/atrial filling velocity ratio

3.3.2.2 Correlation of ultrasound molecular imaging during T_1 with tissue fibrosis during T_2

A second regression analysis was performed to assess whether molecular imaging data acquired during the acute phase of myocarditis (T_1) is able to predict structural changes that occur during the chronic phase (T_2) of myocarditis.

The results showed a positive correlation with tissue fibrosis for control microbubbles (MB_{Iso}), microbubbles targeted to CD4 (MB_{CD4}) and microbubbles targeted to activated leukocytes (MB_{Lc}) with the largest correlation coefficient for MB_{CD4} (see Figure 3.10).

While the results for microbubbles targeted to P-Selectin (MB_{PSel}) showed a higher correlation coefficient with fibrosis, this was not significant due to the low number of animals that received MB_{PSel}.

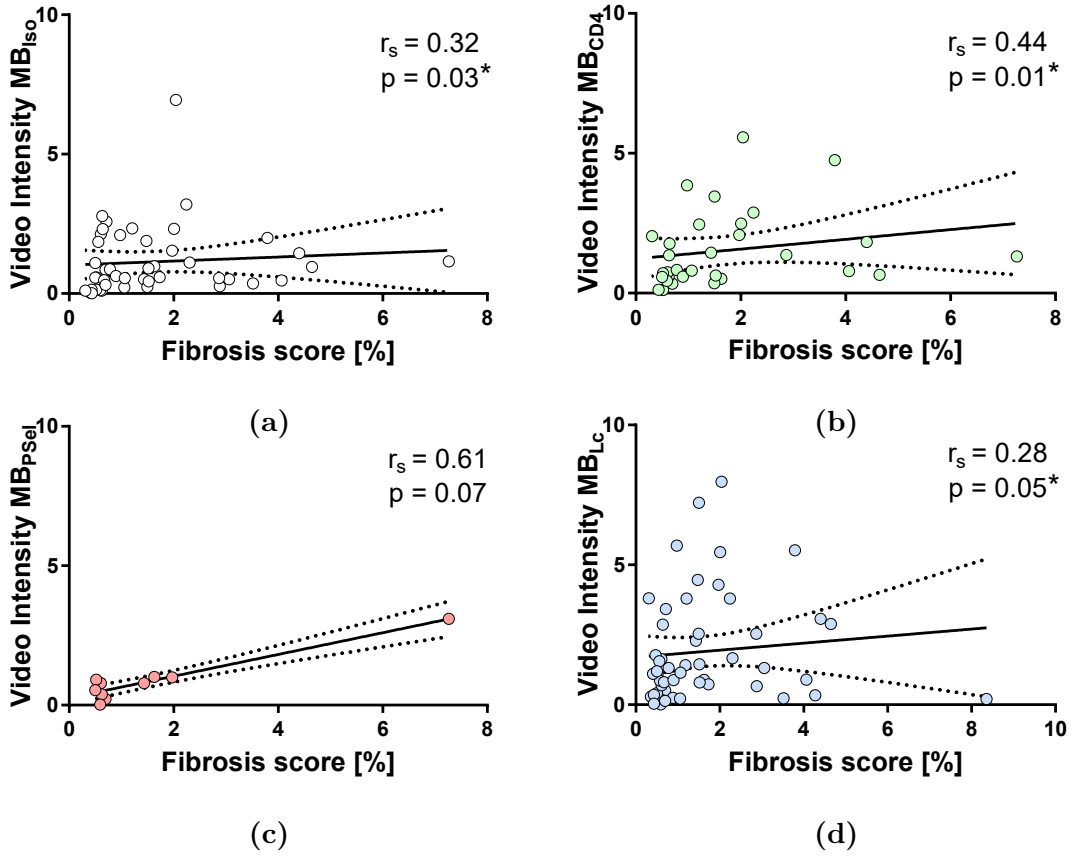

Figure 3.10: Correlation fibrosis vs. signal from **(a)** isotype control microbubbles MB_{Iso}, **(b)** CD4-targeted microbubbles MB_{CD4}, **(c)** P-Selectin-targeted microbubbles MB_{PSel} and **(d)** microbubbles targeted to activated leukocytes MB_{Lc}.

3.3.3 Invasive hemodynamic measurements during the chronic phase (T_2)

Results of invasive hemodynamic measurements are shown in Table 3.3. In comparison to published values of healthy mice under isoflurane anesthesia [76], the pressure at end of the systole was slightly reduced while the end-diastolic pressure was significantly increased.

The maximal peak rate of pressure rise (dP/dt_{max}) as well as pressure decline (dP/dt_{min}) were both decreased and in contrast, the left ventricular relaxation constant Tau was increased.

Table 3.3: Invasive hemodynamic measurements during the chronic phase (T_2) of myocarditis and their published normal range in healthy mice anesthetized with isoflurane. Experimental data is presented as median (25th - 75th percentile).

	Chronic phase (T_2)		Published values [76]	Change vs. normal
P_{es} (mmHg)	89	(83 – 92)	92 – 118	–
P_{ed} (mmHg)	12.5	(8.2 – 17.0)	1 – 6	++
dP/dt_{max} (mmHg s^{-1})	6597	(5518 – 7245)	7700 – 14480	– –
-dP/dt_{min} (mmHg s^{-1})	5987	(6968 – 5102)	6900 – 10400	– –
Tau (ms)	12.4	(9.6 – 14.3)	4.4 – 7.6	++
AP_{max} (mmHg)	90	(86 – 93)	n.a.	n.a.

$P_{es/ed}$ end systolic / diastolic pressure; **dP/dt** maximal/minimal rate of pressure generation; **Tau** Isovolumic relaxation constant; **$AP_{max/min}$** Maximal/minimal aortic pressure

3.3.3.1 Correlation of functional parameters during T_1 with hemodynamic measurements during T_2

Regression analysis was performed to assess whether functional parameters acquired during the acute phase of myocarditis (T_1) are able to predict changes of hemodynamic parameters. In Table 3.4, correlations for end-systolic pressure (P_{es}), end-diastolic pressure (P_{ed}) and the maximal rate of pressure change (dP/dt_{max}) are shown.

Significant, but weak correlations to the increase in P_{es} was found for the heart rate.

The dimensions of the left ventricular posterior wall during systole was correlated to end-systolic pressure with thinner wall dimensions predicting a lower P_{es}. The left ventricular internal diameter showed an inverse correlation to end-systolic pressure, with a larger internal diameter (both in diastole and systole) predicting a lower P_{es}. A greater left ventricular volume (both in diastole as well as systole) correlated with a lower end-systolic pressure as well.

The ejection fraction showed a correlation to end-systolic pressure with low values predicting a lower P_{es}.

Ratio of E to A-wave velocity showed a trend but a significant correlation was found only for the A-wave velocity with higher velocities predicting a higher end-systolic pressure.

However, an increase or decrease in end-diastolic pressure (P_{ed}) was not predicted by any of the assessed functional parameters except E-wave velocity, with lower velocity values indicating a higher end-diastolic pressure.

The maximal left ventricle pressure rise (dP/dt_{max}) showed a positive correlation to heart rate.
Ventricular dimensions showed a general trend similar to the results for P_{es}. However, significant correlations were only observed for internal diameter and ventricular volume during systole.

The ejection fraction showed a positive correlation as did E- and A-wave velocities.

Table 3.4: Correlation analysis of functional parameters measured during the acute phase (T_1) of myocarditis with hemodynamic measurements at the chronic phase (T_2). Data presented are nonparametric Spearman coefficients (r_s) and respective two-tailed p values.

	vs. P_{es} (T_2)		vs. P_{ed} (T_2)		vs. $\frac{dP}{dt_{max}}$ (T_2)	
	r_s	p-value	r_s	p-value	r_s	p-value
Physiological parameters						
Bodyweight (g)	0.07	0.60	−0.19	0.18	0.14	0.33
Heartrate (bpm)	0.35	0.010**	−0.10	0.47	0.28	0.04 *
Echocardiographic parameters of LV structure						
LV Mass (mg)	−0.11	0.41	−0.16	0.24	−0.11	0.41
LV AW_d (mm)	0.09	0.51	−0.12	0.38	0.02	0.88
LV AW_s (mm)	0.17	0.22	−0.10	0.47	0.11	0.42
LV PW_d (mm)	0.24	0.08	0.17	0.21	0.23	0.09
LV PW_s (mm)	0.34	0.012*	0.21	0.13	0.24	0.08
LV ID_d (mm)	−0.33	0.016*	−0.16	0.26	−0.24	0.07
LV ID_s (mm)	−0.36	0.007**	−0.11	0.44	−0.30	0.03 *
LV Vol_d (µl)	−0.32	0.020*	−0.16	0.24	−0.24	0.08
LV Vol_s (µl)	−0.36	0.007**	−0.11	0.44	−0.30	0.03 *
Echocardiographic parameters of LV systolic function						
Ejection Fraction (%)	0.35	0.009**	0.07	0.61	0.31	0.02 *
$Strain_{rad}$ (%)	−0.08	0.57	−0.14	0.32	0.07	0.63
$Strain_{circ}$ (%)	−0.01	0.92	0.06	0.65	0.00	0.99
$Strain_{long}$ (%)	0.12	0.40	0.08	0.58	0.14	0.31
$Strainrate_{rad}$ (s^{-1})	0.04	0.75	−0.12	0.40	0.13	0.36
$Strainrate_{circ}$ (s^{-1})	−0.17	0.22	−0.09	0.52	−0.13	0.35
$Strainrate_{long}$ (s^{-1})	−0.06	0.67	−0.08	0.59	−0.09	0.53
Echocardiographic parameters of LV diastolic function						
E-wave velocity (mm/s)	0.16	0.26	−0.30	0.03 *	0.30	0.03 *
A-wave velocity (mm/s)	0.34	0.012*	−0.13	0.36	0.34	0.013*
E/A	−0.26	0.06	−0.01	0.95	−0.21	0.13

P_{es} Left ventricular end systolic pressure; **P_{ed}** Left ventricular end diastolic pressure; **dP/dt_{max}** maximal rate of pressure generation; **LV Mass** Left ventricular mass; **LV AW_x** Left ventricular anterior wall during diastole or systole respectively; **LV PW_x** Left ventricular posterior wall during diastole or systole respectively; **LV ID_x** Left ventricular internal diameter during diastole or systole respectively; **LV Vol_x** Left ventricular volume during diastole or systole respectively; **Strain** Radial. circular or longitudinal strain respectively; **E-wave** early filling wave; **A-wave** atrial filling wave; **E/A** early/atrial filling velocity ratio

3.3.3.2 Correlation of ultrasound molecular imaging during T_1 with hemodynamic measurements during T_2

Regression analysis for molecular imaging data during the acute phase (T_1) with the end-systolic pressure (P_{es}) during the chronic phase is presented in Figure 3.11. P_{es} showed a negative correlation for leukocyte-targeted microbubbles (MB_{Lc}), with higher signal predicting lower end-systolic pressure. Signals from microbubbles targeted to CD4 (MB_{CD4}) or control microbubbles (MB_{Iso}) showed a trend towards a negative relation, but this was statistically not significant. The limited data available for P-Selectin targeted microbubbles did not show any correlation.

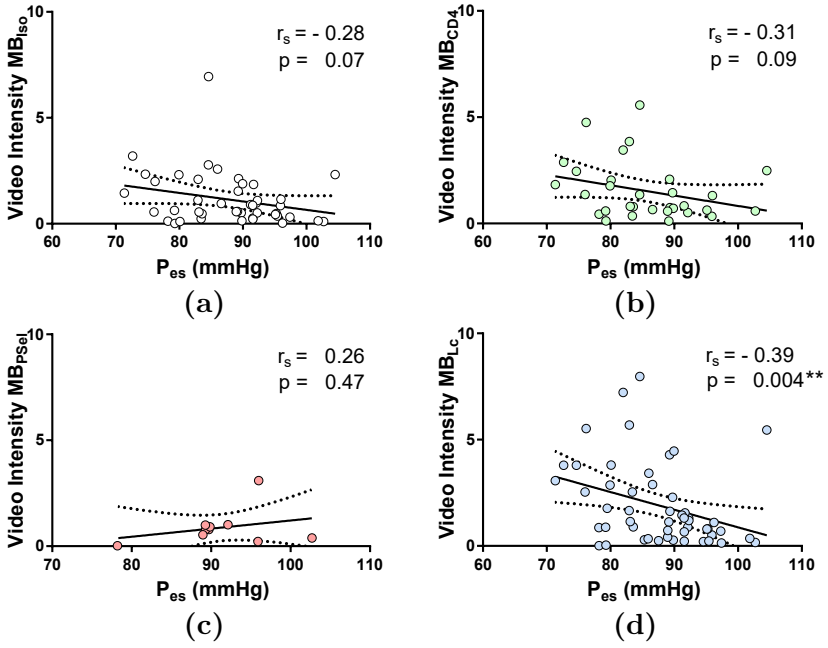

Figure 3.11: Correlation of end-systolic pressure (P_{es}) vs. signal for **(a)** isotype control microbubbles (MB_{Iso}), **(b)** CD4-targeted microbubbles (MB_{CD4}), **(c)** P-Selectin-targeted microbubbles (MB_{PSel}) and **(d)** microbubbles targeted to activated leukocytes (MB_{Lc}).

Regression analysis with the end-diastolic pressure (P_{ed}) during the chronic phase is presented in Figure 3.12. P_{ed} showed a negative correlation for leukocyte-targeted microbubbles (MB_{Lc}) and isotype control microbubbles (MB_{Iso}). Signals from microbubbles targeted to CD4 (MB_{CD4}) and P-Selectin (MB_{PSel}) did not show any correlation.

Regression analysis with the maximal rate of rise of left ventricular pressure (dP/dT_{max}) during the chronic phase is presented in Figure 3.13. All microbubble species did not show any correlation with dP/dT_{max}.

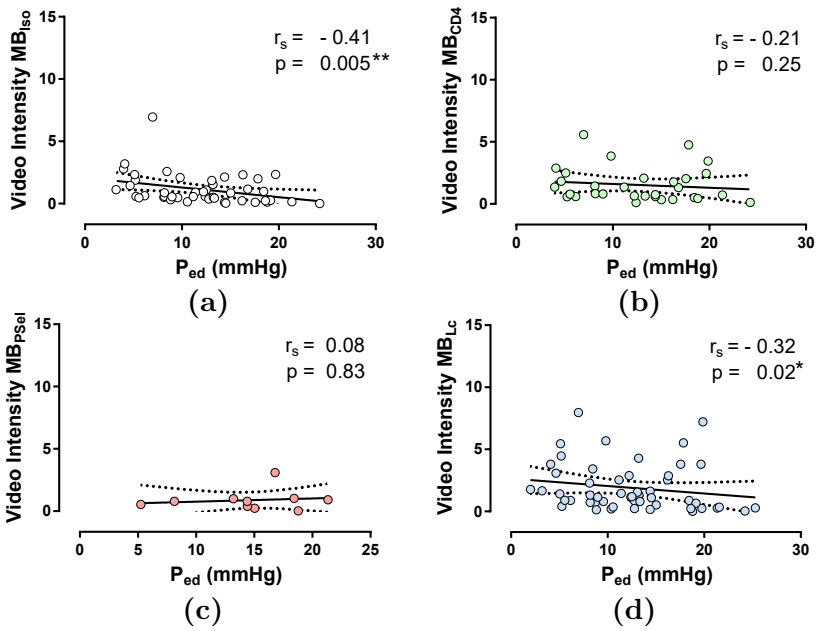

Figure 3.12: Correlation of end-diastolic pressure (P_{ed}) signal for **(a)** isotype control microbubbles, **(b)** CD4-targeted microbubbles, **(c)** P-Selectin-targeted microbubbles and **(d)** microbubbles targeted to activated leukocytes.

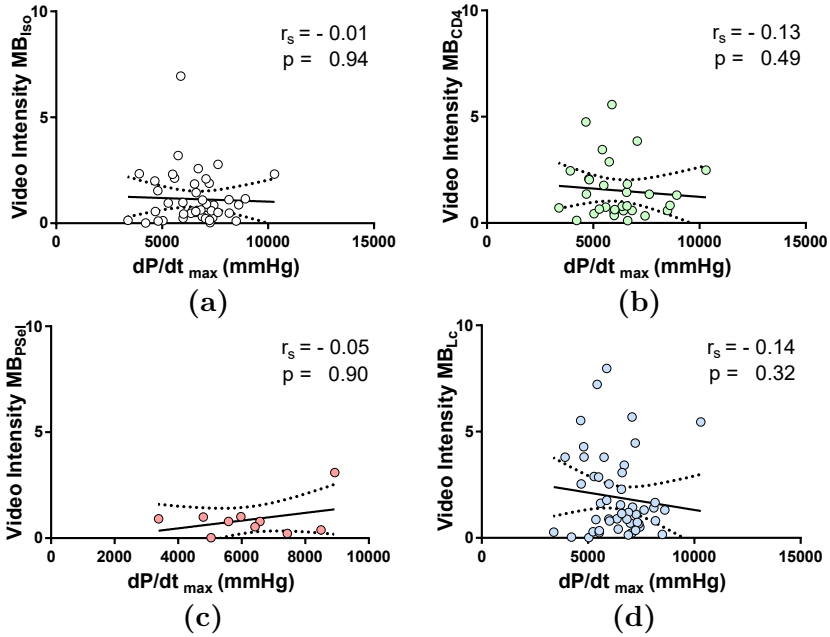

Figure 3.13: Correlation of maximal rate of rise of left ventricular pressure (dP/dT_{max}) signal for **(a)** isotype control microbubbles, **(b)** CD4-targeted microbubbles, **(c)** P-Selectin-targeted microbubbles and **(d)** microbubbles targeted to activated leukocytes.

3.3.4 Ejection fraction during the chronic phase (T_2)

3.3.4.1 Correlation of functional parameters during T_1 with ejection fraction during T_2

Regression analysis was performed to assess whether functional parameters acquired during the acute phase of myocarditis (T_1) are able to predict a systolic dysfunction with a reduction in ejection fraction during the chronic phase (T_2).
The results are shown in Table 3.6 on page 76.

For all parameters, only the heart rate and left ventricular mass showed a correlation, with higher values being predictive for a reduction in ejection fraction.

3.3.4.2 Correlation of ultrasound molecular imaging during T_1 with ejection fraction at T_2

Regression analysis was performed to assess whether molecular imaging data acquired during the acute phase of myocarditis (T_1) is able to predict a reduction in ejection fraction in the chronic phase (T_2) of myocarditis.
The results are shown in Table 3.5.

For the applied microbubbles there was no correlation with a change in ejection fraction observed.

Table 3.5: Correlation analysis of ultrasound molecular imaging during the acute phase (T_1) of myocarditis with the ejection fraction during the chronic phase (T_2). Data presented are nonparametric Spearman coefficients (r_s) and respective two-tailed p values.

	vs. Ejection Fraction (T_2)	
	r_s	p-value
MB_{Iso}	0.08	0.60
MB_{CD4}	−0.13	0.47
MB_{PSel}	−0.37	0.29
MB_{Lc}	−0.11	0.45

$\mathbf{MB_{Iso}}$ Isotype control microbubbles; $\mathbf{MB_{CD4}}$ Microbubbles targeted against CD4; $\mathbf{MB_{PSel}}$ Microbubbles targeted against P-Selectin; $\mathbf{MB_{Lc}}$ Microbubbles targeted against activated Leukocytes

Table 3.6: Correlation analysis of functional parameters measured during the acute phase (T_1) of myocarditis with ejection fraction at the chronic phase (T_2). Data presented are nonparametric Spearman coefficients (r_s) and respective two-tailed p values.

	vs. Ejection fraction (T_2)	
	r_s	p-value
Physiological parameters		
Bodyweight (g)	−0.08	0.57
Heart rate (bpm)	−0.34	0.012*
Echocardiographic parameters of LV structure		
LV Mass (mg)	−0.31	0.02 *
LV AW_d (mm)	−0.17	0.23
LV AW_s (mm)	−0.03	0.83
LV PW_d (mm)	−0.08	0.59
LV PW_s (mm)	−0.07	0.60
LV ID_d (mm)	−0.11	0.42
LV ID_s (mm)	−0.18	0.19
LV Vol_d (µl)	−0.13	0.36
LV Vol_s (µl)	−0.18	0.19
Echocardiographic parameters of LV systolic function		
Ejection Fraction (%)	0.20	0.15
$Strain_{rad}$ (%)	−0.03	0.84
$Strain_{circ}$ (%)	−0.03	0.85
$Strain_{long}$ (%)	−0.13	0.37
$Strainrate_{rad}$ (s^{-1})	−0.04	0.78
$Strainrate_{circ}$ (s^{-1})	−0.02	0.90
$Strainrate_{long}$ (s^{-1})	0.12	0.37
Echocardiographic parameters of LV diastolic function		
E-wave velocity (mm/s)	−0.16	0.25
A-wave velocity (mm/s)	−0.27	0.05
E/A	−0.02	0.88

LV Mass Left ventricular mass; **LV AW_x** Left ventricular anterior wall during diastole respectively systole; **LV PW_x** Left ventricular posterior wall; **LV ID_x** Left ventricular internal diameter; **LV Vol_x** Left ventricular volume; **Strain** Radial. circular or longitudinal strain respectively; **E-wave** early filling wave; **A-wave** atrial filling wave; **E/A** early/atrial filling velocity ratio

3.4 Discussion

Myocarditis and the ensuing inflammatory autoimmune process can lead to chronic dilated cardiomyopathy and heart failure. Currently available non-invasive imaging methods detect the functional or structural consequences of infection or inflammation such as tissue necrosis or edema and are limited in diagnostic accuracy at best. There is no diagnostic tool available to date that can predicts long-term effects such as ventricular dilatation, development of heart failure or the need for heart transplantation. Therefore, we examined whether contrast enhanced ultrasound molecular imaging during the acute phase of myocarditis could be used to predict functional impairments and structural changes in the chronic stage of myocarditis.

The main conclusion of these experiments is that ultrasound molecular imaging during the acute phase correlates to the extent of tissue fibrosis that subsequently develops in the chronic phase. However, this relation is weak and the clinical usefulness is debatable.

Changes in physiological and echocardiographic parameters during the chronic phase of myocarditis

Physiological parameters like body weight or heart rate changed significantly between the acute phase (T_1) and chronic phase (T_2) of myocarditis. The age of the animals at time point T_1 and T_2 was 11 ± 1 weeks and 17 ± 1 weeks respectively, and thus a natural increase in body weight was expected. Comparisons with strain-specific weight charts showed a normal increase in weight and a moderately lower body weight for both time points. The moderate weight difference for both time points compared to age-matched reference charts can be explained by the induced inflammation, which causes pain and malaise as well as pathological effects on hemodynamics and metabolism that myocarditis causes.

An age-dependent decrease in heart rate, as seen here in the course over six weeks, is known in the process of aging [77]. However, the observed reduction can potentially be explained by a underlying second cause. During the ongoing inflammatory immune reaction in the myocardium, the heart rate is reported to be significantly increased in patients suffering myocarditis [43] caused by an increased level of circulating pro-inflammatory cytokines that exert a systemic effect during the acute

phase. With a decreasing immune reaction, the heart rate will normalize eventually.

The structural parameters for anterior and posterior wall thickness are globally decreased in the chronic phase (T_2). When animals with severe myocarditis were compared with control animals in chapter 2.3.3, especially posterior wall thicknesses showed a marked thickening in the acute phase (T_1) due to the ongoing inflammatory response. The subsiding of the acute inflammation leads to a volumetric reduction of the inflamed and edematous tissue. Animals with severe myocarditis will eventually progress into dilated cardiomyopathy with further decreasing LV wall-thicknesses and widened cavity which falls in line with clinical observations in humans [78].

The parameters of systolic function, including ejection fraction as a measure for the amount of blood ejected out of the left ventricle and myocardial strain as a measure of myocardial mechanics show a general decline as it would have been expected for chronic dilated cardiomyopathy and heart failure.

The E-wave (or early ventricular filling) velocity is primarily influenced by pressure gradients between left atrium – left ventricle and the rate of the ventricular relaxation during diastole. The A-wave (or late ventricular filling) velocity on the other hand is a measure for the velocity at atrial contraction and depends on left atrial volume and contractile forces as well as the left ventricular chamber compliance C, defined as a change of volume over pressure ($C = \frac{\Delta V}{\Delta P}$).

Although a significant reduction of E-wave velocities was observed in animals with severe myocarditis compared to control animals in the acute phase, the effect is most likely caused by a reduced ventricular relaxation. However, there was no observable difference in E-wave velocity between time points T_1 and T_2.

In contrast, comparisons between time points T_1 and T_2 revealed a significant decrease in A-wave velocity which changed the E/A ratio accordingly. The ratio E/A showed a median increase from 1.9 to 4.0, and the ratios during T_1 showed a very small variability, while the measurements during T_2 spread over a much broader range.

A reduction in A-wave velocity and thus an increased E/A ratio with unchanged E-wave velocity could either suggest atrial dysfunction, which is associated with dilated cardiomyopathy caused by atrial fibrosis and prevents the appropriate gen-

eration of pressure to evacuate the atrium effectively. Or it could suggest a reduced compliance of the left ventricle, indicating the inability of the myocardium to react to the increased pressure with further sarcomer and matrix-stretching which is usually observed in hypertrophic cardiomyopathy [79], and increased fibrotic remodeling where myocardial stiffening has been reported to lead to a decrease in diastolic function [80].

Parameters that predict left ventricular fibrosis during the chronic phase of myocarditis

The assessment of fibrosis area was performed on PicroSirius Red stained transversal heart sections. Overall, the analyzed animals showed a median collagen-positive area of 1% of the total stained myocardium which is comparable to findings with an average of 1% in healthy heart tissue for humans [81] and rats [82]. The collagen-rich area is increased considerably in pathological situations as in dilated cardiomyopathies (average of 7 %, [81]) or in myocardial infarction, where the content can vary over a broad range and can constitute close to 100% in scar tissue [83].
Thus sixteen of the 54 analyzed animals in the cohort showed a fibrosis score greater than 2% of total tissue area, indicating an increased collagen deposition by cardiac fibroblasts as a consequence of cardiomyocyte damage in myocarditis.

Correlation analysis with functional parameters showed a positive relation with heart rate during the acute phase (T_1). The link between the development of fibrosis and an increased heart rate is not well understood. There is however a well known association of increased heart-rate with systolic heart failure and patients with dilated cardiomyopathy or ischemic heart diseases can show tachycardia (increased resting heart rate) [84]. The most likely explanation is a compensatory mechanism to counteract the decreased cardiac output for the single stroke sensed amongst others by baroreceptors or by the action of circulating pro-inflammatory cytokines as a systemic side effect of severe inflammation [85]. While other conditions can contribute to an increase in heart-rate as well (e.g. pulmonary fibrosis, tachycardia ameliorated cardiomyopathies), no screening for electrocardiographic irregularities or pulmonary histology of the analyzed mice was performed.

The extent of fibrosis during T_2 correlated with an increase of the cavity diameter

and thus ventricular volume during the chronic stage of myocarditis (T_2). However, this was not the case for the acute phase (T_1), where no structural parameter other than the left ventricular posterior wall during diastole and LV mass had a predictive quality.
The mechanisms behind that and the contrast to the clinical presentation with a decrease in wall thicknesses is not well understood, but the increase in posterior wall thickness does match the clinical observations that the posterior wall is more frequently affected by fibrotic remodeling than the lateral or septal walls [86]. While extensive matrix remodeling is expected at locally defined sites of damage, the myocardial wall thinning is expected to occur diffusely. No other parameters during T_1, especially parameters for systolic and diastolic function did show a correlation to the extent of tissue fibrosis during T_2.

Contrast enhanced molecular ultrasound on the other hand, did show a moderate correlation for signal from CD4-targeted microbubbles, from microbubbles targeted to activated leukocytes and interestingly from isotype control microbubbles to the extent of fibrosis.

Microbubbles for $CD4^+$ cells and activated leukocytes are specific for cellular components of the inflammatory response in myocarditis and an increased signal during the acute phase (T_1), that is caused by an increased number of attached cells at the myocardial endothelium predicts the extent of fibrosis during the chronic phase (T_2).

Of note is the positive correlation with signal from isotype-control microbubbles. These control microbubbles did not show attachment to $CD4^+$ cells or CD4 protein *in vitro* and *in vivo* experiments during the acute phase, a significant signal enhancement of $CD4^+$ targeted microbubbles was shown relative to isotype-controls. However, an increased attachment of control microbubbles to phagocytic leukocytes on the endothelium and thus increase in signal intensity for MB_{Iso} is expected [87]. Due to the inflammatory milieu, molecular changes of the endothelium will attract an increased number of innate phagocytic cells, which will bind pathogen-associated molecular patterns and non-self molecules and thus increase the measured signal for all microbubbles.

Since the signal intensity both for $MB_{\mathbf{CD4}}$ and $MB_{\mathbf{Lc}}$ is not significantly increased relative to signal from $MB_{\mathbf{Iso}}$, it does not allow for further deductions about the

role of $CD4^+$ cells or activated leukocytes in respect of the progression to dilated cardiomyopathy.

Parameters that predict hemodynamic changes during the chronic phase of myocarditis

Compared to published values for healthy mice, the hemodynamic changes during the chronic phase in myocarditis reported here were an increased end-diastolic pressure and the relaxation constant tau, while a reduction was found for end-systolic pressure and the maximal rate of pressure rise and pressure decrease, respectively.

Interestingly, there was no correlation of fibrosis during the chronic stage (T_2) with a reduced capability of the heart to generate high discharge pressure at the end of systole or with any other hemodynamic parameter during the chronic phase (T_2).

To further investigate this, all functional parameters measured at T_2 were tested against the extent of fibrosis. There was no correlation found between fibrosis and ejection fraction, strain or strain-rate or any pressure parameters during the chronic phase (T_2). A correlation was found for heart rate, LV mass and structural parameters (LV volume and internal diameter). This suggests, that the extent of fibrosis in the used model has only limited influence on both systolic and diastolic function which is surprising given the fact that myocardial fibrosis is a result of cardiac damage during myocardial inflammation.

However, a prognostic value for a reduced end-systolic pressure was found for increased LV diameters and volumes during the acute phase. Since severe myocarditis was correlated with a reduction in LV diameter and volume because of the myocardial selling during inflammation, this would indicate a potential higher end-systolic pressure at time point T_2 for animals that developed myocarditis.

This is also confirmed by heart rate, which is elevated during acute myocarditis and is correlated as well to a higher end-systolic pressure during the chronic stage (T_2). Correlation analysis for the maximal rate of pressure rise (dP/dt_{max}) showed similar relations to heart rate, LV diameter and LV volume as well as ejection fraction.

The end-diastolic pressure at the chronic stage (T_2) was increased compared to values found in the literature, but was not predicted by any of the analyzed parameter during the acute phase.

Signals for microbubbles showed either a trend (MB_{CD4}) or significant correlation (MB_{Lc}) with a reduction in LV end-systolic and maximal aortic pressures, falling in line with the expected loss of contractile force of dilated ventricles in myocarditis. The signals for MB_{Lc} showed a correlation with a decrease in LV end-diastolic pressure as well.

Patients with dilated cardiomyopathy have a LV end-diastolic pressure-volume relationship that is shifted to the right. The left ventricle can tolerate a higher volume at the same pressure and importantly generates pressure at a lower rate than normal ventricles [89]. A lower end-diastolic pressure in dilated ventricles is caused by two mechanisms.

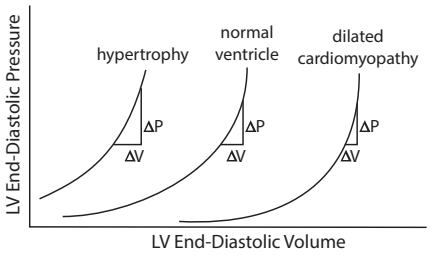

Figure 3.14: Volume-pressure curve for hypertrophic, normal and dilated ventricles. A higher pressure is needed for hypertrophic ventricles, to reach the same volume. Dilated ventricles however offer a higher volume at the same pressure and show a more distensible ventricle. From Little et al. [88]

Fist, sliding displacement of cardiomyocytes and a decrease of wall thickness of the ventricle [90] causes a systolic dysfunction with a decrease of force that can be generated during systole. Extensive matrix degradation and collagen synthesis lead to a loss of fibrillar collagen, which has an important elastic function in storing the energy generated during systole and is released early in diastole to relax the ventricle [91]. With a decrease in systolic pressure and a reduced spring-loaded matrix, the ventricle is impaired in its inertial acceleration and does not develop a proper pressure-gradient or suction between ventricle and atrium [92].

The second mechanisms is due to the cavity dilation, hemodynamic turbulences are introduced which lead to convective deceleration of the inflowing blood [92] that withstands the ventricular pressurization.

Parameters that predict a decreased ejection fraction during the chronic phase of myocarditis

A decrease in ejection fraction, which is the clinical definition of dilated cardiomyopathy, was observed between time points T_1 and T_2. Additionally, during the chronic phase there was a very strong correlation of a decreased ejection fraction with an increase in left ventricular diameter and volume ($r_s \leq$-0.5; $p \leq 0.001$) clearly indicating a progression to ventricular dilation and a reduced systolic function.

However, during the acute phase in myocarditis, only heart rate and left ventricular mass showed a significant correlation with a reduced ejection fraction during the chronic phase. No other functional parameter or finding in structural and functional echocardiography during the acute phase was able to predict a reduced systolic function during the chronic stage of myocarditis.

Ultrasound molecular imaging, which is able to detect acute inflammation during the acute phase of myocarditis, showed no correlation to the reduced ejection fraction in the chronic stage as well. This indicates that the progression from an inflamed myocardium, which can be detected using ultrasound molecular imaging, into dilated cardiomyopathy with reduction in systolic function, is not inevitable or has other a more complex development.

The animal model, that was used and which is susceptible for the induction of myocardial inflammation with cardiac myosin, will develop myocarditis in approximately 60% of induced animals. However, there is very little data available on the compensatory mechanisms of the murine heart in myocarditis and the progression to dilated cardiomyopathy. Additionally, rodents differ profoundly both in their immune system and hemodynamic properties when compared to humans.

Limitations of this study

This study has several limitations. The used model did not allow for direct control in the development of dilated cardiomyopathy and forced the deductive assessment based on functional and descriptive measurements. However, patho-physiological features have been observed that are characteristic for DCM (ejection fraction, ventricular dilatation). Although it should be noted that there are significant systemic differences in the immune system, the physical parameters (heart rate, generated

force/mm^3) and genetic distance between man and rodents [93].
Due to the spatial limitation of tissue volume that can be imaged in real-time using molecular ultrasound imaging, the analyzed hearts cannot be characterized on a global organ-scale, in contrast to MRI. Additionally, the limited spatial resolution of CEU at 7MHz in the mouse model used precluded a precise regional assessment of the disease activity. Another limitation is the routinely overestimation of LV mass and Ejection fraction with 2D-echocardiography, compared to MRI [94] and is additionally complicated with extensive remodeling and the application in small-animal models that exhibit a high cardiac frequency and small spatial dimensions.
Last, the average collagen content was reported to be less strict and seems to be a less robust predictor on systolic heart-function, because small qualitative differences in cross-linking and collagen-ratios can have a huge impact in the passive mechanical properties [95].

3.5 Summary

Until today, the link between myocardial inflammation in myocarditis and the development of ventricular dilatation is not well understood because of the complexity of the immune response and the lack of available data.
Individuals, who suffer from severe myocardial tissue damage caused by inflammatory processes are at high risk to progress into dilated cardiomyopathy.

To predict the progression to dilated cardiomyopathy and subsequently heart failure, contrast enhanced ultrasound at the acute stage of myocarditis is moderately correlated with the extend of fibrosis as well as a reduction in end-diastolic and end-systolic pressure.
Ejection fraction as an important parameter of systolic function during the chronic phase in myocarditis could not be predicted with any parameters at the acute phase, although heart rate and LV mass were correlated. However, these two parameters are insignificant on their own in the clinical setting.
The progression into dilated cardiomyopathy is with the here applied measurements with structural, functional and ultrasound molecular imaging not predictable in the murine experimental autoimmune myocarditis model by relying on one single parameter. However, the use of ultrasound molecular imaging might help one day in diagnosing myocarditis and the progression by providing additional information about the pathology in multi-parameter diagnostics.

4 Conclusions

Myocarditis is defined as an inflammatory infiltration of the myocardium with myocyte degeneration and necrosis in the absence of ischemia. The inflammation can be caused by various cardiotropic pathogens or drugs. The natural course of the disease usually is clearance of the pathogens and confinement of the inflammation. The symptoms of the disease are often cold- or flue-like, if they are perceptible at all. However, some patients will develop symptoms of heart failure and myocarditis is is the main cause for sudden cardiac death in young adults.

The diagnostic tools are not satisfying, including either invasive biopsies, expensive and availability-limited magnetic resonance imaging or tests lacking either sensitivity or specificity.
Ultrasound molecular imaging, that combines real-time imaging capabilities, a save application and the widespread availability of ultrasound as a diagnostic tool with molecular targeted contrast agents would be of tremendous advantage.

The aim for this study was to use contrast enhanced ultrasound (CEU) molecular imaging to detect the inflammatory process in myocarditis at the acute stage.
In summary, the results of our study indicate that CEU molecular imaging can be used to detect the inflammatory process in myocarditis and discriminate the disease severity independent of cardiac function.
In addition, specific molecular imaging of a leukocyte subset that is driving the autoimmune process in myocarditis is possible.
As a consequence, CEU molecular imaging can potentially be useful in the diagnosis of myocarditis at an early stage of the disease.

Patients, who have suffered severe myocardial tissue damage caused by the inflammatory processes during the acute phase are at risk to progress into dilated

cardiomyopathy (DCM) and subsequently heart failure.
To date, there is no diagnostic tool available that offers robust prognostic information during the inflammatory process that can predict the extent of the cardiac remodeling and development of DCM.
To predict the progression to dilated cardiomyopathy and subsequently heart failure, contrast enhanced ultrasound at the acute stage of myocarditis was performed. The results for molecular imaging during the acute phase is moderately correlated with the extend of fibrosis as well as a reduction in end-diastolic and end-systolic pressure at the chronic phase of myocarditis.
Ejection fraction as an important parameter of systolic function during the chronic phase could not be predicted with any parameters at the acute phase, although heart rate and LV mass were correlated. However, these two parameters are insignificant on their own in the clinical setting.
The progression into dilated cardiomyopathy is with the here applied measurements with structural, functional and ultrasound molecular imaging not predictable in the murine experimental autoimmune myocarditis model by relying on one single parameter.

However, the use of ultrasound molecular imaging might help one day in diagnosing myocarditis and the progression by providing additional information about the pathology in multi-parameter diagnostics.

Bibliography

1. Caforio, A. L. P. *et al.* Current state of knowledge on aetiology, diagnosis, management, and therapy of myocarditis: a position statement of the European Society of Cardiology Working Group on Myocardial and Pericardial Diseases. *European Heart Journal* **34,** 2636–+ (Sept. 2013) (cit. on p. 26).

2. Theleman, K. P., Kuiper, J. J. & Roberts, W. C. Acute myocarditis (predominately lymphocytic) causing sudden death without heart failure. *American Journal of Cardiology* **88,** 1078–+ (Nov. 2001) (cit. on p. 26).

3. Doolan, A., Langlois, N. & Semsarian, C. Causes of sudden cardiac death in young Australians. *Medical Journal of Australia* **180,** 110–112 (Feb. 2004) (cit. on p. 26).

4. Sagar, S., Liu, P. P. & Cooper Leslie T., J. Myocarditis. *Lancet* **379,** 738–747 (Feb. 2012) (cit. on pp. 26 sq.).

5. Al-Amoodi, M. *et al.* Fulminant myocarditis due to H1N1 influenza. *Circulation: Heart Failure* **3,** e7–e9 (2010) (cit. on p. 26).

6. Barbaro, G. HIV-associated myocarditis. *Heart failure clinics* **1,** 439–448 (2005) (cit. on p. 26).

7. Woodruff, J. F. & Woodruff, J. J. Involvement of T Lymphocytes in Pathogenesis of Coxsackie-virus B3 Heart-disease. *Journal of Immunology* **113,** 1726–1734 (1974) (cit. on pp. 26, 32).

8. Klingel, K. *et al.* Visualization of enteroviral replication in myocardial tissue by ultrastructural in situ hybridization: identification of target cells and cytopathic

effects. *Laboratory investigation; a journal of technical methods and pathology* **78,** 1227–1237 (1998) (cit. on p. 26).

9. Chen, X. *et al.* Pertussis toxin as an adjuvant suppresses the number and function of CD4+CD25+ T regulatory cells. *European journal of immunology* **36,** 671–680 (3 Mar. 2006) (cit. on p. 27).

10. Barbaro, G. Cardiovascular manifestations of HIV infection. *Circulation* **106,** 1420–1425 (2002) (cit. on p. 28).

11. Cihakova, D. & Rose, N. R. Pathogenesis of myocarditis and dilated cardiomyopathy. *Advances in immunology* **99,** 95–114 (2008) (cit. on p. 28).

12. Why, H. *et al.* Clinical and prognostic significance of detection of enteroviral RNA in the myocardium of patients with myocarditis or dilated cardiomyopathy. *Circulation* **89,** 2582–2589 (1994) (cit. on p. 28).

13. Huber, S. A., Sartini, D. & Exley, M. V gamma 4(+) T cells promote autoimmune CD8(+) cytolytic T-lymphocyte activation in coxsackievirus B3-induced myocarditis in mice: Role for CD4(+) Th1 cells. *Journal of Virology* **76,** 10785–10790 (Nov. 2002) (cit. on pp. 29, 32).

14. Eriksson, U., Penninger, J. M. & Kopf, M. Mechanisms of autoimmune heart disease. *Drug Discovery Today: Disease Mechanisms* **1,** 283–288 (2004) (cit. on p. 29).

15. Cunningham, M. W. Cardiac myosin and the TH1/TH2 paradigm in autoimmune myocarditis. *The American journal of pathology* **159,** 5–12 (2001) (cit. on p. 29).

16. Afanasyeva, M. *et al.* Experimental autoimmune myocarditis in A/J mice is an interleukin-4-dependent disease with a Th2 phenotype. *The American journal of pathology* **159,** 193–203 (2001) (cit. on p. 29).

17. Okura, Y. *et al.* Recombinant murine interleukin-12 facilitates induction of cardiac myosin-specific type 1 helper T cells in rats. *Circulation research* **82,** 1035–1042 (10 June 1998) (cit. on p. 30).

18. Lefranc, M.-P. IMGT, the international ImMunoGeneTics database. *Nucleic acids research* **29,** 207–209 (2001) (cit. on p. 30).

19. Ben-Sasson, S. Z. *et al.* IL-1 acts directly on CD4 T cells to enhance their antigen-driven expansion and differentiation. *Proceedings of the National Academy of Sciences of the United States of America* **106,** 7119–7124 (17 Apr. 2009) (cit. on p. 30).

20. Shioi, T., Matsumori, A. & Sasayama, S. Persistent expression of cytokine in the chronic stage of viral myocarditis in mice. *Circulation* **94,** 2930–2937 (1996) (cit. on pp. 30, 56).

21. Leuschner, F., Katus, H. A. & Kaya, Z. Autoimmune myocarditis: past, present and future. *Journal of autoimmunity* **33,** 282–289 (2009) (cit. on p. 30).

22. Cruz-Adalia, A. *et al.* CD69 limits the severity of cardiomyopathy after autoimmune myocarditis. *Circulation* **122,** 1396–1404 (14 Oct. 2010) (cit. on p. 30).

23. Valaperti, A. *et al.* CD11b+ monocytes abrogate Th17 CD4+ T cell-mediated experimental autoimmune myocarditis. *Journal of immunology (Baltimore, Md. : 1950)* **180,** 2686–2695 (4 Feb. 2008) (cit. on p. 30).

24. Aretz, H. T. *et al.* Myocarditis. A histopathologic definition and classification. *The American journal of cardiovascular pathology* **1,** 3–14 (Jan. 1987) (cit. on p. 31).

25. Chow, L. H. *et al.* Insensitivity of Right Ventricular Endomyocardial Biopsy in the Diagnosis of Myocarditis. *Journal of the American College of Cardiology* **14,** 915–920 (Oct. 1989) (cit. on p. 31).

26. Pinamonti, B. *et al.* Echocardiographic Findings in Myocarditis. *American Journal of Cardiology* **62,** 285–291 (1988) (cit. on p. 32).

27. Mendes, L. A. *et al.* Ventricular remodeling in active myocarditis. *American Heart Journal* **138,** 303–308 (1999) (cit. on p. 32).

28. Hiramitsu, S. *et al.* Transient ventricular wall thickening in acute myocarditis - A serial echocardiographic and histopathologic study. *Japanese Circulation Journal-english Edition* **65,** 863–866 (Oct. 2001) (cit. on p. 32).

29. Kishimoto, C. *et al.* Natural Evolution of Cardiac-function, Cardiac Pathology and Antimyosin Scan in a Murine Myocarditis Model. *Journal of the American College of Cardiology* **17,** 821–827 (Mar. 1991) (cit. on p. 32).

30. Narula, J. *et al.* Diagnostic accuracy of antimyosin scintigraphy in suspected myocarditis. *Journal of Nuclear Cardiology* **3,** 371–381 (1996) (cit. on p. 32).

31. Thavendiranathan, P. *et al.* Improved Detection of Myocardial Involvement in Acute Inflammatory Cardiomyopathies Using T2 Mapping. *Circulation-cardiovascular Imaging* **5,** 102–110 (Jan. 2012) (cit. on p. 32).

32. Mahrholdt, H. *et al.* Cardiovascular magnetic resonance assessment of human myocarditis - A comparison to histology and molecular pathology. *Circulation* **109,** 1250–1258 (Mar. 2004) (cit. on p. 32).

33. Francone, M. *et al.* CMR Sensitivity Varies With Clinical Presentation and Extent of Cell Necrosis in Biopsy-Proven Acute Myocarditis. *Jacc-cardiovascular Imaging* **7,** 254–263 (Mar. 2014) (cit. on p. 32).

34. Van Heeswijk, R. B. *et al.* Selective In Vivo Visualization of Immune-Cell Infiltration in a Mouse Model of Autoimmune Myocarditis by Fluorine-19 Cardiac Magnetic Resonance. *Circulation-cardiovascular Imaging* **6,** 277–284 (Mar. 2013) (cit. on p. 32).

35. Eriksson, U. *et al.* Dendritic cell-induced autoimmune heart failure requires cooperation between adaptive and innate immunity. *Nature Medicine* **9,** 1484–1490 (Dec. 2003) (cit. on pp. 32, 40, 51).

36. Kaufmann, B. A. *et al.* Detection of recent myocardial ischaemia by molecular imaging of P-selectin with targeted contrast echocardiography. *Eur Heart J* **28,** 2011–7 (2007) (cit. on p. 33).

37. Villanueva, F. S. *et al.* Myocardial ischemic memory imaging with molecular echocardiography. *Circulation* **115,** 345–352 (Jan. 2007) (cit. on p. 33).

38. Lindner, J. R. *et al.* Noninvasive ultrasound imaging of inflammation using microbubbles targeted to activated leukocytes. *Circulation* **102,** 2745–2750 (Nov. 2000) (cit. on pp. 35, 51, 59).

39. Lindner, J. R. *et al.* Ultrasound assessment of inflammation and renal tissue injury with microbubbles targeted to P-selectin. *Circulation* **104,** 2107–2112 (Oct. 2001) (cit. on pp. 35, 59).

40. Gao, S. *et al.* Echocardiography in Mice. *Current protocols in mouse biology* **1,** 71–83 (Mar. 2011) (cit. on pp. 37, 60).

41. Bauer, M. *et al.* Echocardiographic Speckle-Tracking Based Strain Imaging for Rapid Cardiovascular Phenotyping in Mice. *Circulation Research* **108,** 908–U33 (Apr. 2011) (cit. on pp. 38, 45, 60).

42. Raher, M. J. *et al.* In vivo characterization of murine myocardial perfusion with myocardial contrast echocardiography - Validation and application in nitric oxide synthase 3-deficient mice. *Circulation* **116,** 1250–1257 (Sept. 2007) (cit. on p. 40).

43. Felker, G. M. *et al.* Echocardiographic findings in fulminant and acute myocarditis. *Journal of the American College of Cardiology* **36,** 227–232 (July 2000) (cit. on pp. 50, 77).

44. McCarthy, R. E. *et al.* Long-term outcome of fulminant myocarditis as compared with acute (nonfulminant) myocarditis. *New England Journal of Medicine* **342,** 690–695 (2000) (cit. on p. 51).

45. Cai, Y. H. *et al.* Abrogation of functional selectin-ligand expression reduces migration of pathogenic CD8(+) T cells into heart. *Journal of Immunology* **176,** 6568–6575 (June 2006) (cit. on p. 51).

46. Weller, G. E. R. *et al.* Ultrasound Imaging of acute cardiac transplant rejection with microbubbles targeted to intercellular adhesion molecule-1. *Circulation* **108,** 218–224 (July 2003) (cit. on p. 51).

47. Kondo, I. *et al.* Leukocyte-targeted myocardial contrast echocardiography can assess the degree of acute allograft rejection in a rat cardiac transplantation model. *Circulation* **109,** 1056–1061 (Mar. 2004) (cit. on p. 51).

48. Afanasyeva, M., Georgakopoulos, D. & Rose, N. R. Autoimmune myocarditis: cellular mediators of cardiac dysfunction. *Autoimmunity Reviews* **3,** 476–486 (Nov. 2004) (cit. on p. 51).

49. Afanasyeva, M. *et al.* Quantitative analysis of myocardial inflammation by flow cytometry in murine autoimmune myocarditis - Correlation with cardiac function. *American Journal of Pathology* **164,** 807–815 (Mar. 2004) (cit. on p. 52).

50. D'Ambrosio, A. *et al.* The fate of acute myocarditis between spontaneous improvement and evolution to dilated cardiomyopathy: a review. *Heart (British Cardiac Society)* **85,** 499–504 (5 May 2001) (cit. on p. 53).

51. Yilmaz, A. *et al.* Role of cardiovascular magnetic resonance imaging (CMR) in the diagnosis of acute and chronic myocarditis. *Heart failure reviews* **18,** 747–760 (6 Nov. 2013) (cit. on p. 53).

52. Mason, J. W. *et al.* A clinical trial of immunosuppressive therapy for myocarditis. The Myocarditis Treatment Trial Investigators. *The New England journal of medicine* **333,** 269–275 (5 Aug. 1995) (cit. on p. 53).

53. Merlo, M. *et al.* Prevalence and prognostic significance of left ventricular reverse remodeling in dilated cardiomyopathy receiving tailored medical treatment. *Journal of the American College of Cardiology* **57,** 1468–1476 (2011) (cit. on p. 53).

54. Malik, M. Arrhythmic substrate. *Heart (British Cardiac Society)* **94,** 402–403 (4 Apr. 2008) (cit. on p. 53).

55. Moloney, E. D. *et al.* Transplantation for myocarditis: a controversy revisited. *The Journal of heart and lung transplantation : the official publication of the International Society for Heart Transplantation* **24,** 1103–1110 (8 Aug. 2005) (cit. on p. 53).

56. Kwak, H.-B. Aging, exercise, and extracellular matrix in the heart. *Journal of Rehabilitation* **9,** 338–347 (2013) (cit. on p. 53).

57. Senyo, S. E., Lee, R. T. & Kühn, B. Cardiac regeneration based on mechanisms of cardiomyocyte proliferation and differentiation. *Stem cell research* **13,** 532–541 (3 Pt B Nov. 2014) (cit. on p. 54).

58. Marijianowski, M. M. *et al.* Dilated cardiomyopathy is associated with an increase in the type I/type III collagen ratio: a quantitative assessment. *Journal of the American College of Cardiology* **25,** 1263–1272 (1995) (cit. on p. 54).

59. Woodiwiss, A. *et al.* Reduction in myocardial collagen cross-linking parallels left ventricular dilatation in rat models of systolic chamber dysfunction. *Circulation* **103,** 155–160 (2001) (cit. on p. 54).

60. Ono, K. *et al.* Cytokine gene expression after myocardial infarction in rat hearts. *Circulation* **98,** 149–156 (1998) (cit. on p. 54).

61. Westermann, D. *et al.* Immunomodulation and matrix metalloproteinases in viral myocarditis. *Journal of molecular and cellular cardiology* **48,** 468–473 (2010) (cit. on p. 55).

62. Marchant, D. & McManus, B. M. Matrix metalloproteinases in the pathogenesis of viral heart disease. *Trends in cardiovascular medicine* **19,** 21–26 (2009) (cit. on p. 55).

63. Schönbeck, U., Mach, F. & Libby, P. Generation of biologically active IL-1β by matrix metalloproteinases: a novel caspase-1-independent pathway of IL-1β processing. *The Journal of Immunology* **161,** 3340–3346 (1998) (cit. on p. 55).

64. Sambrano, G. R. *et al.* Cathepsin G activates protease-activated receptor-4 in human platelets. *The Journal of biological chemistry* **275,** 6819–6823 (10 Mar. 2000) (cit. on p. 56).

65. Sabri, A. *et al.* Protease-Activated Receptor-1–Mediated DNA Synthesis in Cardiac Fibroblast Is via Epidermal Growth Factor Receptor Transactivation. *Circulation research* **91,** 532–539 (2002) (cit. on p. 56).

66. Antoniak, S. *et al.* PAR-1 contributes to the innate immune response during viral infection. *The Journal of clinical investigation* **123,** 1310–1322 (3 Mar. 2013) (cit. on p. 56).

67. Slofstra, S. H. *et al.* Protease-activated receptor-4 inhibition protects from multiorgan failure in a murine model of systemic inflammation. *Blood* **110,** 3176–3182 (2007) (cit. on p. 56).

68. Rattenholl, A. & Steinhoff, M. Proteinase-activated receptor-2 in the skin: receptor expression, activation and function during health and disease. *Drug News Perspect* **21,** 369–381 (2008) (cit. on p. 56).

69. Diaz, J. A. *et al.* Critical Role for IL-6 in Hypertrophy and Fibrosis in Chronic Cardiac Allograft Rejection. *American Journal of Transplantation* **9,** 1773–1783 (2009) (cit. on p. 56).

70. Baldeviano, G. C. *et al.* Interleukin-17A is dispensable for myocarditis but essential for the progression to dilated cardiomyopathy. *Circulation research* **106,** 1646–1655 (2010) (cit. on p. 56).

71. Cortez, D. M. *et al.* IL-17 stimulates MMP-1 expression in primary human cardiac fibroblasts via p38 MAPK-and ERK1/2-dependent C/EBP-β, NF-κB, and AP-1 activation. *American Journal of Physiology-Heart and Circulatory Physiology* **293,** H3356–H3365 (2007) (cit. on p. 56).

72. Goebel, B. *et al.* Early diastolic strain rate predicts response to heart failure therapy in patients with dilated cardiomyopathy. *The international journal of cardiovascular imaging* **30,** 505–513 (2014) (cit. on p. 56).

73. Rademakers, F. E. *et al.* Relation of regional cross-fiber shortening to wall thickening in the intact heart. Three-dimensional strain analysis by NMR tagging. *Circulation* **89,** 1174–1182 (1994) (cit. on p. 57).

74. Fry, D. I., Griggs, D. M. & Greenfield, J. C. Myocardial Mechanics: Tension-Velocity-Length Relationships of Heart Muscle. *Circulation research* **14,** 73–85 (Jan. 1964) (cit. on p. 57).

75. *The Dynamic Heart and Circulation* (ed Holdrege, C.) (AWSNA, 2002) (cit. on p. 57).

76. Pacher, P. *et al.* Measurement of cardiac function using pressure–volume conductance catheter technique in mice and rats. *Nature protocols* **3,** 1422–1434 (2008) (cit. on p. 70).

77. Aasum, E. *et al.* Age-dependent changes in metabolism, contractile function, and ischemic sensitivity in hearts from db/db mice. *Diabetes* **52,** 434–441 (2003) (cit. on p. 77).

78. Barry, J., Maron, J. A., *et al.* Contemporary definitions and classification of the cardiomyopathies. *Circulation* **113,** 1807–1816 (2006) (cit. on p. 78).

79. Iwanaga, Y. *et al.* Excessive activation of matrix metalloproteinases coincides with left ventricular remodeling during transition from hypertrophy to heart failure in hypertensive rats. *Journal of the American College of Cardiology* **39,** 1384–1391 (2002) (cit. on p. 79).

80. Müller-Brunotte, R. *et al.* Myocardial fibrosis and diastolic dysfunction in patients with hypertension: results from the Swedish Irbesartan Left Ventricular Hypertrophy Investigation versus Atenolol (SILVHIA). *Journal of hypertension* **25,** 1958–1966 (2007) (cit. on p. 79).

81. Soufen, H. *et al.* Collagen content, but not the ratios of collagen type III/I mRNAs, differs among hypertensive, alcoholic, and idiopathic dilated cardiomyopathy. *Brazilian Journal of Medical and Biological Research* **41,** 1098–1104 (2008) (cit. on p. 79).

82. Hadi, A. M. *et al.* Rapid quantification of myocardial fibrosis: a new macro-based automated analysis. *Cellular oncology* **34,** 343–354 (2011) (cit. on p. 79).

83. Rich, L. & Whittaker, P. Collagen and picrosirius red staining: a polarized light assessment of fibrillar hue and spatial distribution. *Braz J Morphol Sci* **22,** 97–104 (2005) (cit. on p. 79).

84. Clements, I. P., Miller, W. L. & Olson, L. J. Resting heart rate and cardiac function in dilated cardiomyopathy. *International journal of cardiology* **72,** 27–37 (1999) (cit. on p. 79).

85. Sajadieh, A. *et al.* Increased heart rate and reduced heart-rate variability are associated with subclinical inflammation in middle-aged and elderly subjects with no apparent heart disease. *European heart journal* **25,** 363–370 (2004) (cit. on p. 79).

86. Juilliere, Y. *et al.* Radionuclide assessment of regional differences in left ventricular wall motion and myocardial perfusion in idiopathic dilated cardiomyopathy. *European heart journal* **14,** 1163–1169 (1993) (cit. on p. 80).

87. Yanagisawa, K. *et al.* Phagocytosis of ultrasound contrast agent microbubbles by Kupffer cells. *Ultrasound in medicine & biology* **33,** 318–325 (2007) (cit. on p. 80).

88. Little, W. C. *Diastolic Dysfunction Beyond Distensibility* 2005 (cit. on p. 82).

89. Fukuta, H. & Little, W. C. The cardiac cycle and the physiologic basis of left ventricular contraction, ejection, relaxation, and filling. *Heart failure clinics* **4,** 1–11 (2008) (cit. on p. 82).

90. Beltrami, C. A. *et al.* Structural basis of end-stage failure in ischemic cardiomyopathy in humans. *Circulation* **89,** 151–163 (1994) (cit. on p. 82).

91. Baicu, C. F. *et al.* Changes in extracellular collagen matrix alter myocardial systolic performance. *American Journal of Physiology-Heart and Circulatory Physiology* **284,** H122–H132 (2003) (cit. on p. 82).

92. Yotti, R. *et al.* A noninvasive method for assessing impaired diastolic suction in patients with dilated cardiomyopathy. *Circulation* **112,** 2921–2929 (2005) (cit. on p. 82).

93. Recchia, F. & Lionetti, V. Animal models of dilated cardiomyopathy for translational research. *Veterinary research communications* **31** (2007) (cit. on p. 84).

94. Strohm, O. *et al.* Measurement of left ventricular dimensions and function in patients with dilated cardiomyopathy. *Journal of Magnetic Resonance Imaging* **13,** 367–371 (2001) (cit. on p. 84).

95. Brower, G. L. *et al.* The relationship between myocardial extracellular matrix remodeling and ventricular function. *European journal of cardio-thoracic surgery : official journal of the European Association for Cardio-thoracic Surgery* **30,** 604–610 (4 Oct. 2006) (cit. on p. 84).

96. McCrohon, J. A. *et al.* Differentiation of heart failure related to dilated cardiomyopathy and coronary artery disease using gadolinium-enhanced cardiovascular magnetic resonance. *Circulation* **108,** 54–59 (1 July 2003).